

DOCTOR OF PHILOSOPHY

Learning Uncertainties in Ego-Motion Sensors for the Localisation of Autonomous Vehicles in GNSS-Deprived Environments

Onyekpe, Uche

Award date:
2021

Awarding institution:
Coventry University

[Link to publication](#)

General rights

Copyright and moral rights for the publications made accessible in the public portal are retained by the authors and/or other copyright owners and it is a condition of accessing publications that users recognise and abide by the legal requirements associated with these rights.

- Users may download and print one copy of this thesis for personal non-commercial research or study
- This thesis cannot be reproduced or quoted extensively from without first obtaining permission from the copyright holder(s)
- You may not further distribute the material or use it for any profit-making activity or commercial gain
- You may freely distribute the URL identifying the publication in the public portal

Take down policy

If you believe that this document breaches copyright please contact us providing details, and we will remove access to the work immediately and investigate your claim.

Learning Uncertainties in Ego-Motion Sensors for the Localisation of Autonomous Vehicles in GNSS-Deprived Environments



Uche Onyekpe

Centre of Computational Science and Mathematical Modelling

Institute for Mathematical, Physical and Computational Science

Coventry University

A thesis submitted in partial fulfillment of the University's requirement for
the degree of *Doctor of Philosophy*

June 2021



Certificate of Ethical Approval

Applicant:

Uche Onyekpe

Project Title:

Efficient Machine learning for autonomous vehicle embedded systems

This is to certify that the above named applicant has completed the Coventry University Ethical Approval process and their project has been confirmed and approved as Low Risk

Date of approval:

10 October 2019

Project Reference Number:

P95615

Acknowledgement

I would like to thank my supervisors; Prof. Vasile Palade, Prof. Stratis Kanarachos, and Dr. Stravros Richard G Christopoulos for their support, guardianship, and patience during my Ph.D. journey. I feel thankful to the people I met at different stages of my Ph.D. program, particularly for their massive support and motivation to keep me moving forward. They made my research journey a wonderful experience.

I am also thankful to a great number of colleagues, whom I feel chanced and elated to receive technical support from. They are in (no particular order); Alicja Szkolnik, Anuradha Herath, Thierry Touzet, Ninan Touzet, Sarah Tompkins, and Andy Thompson. I remain grateful for their interesting and wonderful opinions, contributions, and technical support which went a long way in enabling the completion of my Ph.D.

And my biggest thanks goes to my family and friends for their support and encouragement, Pallavi Joshi, thanks for the interesting conversations and help with proof reading; Alicja Szkolnik, James Spooner, Benin Wahab, Mark Bevan, Kevon Kelly of Kitau Robotics and Abdulrahman Mahmoud thanks for the useful conversations! To my parents, thank you, I would not be there if it had not been for your faith in me and your devotion to my education, I am forever grateful. A special thanks goes to my uncle Dele who enabled my studies in the UK. Finally, to my wife; Orane Onyekpe-Touzet who has been by my side during this whole journey, thank you for your patience and support, conversations and for your help proof-reading chapters.

Abstract

In the absence of signals from Global Navigation Satellite Systems (GNSS), Inertial Navigation Systems (INS) are usually used to position vehicles. However, INS sensors are commonly plagued by noises, which grow exponentially over time during the multiple integration computation, leading to a poor navigation result. More so, the error drift is characterised by a time dependent pattern. This thesis proposes several efficient deep learning - based solutions to learn the position and orientation error drifts of the vehicle using Recurrent Neural Networks, such as the simple Recurrent Neural Network (sRNN), Long Short-Term Memory (LSTM), Gated Recurrent Unit (GRU) and the Input Delay Neural Network (IDNN).

The thesis also investigates the use of the wheel encoder as an alternative to the accelerometer of the INS for vehicular positioning, and for the first time explores the potential of deep learning using the simple recurrent neural network to learn the uncertainty present in the wheel encoder's output. These uncertainties could be manifested as wheel slips because of wet/muddy road drive or worn out tyres; or changes in the tyre size or pressure. The proposed solution has less integration steps in its computation, and as such, has the potential to provide a more accurate estimation of the vehicles position.

In contrast to previous papers published in literature, which focused on travel routes that do not consider complex driving scenarios, this thesis investigates the performance of the proposed deep learning-based models to accurately estimate the position of the vehicle in challenging scenarios. These scenarios include, roundabouts, hard brake, sharp cornering, quick changes in vehicular acceleration, successive left and right turns.

The performance of the deep learning models are then further evaluated extensively on longer-term GNSS outages of 30s, 60s, 120s and 180s duration respectively, over a total distance of 493 km. The experimental results obtained show that the proposed deep learning model using wheel odometry data is able to accurately position the vehicle with up to 93% reduction in the positioning error of its original (physics model) counterpart after any 180s of travel.

Contents

Chapter 1	Introduction.....	1
	1.1 Importance of Autonomous Vehicles.....	1
	1.2 GNSS (Global Navigation Satellite System) Issues.....	2
	1.3 Navigation using Inertial Measurement Sensors.....	3
	1.4 Inertial Positioning using Wheel Encoder Sensor.....	5
	1.5 Research challenges.....	5
	1.51 Lack of a Publicly Available Dataset for Ego-motion Odometry.....	6
	1.52 Accuracy and Robustness.....	6
	1.53 Adaptation to Vehicles with Different Domain Characteristics.....	6
	1.6 Research Questions.....	7
	1.7 Contributions.....	8
	1.8 Thesis Outline.....	11
Chapter 2	Background and Literature Review on Positioning Techniques.....	13
	2.1 Land Vehicular Positioning techniques.....	13
	2.1.1 Global Navigation Satellite Systems (GNSS).....	13
	2.1.2 Dead Reckoning (DR) Systems.....	14
	2.1.3 Multi-sensor Augmented Positioning Systems....	17
	2.2 Coordinate Systems.....	20
	2.2.1 Inertial Frame.....	20
	2.2.2 Earth Fixed Frame.....	21
	2.2.3 Body (Sensor) Frame.....	21
	2.3 Machine Learning-based Localisation Models. Review, Limitations and Challenges.....	22
	2.3.1 Kalman Filters.....	22
	2.3.2 Other Machine Learning Techniques.....	24
	2.3.3 Machine Learning Techniques used in this Thesis	25
	2.4 Summary.....	30
Chapter 3	Dataset and Methodology for Inertial and Odometry Vehicular Localisation.....	31
	3.1 Datasets.....	31
	3.1.1 Inertial and Odometry Vehicle Navigation Benchmark Dataset (IO-VNBD).....	33
	3.1.2 Coventry University Public road dataset for Automated Cars (CUPAC) Dataset.....	39
	3.2 Methodology.....	39
	3.2.1 Ground Truth Formulation – Positioning and Orientation Rate Formulation Using GNSS.....	39

	3.2.2	Physics Model and Machine Learning Schemes for Vehicular Position and Orientation Estimation	42
	3.2.3	Model Selection, Training and Evaluation.....	49
	3.3	Summary.....	61
Chapter 4		Results and Analysis on Position and Orientation Estimation in Challenging (Complex) GNSS Environments.....	63
	4.1	Challenging Localisation Environments.....	63
	4.1.1	Roundabout.....	64
	4.1.2	Quick Changes in Acceleration.....	64
	4.1.3	Hard Brake.....	64
	4.1.4	Successive Left and Right Turns and Sharp Cornering.....	64
	4.1.5	Wet Road.....	64
	4.2	Results and Discussion.....	65
	4.2.1	Motorway Scenario.....	65
	4.2.2	Roundabout Scenario.....	69
	4.2.3	Quick Changes in Vehicle Acceleration Scenario	73
	4.2.4	Hard Brake Scenario.....	77
	4.2.5	Sharp Cornering and Successive Left-Right Turns Scenario.....	80
	4.2.6	Wet Road.....	84
	4.3	Summary.....	88
Chapter 5		Result and Analysis on Position Estimation in Longer Term GNSS Outages.....	89
	5.1	Performance Evaluation on the Longer term GNSS outages.....	90
	5.1.1	30s GNSS Outage Scenario.....	90
	5.1.2	60s GNSS Outage Scenario.....	93
	5.1.3	120s GNSS Outage Scenario.....	97
	5.1.4	180s GNSS Outage Scenario.....	101
	5.2	Summary.....	105
Chapter 6		New Vehicle Domain Adaptation of Vehicular Position Model using Transfer Learning.....	106
	6.1	Motivation.....	106
	6.2	Transfer Learning.....	107
	6.2.1	Definition of representations.....	107
	6.2.2	Definition of Transfer Learning.....	108
	6.2.3	Model Definitions.....	109
	6.3	Model Training and Evaluation.....	110
	6.3.1	G-WhONet's Training.....	110
	6.3.2	S-WhONet's Training.....	111
	6.3.3	R-WhONet's Training.....	111
	6.3.4	R-WhONet Training Time Selection Experiment	112
	6.3.5	Model Evaluation.....	113
	6.4	Result and Discussion.....	113
	6.4.1	30 s GNSS Outage.....	113

	6.4.2	60 s GNSS Outage.....	116
	6.4.3	120 s GNSS Outage.....	119
	6.4.4	180 s GNSS Outage.....	121
	6.5	Summary	124
Chapter 7		Conclusions and Future Work.....	126
	7.1	Conclusions.....	126
	7.2	Limitations.....	129
	7.3	Future Work.....	130
	7.3.1	Map Matching.....	130
	7.3.2	Explainable, Reliable and Accurate Localisation	130
	7.3.3	Sensor Fusion.....	131
Appendix A		132
References		144

List of Figures

2.1	Dead-reckoning; showing the integration of the INS's measurement to position.....	15
2.2	Dead reckoning; showing the integration of the WO/INS's measurement to position.....	17
2.3	Inertial frame.....	20
2.4	Earth fixed frame.....	21
2.5	Body frame axis.....	22
2.6	Unrolled RNN architecture.....	26
2.7	LSTM cell structure.....	27
2.8	Cell Structure of the GRU.....	28
2.9	Illustration of an IDNN's general architecture.....	29
3.1	Sensor locations and dimension of vehicle.....	34
3.2	Smartphone and GPS antennae setup.....	35
3.3	Prediction setup of the proposed AccNet displacement estimation model.....	47
3.4	Training setup of the AccNet displacement estimation model.....	47
3.5	AccNet's learning scheme.....	48
3.6	GyroNet's learning scheme.....	48
3.7	GyroNet's orientation rate prediction block during GNSS outages.....	48
3.8	WhONet's learning scheme.....	49
3.9	WhONet's position prediction block during GNSS outages.....	49
4.1	Sample evolution of the estimation error over time in the motorway scenario based on the position CRSE.....	67
4.2	Sample evolution of the estimation error over time in the motorway scenario based on the position CTE.....	67
4.3	Sample evolution of the estimation error over time in the motorway scenario based on the orientation rate CRSE.....	68
4.4	Sample evolution of the estimation error over time in the motorway scenario based on the orientation rate CTE.....	68
4.5	The comparison of the CRSE and CTE performance of the WhONet, WPM, AccNet and APM across all investigated challenging scenarios on the displacement estimation.....	68
4.6	The comparison of the CRSE and CTE performance of the GyroNet and GPM across all investigated challenging scenarios on the orientation rate estimation.....	69
4.7	Sample evolution of the estimation error over time in the roundabout scenario based on the position CRSE.....	71
4.8	Sample evolution of the estimation error over time in the roundabout scenario based on the position CTE.....	72

4.9	Sample evolution of the estimation error over time in the roundabout scenario based on the position CRSE.....	72
4.10	Sample evolution of the estimation error over time in the roundabout scenario based on the Orientation rate CTE.....	72
4.11	Sample trajectory of the (a) V-Vta11 roundabout data subset of the Inertia and Odometry Vehicle Navigation Dataset (IO-VNBD) and (b) V-Vw12 motorway data subset of the IOVNBD.....	73
4.12	Sample evolution of the estimation error over time in the quick changes in acceleration scenario based on the position CRSE....	75
4.13	Sample evolution of the estimation error over time in the quick changes in acceleration scenario based on the position CTE.....	75
4.14	Sample evolution of the estimation error over time in the quick changes in acceleration scenario based on the Orientation rate CRSE.....	75
4.15	Sample evolution of the estimation error over time in the quick changes in acceleration scenario based on the Orientation rate CTE.	75
4.16	Sample evolution of the estimation error over time in the hard brake scenario based on the position CRSE.....	79
4.17	Sample evolution of the estimation error over time in the hard brake scenario based on the position CTE.....	79
4.18	Sample evolution of the estimation error over time in the hard brake scenario based on the Orientation rate CRSE.....	79
4.19	Sample evolution of the estimation error over time in the hard brake scenario based on the Orientation rate CTE.....	80
4.20	Sample evolution of the estimation error over time in the sharp cornering and successive left and right turns scenario based on the position CRSE.....	83
4.21	Sample evolution of the estimation error over time in the sharp cornering and successive left and right turns scenario based on the position CTE.....	83
4.22	Sample evolution of the estimation error over time in the sharp cornering and successive left and right turns scenario based on the Orientation rate CRSE.....	83
4.23	Sample evolution of the estimation error over time in the sharp cornering and successive left and right turns scenario based on the Orientation rate CTE.....	84
4.24	Trajectory of V-Vw8 sharp cornering and successive left and right turns data subset of the IO-VNBD.....	87
4.25	Sample evolution of the estimation error over time in the wet road scenario based on the position CRSE.....	87
4.26	Sample evolution of the estimation error over time in the wet road scenario based on the position CTE.....	87
4.27	Sample evolution of the estimation error over time in the wet road scenario based on the Orientation rate CRSE.....	88
4.28	Sample evolution of the estimation error over time in the wet road scenario based on the Orientation rate CTE.....	88

5.1	Comparison of the average positional CRSE on the IO-VNB and CUPAC dataset during the 30s GNSS signal outage experiment	91
5.2	Comparison of the average positional CTE on the IO-VNB and CUPAC dataset during the 30s GNSS signal outage experiment	91
5.3	Showing a sample evolution of the estimation error over time in the 30 s GNSS outage scenario based on the position CRSE and CTE	91
5.4	Comparison of the average positional CRSE on the IO-VNB and CUPAC dataset during the 60s GNSS signal outage experiment	94
5.5	Comparison of the average positional CTE on the IO-VNB and CUPAC dataset during the 60s GNSS signal outage experiment	95
5.6	Showing a sample evolution of the estimation error over time in the 60s GNSS outage scenario based on the position CRSE and CTE	95
5.7	Comparison of the average positional CRSE on the IO-VNB and CUPAC dataset during the 120s GNSS signal outage experiment	98
5.8	Comparison of the average positional CTE on the IO-VNB and CUPAC dataset during the 120s GNSS signal outage experiment	98
5.9	Sample evolution of the estimation error over time in the 120s GNSS outage scenario based on the position CRSE and CTE	99
5.1	Comparison of the average positional CRSE on the IO-VNB and CUPAC dataset during the 180s GNSS signal outage experiment	102
5.11	Comparison of the average positional CTE on the IO-VNB and CUPAC dataset during the 180s GNSS signal outage experiment	102
5.12	Sample evolution of the estimation error over time in the 180 s GNSS outage scenario based on the position CRSE and CTE	102
5.13	The vehicle trajectory on the V-Vfb02g dataset (left) and V-Vfbo2b dataset (right) used in evaluating WhONet's performance during the 30s, 60s, 120s and 180s GNSS outage experiment.....	103
6.1	Sample CRSE evolution of the models on the Delta 2 CUPAC dataset during the 30 s GNSS outage scenario after recalibration.....	115
6.2	Sample CTE evolution of the models on the Delta 2 CUPAC dataset during the 30 s GNSS outage scenario after recalibration.....	116
6.3	CRSE and CTE comparison of the models on the Charlie 4 CUPAC dataset during the 30 s GNSS outage scenario after recalibration.....	116
6.4	CRSE evolution of the models on the Delta 2 CUPAC dataset during the 60 s GNSS outage scenario after recalibration.....	118
6.5	Sample CTE evolution of the models on the Delta 2 CUPAC dataset during the 60 s GNSS outage scenario after recalibration.....	118
6.6	CRSE and CTE comparison of the models on the Charlie 4 CUPAC dataset during the 60 s GNSS outage scenario after recalibration.....	118

6.7	Sample CRSE evolution of the models on the Delta 2 CUPAC dataset during the 120 s GNSS outage scenario after recalibration.....	120
6.8	Sample CTE evolution of the models on the Delta 2 CUPAC dataset during the 120 s GNSS outage scenario after recalibration.....	121
6.9	CRSE and CTE comparison of the models on the Char-lie 4 CUPAC dataset during the 120 s GNSS outage scenario after recalibration.....	121
6.1	Sample CRSE evolution of the models on the Delta 2 CUPAC dataset during the 180 s GNSS outage scenario after recalibration.....	123
6.11	Showing a sample CTE evolution of the models on the Delta 2 CUPAC dataset during the 180 s GNSS outage scenario after recalibration.....	123
6.12	CRSE and CTE comparison of the models on the Char-lie 4 CUPAC dataset during the 180 s GNSS outage scenario after recalibration.....	124

List of Tables

1	Publications from this thesis.....	12
2.1	The requirements of a positioning system.....	18
2.2	Comparison of the WO/ INS, GPS and the integrated WO/INS/GPS system.....	19
2.3	Requirement for land positioning systems in urban areas.....	20
3.1	Dataset collection platforms.....	32
3.2	Several datasets for vehicular localisation.....	32
3.3	Driving pattern of each driver.....	36
3.4	Various tyre pressures experimented on.....	37
3.5	Information recorded from the Ford Fiesta's ECU.....	37
3.6	Environmental and driving scenarios investigated.....	38
3.7	Information recorded from the smartphone sensors.....	38
3.8	Number of trainable parameters in each Neural Network (NN) across various weighted connections.....	52
3.9	The performance evaluation based on the Cumulative Root Squared Error (CRSE) metric of the Input Delay Neural Network (IDNN) in each investigated scenario across several time steps on the orientation rate estimation (GyroNet model).....	52
3.10	Performance evaluation based on the CRSE metric of the IDNN in each investigated scenario across several time steps on the AccNet model.....	53
3.11	Performance comparison of the IDNN, LSTM, GRU and sRNN using the CTE and CRSE metric on the WhONet model.....	54
3.12	Training parameters of models used in this thesis.....	56
3.13	IO-VNB data subsets used in training the models.....	56
3.14	CUPAC data subsets used in training the models.....	58
3.15	IO-VNB data test subset used in the motorway scenario.....	59
3.16	IO-VNB data test subset used in the challenging scenarios.....	59
3.17	IO-VNB data subsets used for the longer GNSS outage scenario performance evaluation.....	60
3.18	CUPAC data subsets used for the longer GNSS outage scenario performance evaluation.....	61
4.1	The experimental results of AccNet and APM on the motorway scenario.....	66
4.2	The experimental results of WhONet and WPM on the motorway scenario.....	66
4.3	The experimental results of GyroNet and GPM on the motorway scenario.....	66
4.4	The experimental results of AccNet and APM on the roundabout scenario.....	70
4.5	The experimental results of WhONet and WPM on the roundabout scenario.....	70
4.6	The experimental results of GyroNet and GPM on the roundabout scenario.....	71
4.7	The performance of AccNet and APM on the quick changes in acceleration scenario.....	74

4.8	The performance of WhONet and WPM on the quick changes in acceleration scenario.....	74
4.9	The performance of GyroNet and GPM on the quick changes in acceleration scenario.....	75
4.10	The performance of AccNet and APM on the hard brake scenario.....	77
4.11	The performance of WhONet and WPM on the hard brake scenario.....	78
4.12	The performance of GyroNet and GPM on the hard brake scenario.....	78
4.13	The performance of AccNet and APM on the sharp cornering and successive left and right turns scenario.....	81
4.14	The performance of WhONet and WPM on the sharp cornering and successive left and right turns scenario.....	81
4.15	The performance of GyroNet and GPM on the sharp cornering and successive left and right turns scenario.....	82
4.16	The performance of AccNet and APM on the wet road scenario.....	85
4.17	The performance of WhONet and WPM on the wet road scenario.....	85
4.18	The performance of GyroNet and GPM on the wet road scenario.....	86
5.1	The 30 seconds GNSS outage experiment results on the IO-VNB dataset	92
5.2	The 30 seconds GNSS outage experiment results on the CUPAC dataset	93
5.3	The 60 seconds GNSS outage experiment results on the IO-VNB dataset	95
5.4	The 60 seconds GNSS outage experiment results on the CUPAC dataset	96
5.5	The 120 seconds GNSS outage experiment results on the IO-VNB dataset	99
5.6	The 120 seconds GNSS outage experiment results on the CUPAC dataset	100
5.7	The results from the 180 seconds GNSS outage experiment results on the IO-VNB dataset.....	103
5.8	The 180 seconds GNSS outage experiment results on the CUPAC dataset	104
6.1	Training parameters of the G-WhONet, S-WhONet and R-WhONet models.....	111
6.2	Results from the experimentation of various values of m to determine the adaptation time for the R-WhONet model.....	112
6.3	CRSE performance comparison of the R-WhONet, G-WhONet, S-WhONet and WPM on the 30 seconds GNSS outage scenario.....	114
6.4	CTE performance comparison of the R-WhONet, G-WhONet, S-WhONet and WPM on the 30 seconds GNSS outage scenario.....	114
6.5	CRSE performance comparison of the R-WhONet, G-WhONet, S-WhONet and WPM on the 60 seconds GNSS outage scenario.....	116
6.6	CTE performance comparison of the R-WhONet, G-WhONet, S-WhONet and WPM on the 60 seconds GNSS outage scenario.....	117
6.7	CRSE performance comparison of the R-WhONet, G-WhONet, S-WhONet and WPM on the 120 seconds GNSS outage scenario.....	119
6.8	performance comparison of the R-WhONet, G-WhONet, S-WhONet and WPM on the 30 seconds GNSS outage scenario.....	120
6.9	CRSE performance comparison of the R-WhONet, G-WhONet, S-WhONet and WPM on the 180 seconds GNSS outage scenario.....	122
6.10	CTE performance comparison of the R-WhONet, G-WhONet, S-WhONet and WPM on the 180 seconds GNSS outage scenario.....	122
A1	Existing odometry datasets.....	132
A2-1	Dataset description from Driver A, B and C.....	135
A2-2	Dataset description from Driver C and D.....	136
A3-1	Description of datasets V-Vta1a to V-Vta17 from Driver E.....	137
A3-2	Description of datasets V-Vta19 to V-Vta30 from Driver E.....	138
A4	Description of datasets V-Vtb1 to V-Vtb13 from Driver E.....	139

A5	Description of datasets V-Vw1 to V-Vw12 from Driver E.....	140
A6	Description of datasets V-Vw13 to V -Vw17 from Driver E.....	141
A7-1	Description of datasets V-Vfa01to V-Vfb02c from Driver E.....	142
A7-2	Description of datasets V-Vfb02d to V-Vfb02g from Driver E.....	143
A8	Information on other Smartphone Dataset captured independently from drivers F, G and H.....	143

List of Abbreviations

GNSS	Global Navigation Satellite Systems
AV	Autonomous Vehicle
INS	Inertial Navigation Systems
sRNN	simple Recurrent Neural Network
LSTM	Long Short-Term Memory
IDNN	Input Delay Neural Network
GRU	Gated Recurrent Unit
GPS	Global Positioning System
GLONASS	Global Navigation Satellite System
FMEA	Failure Mode and Effect Analysis
DR	Dead Reckoning
IMU	Inertial Measuring Unit
WO	Wheel Odometer
NN	Neural Network
MFNN	Multi-layer Feed-Forward Neural Network
MLNN	Multi-Layer Neural Network
RNN	Recurrent Neural Network
GRU	Gated Recurrent Unit
MLP	Multi-Layer Perceptron
LSTM	Long Short-Term Memory
HD	High Definition
UAV	Unmanned Ariel Vehicles
AUV	Autonomous Underwater Vehicles
USV	Unmanned Surface Vehicles
IO-VNBD	Inertial and Odometry Vehicle Navigation Benchmark Dataset
CUPAC	Coventry University Public road dataset for Automated Cars
CAN	Controlled Area Network
ECU	Electronic Control Unit
NED	North East Down
APM	Accelerometer-based position estimation Physics Model
GPM	Gyroscope-based orientation rate estimation Physics Model
WPM	Wheel encoder based position estimation Physics Model
AccNet	Accelerometer based position estimation neural Network
GyroNet	Gyroscope based orientation rate estimation neural Network
WhONet	Wheel Odometry position estimation neural Network
R-WhONet	Recalibrated Wheel Odometry position estimation neural Network
G-WhONet	Generic pre-trained Wheel odometry position estimation neural Network
S-WhONet	Specific Wheel odometry position estimation neural Network

CRSE	Cumulative Root Square Error
CTE	Cumulative True Error
max	maximum
min	minimum
XAI	Explainable Artificial Intelligence
AI	Artificial Intelligence

List of Symbols

f^b	specific force in the body frame
g^n	acceleration due to gravity in the navigation frame
a^n	the linear acceleration of the sensor expressed in the navigation frame
a_n^b	acceleration of the sensor as expressed in the navigation frame
R^{nb}	transformational (rotational) matrix from the body frame to the navigation frame
$2\omega_{ie}^n + V_n^n$	coriolis acceleration
$\omega_{ie}^n + \omega_{ie}^n + p^n$	centrifugal acceleration.
ω_{ib}^b	attitude rate of the body frame with respect to the navigation frame as expressed in the body frame
ω_{ie}^n	angular velocity of the earth's frame with respect to the inertial frame as expressed in the navigation frame
ω_{nb}^b	orientation of the vehicle in the body frame with respect to the navigation frame as expressed in the body frame
\hat{w}_{wh}^b	angular speed of the wheel in the body frame
w_{wh}^b	noise free wheel speed measurement as expressed in the body frame
ε_{wh}^b	uncertainty in the wheel encoder's measurement as expressed in the body frame.
g^b	acceleration due to gravity in the body frame
ε_x^b	the noise characterising the INS's displacement derived from ε_a^b
ε_v^b	the noise characterising the INS's velocity from ε_a^b
v_{INS}^b	vehicles velocity in the body frame derived from the INS measurements
x_{INS}^b	vehicles displacement in the body frame derived from the INS measurements
ω_{INS}^b	attitude rate from the gyroscope
Ψ_{INS}	orientation information from the INS
Ψ_0	initial orientation information
r	mapping constant from the wheel speed of the rear axle to the linear velocity of the vehicle.

x_{whr}^b	vehicle's displacement estimation from the wheel encoder
$\varepsilon_{whr,x}^b$	vehicle's positional error
$\varepsilon_{whr,v}^b$	vehicle's velocity error
ω_{INS}^b	yaw rate from the gyroscope in the body frame
ω_{GNSS}^b	yaw rate from the GNSS in the body frame (ground truth for the GyroNet)
R^{ie}	direction cosine matrix or rotation matrix from the earth frame to the inertial frame
w_e	constant angular velocity of the earth about the z-axis of the greenwich mean meridian.
\mathcal{Y}	output vector
\mathcal{X}	input vector
W	weight matrix
b	bias vector
σ_f	sigmoid activation (non-linearity) function
h_{t-1}	previous state
U_h	hidden weight matrix
W_x	input weight matrix
W_o	output weight matrix
b_h	bias vector of the hidden layer
b_o	bias vector of the output layer
\mathcal{Y}_t	output of the network
i_t	input gate
$*$	hadamard product
f_t	forget gate
o_t	output gate
c_t	cell state
h_{t-1}	previous state
W_f	weight matrix of the forget gate
W_i	weight matrix of the input gate
W_c	weight matrix of the current memory state
W_o	weight matrix of the output gate
U_f	hidden weight matrix of the forget gate
U_i	hidden weight matrix of the input gate
U_c	current memory state
U_o	hidden weight matrix of the output gate
b_f	bias vector of the forget gate
b_i	bias vector of the input gate
b_c	bias vector of the current memory state
b_o	bias vector of the output gate
\mathcal{X}_t	input features vector
W_z	weight matrix of the update gate
W_r	weight matrix of the reset gate
W_h	weight matrix of the current memory state
U_z	hidden weight matrix of the update gate

U_r	hidden weight matrix of the reset gate
U_h	hidden weight matrix of the current memory state
b_z	bias vector of the update gate
b_r	bias vector of the reset gate
b_h	bias vector of the current memory state
ϕ	roll
θ	pitch
ψ	yaw
R	measurement noise covariant matrix
Q	system noise covariance matrix
D	delay operator of the IDNN
G	activation function of the IDNN
U_i	the neurons
t	time
\hat{x}_{GPS}^b	vehicle's true displacement in the body frame from the GPS
\emptyset	GPS obtained latitude
φ	GPS obtained longitude
σ'	angle between the position at $t - 1$ and t
\hat{x}_t^b	distance travelled at time t in the body frame
U_1	reduced latitude at t
U_2	reduced latitude at $t - 1$
a	radius of the earth at the equator
f	flattening at the ellipsoid
b	length of the ellipsoid semi-minor axis
λ	change in longitude along the auxiliary spheres
σ'_1	angle between the position at $t - 1$ and t
σ'_m	angle between the equator and midpoint of the line
δ_{INS}^b	sensor bias
ε_a^b	sensor noise from the accelerometer
F_{INS}^b	corrupted measurement of the accelerometer sensor in the body frame
$\hat{\omega}_{whrl}^b, \hat{\omega}_{whrr}^b, \hat{\omega}_{whfl}^b$ and $\hat{\omega}_{whfr}^b$	noisy wheel speed measurements of the rear left, rear right, front left and front right wheels
$\varepsilon_{whrl}^b, \varepsilon_{whrr}^b, \varepsilon_{whfl}^b$ and ε_{whfr}^b	positional errors (uncertainties) of the rear left, rear right, front left and front right wheels
$\omega_{whrl}^b, \omega_{whrr}^b, \omega_{whfl}^b$ and ω_{whfr}^b	respective error-free wheel speed measurements
x_{GNSS}^b	vehicle's true displacement in the body frame from the GNSS
e_{pred}	prediction error
Y_t	error free yaw rate information of the vehicle at time t .

N_t	GNSS outage length of 10s in the challenging scenarios and 30s, 60s, 120s and 180s in the longer-term GNSS outage scenario
t	sampling period
e_{pred}	the position prediction error
μ	statistical mean of the CRSE or CTE across all test sequences in each complex scenario
μ_{CTE}	statistical mean of the CTE across all test sequences in each complex scenario
μ_{CRSE}	statistical mean of the CRSE across all test sequences in each complex scenario
σ_{CTE}	Standard deviation of the CTE across all test sequences in each complex scenario (robustness measure)
σ_{CRSE}	Standard deviation of the CRSE across all test sequences in each complex scenario (robustness measure)
N_s	total number of test sequences in each complex scenario
σ	standard deviation
\mathbf{Y}_T	refers to the position uncertainty estimation of the task domain
\mathbf{X}_T	wheel speed measurements of the four wheels in the task domain
\mathbf{Y}_S	refers to the position uncertainty estimation in the source domain
\mathbf{X}_S	wheel speed measurements of the four wheels in the source domain
\mathcal{X}	feature space
\mathcal{Y}	label space
\mathcal{X}_T	feature space of the target domain
\mathcal{Y}_T	label space of the target domain
\mathcal{X}_S	feature space of the source domain
\mathcal{Y}_S	label space of the source domain
$P(\mathbf{X})$	marginal probability distribution
$P(\mathbf{Y} \mathbf{X})$	objective predictive function
D_S	source domain
D_T	target domain
T_S	source task
T_T	target task
n	Transfer learning objective function

Chapter 1

Introduction

1.1 Importance of Autonomous Vehicles

It is estimated that the UK's Autonomous Vehicle (AV) market will be worth an approximate value of £28 billion by 2035 (Dowd 2019). A major motivation towards the development of these vehicles is the need to improve road safety. As human driving errors account for 75% of traffic-related road accidents in the UK, and 94% in the USA (Liu et al. 2019), AVs have the potential to reduce such road accidents (Papadoulis et al. 2019). Although AVs could introduce new kinds of accidents, there is the drive to ensure they are as safe as possible.

AVs acquire an understanding of their environment through the use of sensory systems (Babak et al. 2017). Ultrasonic systems, LIDARs and cameras are examples of such sensors that can be found on the outside of the vehicle. Several systems for data processing and analysis can also be found inside the vehicle, which use the sensor data to make decisions a human driver would normally make. Cameras and LIDARs are imaging systems used to identify objects, potential collision hazards, structures and pedestrians in the vehicle's trajectory (Onda et al. 2018). Cameras are furthermore essential to the identification of road markings and signs on structured roads. A good number of sophisticated versions of such systems are already employed, which proves the crucial role imaging systems play in the operation of AVs (Ahmed et al. 2019). Nevertheless, although the vehicle's environment can be assessed by imaging systems which can also determine markings or the position of objects relative to the vehicle, there is the need to continuously and robustly localise a vehicle

with reference to a defined coordinate system. Information on how the vehicle navigates through its environment is also needed such that real-time follow up decisions can be made.

1.2 GNSS (Global Navigation Satellite System) Issues

A GNSS receiver performs complex analysis on the signals received from at least 3 of the many satellites orbiting the earth and is known to be one of the best when it comes to position estimation, as it has no competition in terms of coverage or cost (Yao et al. 2017). Although GNSS is widely accepted, it is far from being a perfect localisation system. As there has to be a direct line of sight between the satellites and the GNSS antennae, there can be instances of GNSS failures in outdoor environments. GNSS can prove difficult to use in metropolitan cities and similar environments characterised by bridges, tall buildings, tunnels or dense tree canopies, as its line of sight may be blocked during signal transmission (Yao et al. 2017). More so, GNSS signal can be jammed; leaving the vehicle with no information about its position (Gerard O'Dwyer 2018). As such, a GNSS cannot act as a standalone navigation system.

The GNSS is used to localise the AV to a road. To achieve lane localisation, GNSS is combined with cameras, high accuracy LIDARs, High Definition (HD) maps and RADAR. However, there are cases when the camera and LIDAR could be uninformative or unavailable for use. The accuracy of low-cost LIDARs and cameras could be compromised during extreme weather conditions such as when there is heavy snow, fog, rain or sleet (Templeton 2017). This issue is well-recognised in the field. The cost of high accuracy LIDAR also makes them a theft attractive item as they are worth several thousands of pounds. Hence, the use of LIDARs on AVs would increase its cost. Camera-based positioning systems could also face low accuracies depending on the external light intensity of the vehicle's environment and the objects in the camera's scene. In level 4 self-driving applications, as tested by Waymo LLC and Cruise LLC (Lee Teschler 2018), the LIDAR scan is matched onto an HD map in real-time. Based on this, the system is able to precisely position the vehicle within its environment (Lee Teschler 2018). However, this method is computationally intensive.

Furthermore, changes to the driving environment and infrastructure could make an HD map temporarily obsolete and as such not useful for navigation.

Tesla which is well known for its no LIDAR and HD map policy handles GNSS signal outages by relying on its cameras and road markings until the GNSS signal become available. But the question is what happens if a decision is needed to be made on navigating to a new road during the signal loss or what happens when the GNSS signal is lost and the camera is uninformative? Also, Failure Mode and Effect Analysis (FMEA), which is an analysis performed to identify all the ways a system can fail and identify ways to mitigate them, would need to be performed on all the above failure scenarios to ensure the safe operation of AVs.

1.3 Navigation using Inertial Measurement Sensors

An Inertial Navigation Sensor (INS) however, unlike other sensors found in an AV, does not need to interact with its external environment to perform localisation, making it unique to the other sensors employed on the vehicle. This independence makes it vital for both sensor-fusion and safety. An Inertial Measuring Unit (IMU) measures a vehicle's linear acceleration and rotational rate components in the x , y and z -axis and computes positioning, velocity and orientation by continuously. It functions to provide localisation data; needed by the vehicle to position itself within its environment. As production vehicles are already equipped with anywhere from one-third to a full INS (OXTS 2016), the IMU can be used to localise the vehicle temporarily in the absence of the GNSS signals. The IMUs can also be used to compare positions and estimate in order to introduce certainty to the final localisation output. In the absence of an IMU, it would be difficult to know when the localisation accuracy of the LIDAR may have deteriorated (Lee Teschler 2018).

LIDAR scans are matched onto an HD map in real time in self driving applications tested by Google, Waymo and Cruise (Christoph Domke 2020). Based on this, the system is able to precisely position the vehicle within its environment. However, this method is computationally intensive. More so, IMU reduces the potential of the algorithm getting stuck in local minimum (Lee Teschler 2018). The use of high accuracy IMU has been proven to be a way to overcome the GNSS reliability issue. The significant cost of such IMU sensors has however hindered their ado-

ption on AVs. Even more, low cost IMU have accuracies too low to be used independently on AVs as they are plagued by noise and biases (Chen et al. 2018).

Through a complex mathematical analysis (see section 2.2 and 3.2.1), the position of the vehicle can be computed using the INS during the GNSS outage. However, the sensors are plagued by exponential error drifts manifested by the double integration of the acceleration to displacement. These errors are unboundedly cascaded over time, leading to a very poor positioning estimation. Commonly, the GNSS in what could be described as a mutually symbiotic relationship, calibrates the INS periodically during signal coverage in order to improve the positioning estimation accuracy. Traditionally, Kalman filters are used to model the error between the GNSS position and the INS position solution. These Kalman filters have shown limitations when modelling highly non-linear dependencies, non-Gaussian noise measurements and stochastic relationships.

Several researchers (Chiang et al. 2008; Dai et al. 2020; Fang et al. 2020; Noureldin et al. 2011) have recently studied the use of artificial neural networks techniques in place of Kalman filters to model the errors, as they are capable of learning non-linear relationships within the sensor's measurement. Machine learning techniques have proven to perform better in longer GNSS signal losses than Kalman filters (Noureldin et al. 2011).

Nevertheless, we observe that despite the number of machine learning based techniques investigated on the INS/GNSS error drift modelling, there lacks an investigation into the performances of the techniques on complex driving scenarios and environments experienced in everyday driving. Such scenarios range from hard brakes on regular, muddy or wet roads to heavy traffic, sharp cornering scenarios, roundabouts, etc.

We thus set out to investigate the performances of machine learning-based approaches on such complex driving environments and show that these scenarios prove rather more challenging for vehicular positioning.

1.4 Inertial Positioning using Wheel Encoder Sensors

Modern vehicles embed a good number of sensors, lending support to several advanced driver assistance systems. The anti-lock braking system (ABS) wheel speed sensor is an ego-motion sensor which has been investigated as an alternative to the INS for vehicular positioning (Merriaux et al. 2014). A wheel speed sensor (wheel encoder), which operates by measuring the speed of the vehicle's axle or wheel, can provide a better positioning solution compared to the accelerometer sensor of the INS. Indeed, the wheel speed sensor's measurements resolving involves less integration steps in the determination of the vehicles position, thus minimising the error propagated during the integration process. Nevertheless, the wheel speed sensor is not a perfect solution either. The accuracy of the sensor's measurement is affected by several factors such as wheel slippage and changes in the tyre size. A larger tyre diameter due to a tyre replacement, or an increase in tyre pressure, leads to an overestimation of the vehicle's displacement. Meanwhile, a smaller tyre diameter leads to the displacement of the vehicle being underestimated. There has been no study on the use of machine learning techniques to learn these uncertainties (characterised as epistemic due to lack of knowledge) in the wheel speed-based position estimation directly from the wheel encoder data. We thus for the first time, investigate the potential of deep neural networks to learn the uncertainty in the wheel speed measurement to improve the position estimation of AVs compared to the accelerometer-based approach.

1.5 Research challenges

There are a number of high-level challenges associated with this vehicular localisation research. Even though existing approaches have attempted to address the localisation problem with machine learning or analytical models, the robustness and accuracy of these methods have not been evaluated to the sufficient level of deployment in real life scenarios. This thesis aims to address issues faced in real world environments to attain a ubiquitous and dependable localisation of AVs in GNSS-deprived environments. These high-level challenges consist of:

1.5.1. Lack of a Publicly Available Dataset for Ego-motion Odometry

Low-cost inertial navigation sensors (INS) can be utilised for a dependable solution for tracking AVs in the absence of GNSS signals. Nevertheless, position errors

grow significantly over time due to noises in the sensor measurements. Although several researchers have proposed several techniques to learn the noise in the sensor's measurement, the absence of a robust and public standard dataset has obstructed the development in the research, adoption and evaluation of recent machine learning techniques such as deep learning process to learn the error in the INS for a more precise positioning of the vehicle. There is therefore the need for publicly accessible information rich dataset to expedite the benchmarking, estimation and fast development of positioning algorithms. In this thesis, we define ego-motion sensors as sensors that do not require interaction with the external environment to perform odometry.

1.5.2. Accuracy and Robustness

In real world navigation scenarios, usable localisation techniques need to demonstrate robustness and accuracy. Robust localisation method refers to its ability to accommodate disturbances and produce accurate estimations reliably and consistently across a wide variety of dynamic scenarios. Most existing techniques have used visual observations to proffer spectacular results in specific scenarios. However, vision-based models are faced with a number of real factors that reduce their efficiency for example, changing dynamics of the environment, occlusions of cameras and low light conditions. Contrastingly, the use of another sensor modality that is more rigid to environmental dynamics is far less investigated in vehicular localisation. An inertial sensor, which is totally egocentric and unperturbed by environmental disturbances is a good choice. For a complete robustness evaluation of position techniques for real world driving using inertial sensor data, their performance needs to be examined on all driving scenarios as can be found in everyday driving. The robustness of positioning techniques is an important issue for system reliability and safety. The metrics employed in measuring the robustness and accuracy of the positioning techniques in this thesis are defined in Section 3.2.3.1.

1.5.3. Adaptation to Vehicles with Different Domain Characteristics

A common cause for concern for data driven approaches is usually the ability to generalise models to a new vehicle. In scenarios where machine learning models are trained in a specific domain but deployed in another domain, the performance of the model degrades. In real life scenarios, quite a number of factors are influential to this degradation, from changes to the dynamics of the vehicle to new

pattern distribution of the sensor's noise and bias, will make the test sensor data vary from training data. Therefore, the challenge is to explore techniques that allow the trained machine learning models to spontaneously adjust into new vehicle domains.

1.6 Research Questions

In this research work, we examine how best to design and utilise machine learning approach for localisation to address the above challenges. The main research questions that we consider are as follows:

1.6.1. Question 1: How can deep learning improve vehicular localisation using inertial sensor data in complex driving environments?

Many studies on vehicular localisation using inertial sensor data focus more on non-complex driving conditions which are not consistent with everyday driving. However, the everyday drive of AVs, involves navigation in complex driving environments. These complex driving environments include hard brake, roundabout, sharp cornering, etc. It is not known if machine learning is able to improve inertial localisation in such challenging scenarios. Moreover, there is no publicly available dataset with such complex driving scenarios from noisy ego-motion sensors to train and evaluate the inertial tracking model. Deep learning has proven to be effective at learning high level abstractions from ego-motion sensor modalities. This research will therefore gather noisy ego-motion sensor data and investigate the potential of deep learning to improve inertial localisation in such driving scenarios.

1.6.2. Question 2: How can deep learning be used to improve on localisation with wheel encoder data comparatively to inertial sensor data in challenging environments?

Inertial navigation sensors are plagued with noises which grow exponentially through time during the double integration from acceleration to position. Wheel encoders provide the information on the speed of the wheels and require one less integration step compared to the accelerometer of the INS to estimate the vehicle's position. There are no studies on the use of machine learning to improve localisation using wheel encoder data. We therefore investigate the potential of deep learning to improve localisation using wheel encoder data. We also comparatively analyse the performance of machine learning based wheel encoder localisation to machine learning

based accelerometer localisation to determine which approach provides a robust and accurate positioning estimation.

1.6.3. Question 3: How can deep learning be used to improve localisation in longer term GNSS outages?

GNSS outages are typical in environments characterised by dense tree canopies, tunnels, bridges, valleys, etc. These outages could last as long as 180s and could be more in longer tunnels. Very few works have considered the use of deep learning to improve localisation in such long-term outage scenarios. As the sensor noise grows exponentially over time, we set out to investigate the potential of deep learning to capture this exponential error growth to provide a more dependable and accurate positioning solution.

1.6.4. Question 4: How can deep learning localisation models be adapted to vehicles with different error feature characteristics and vehicular state and dynamics?

The training of a deep learning model on a particular domain commonly leads to an over-fit on that specific data distribution and is likely to generalise poorly to a new domain. Ego-motion sensor datasets are usually specific to the vehicle used in collecting the data. However, vehicular characteristics such as vehicular dynamics and vehicular state (tyre pressure, worn out state of the tyres, vehicular size, etc.) vary from vehicle to vehicle, the period of use, etc. As such, a model trained on a specific vehicle will not generalise to accurately learn the position estimation uncertainties present in other vehicles. We therefore investigate the potential of transfer learning to adapt the position estimation model to the new vehicle domains in which the deep learning model is deployed.

1.7 Contributions

The contributions of this thesis are summarised below.

Contribution 1: Chapter 4 addresses question 1 by formulating the structure of the deep learning model analogously to the operation of the feedback control system and we propose the AccNet (Accelerometer-based position estimation neural Network) to feed positioning information from the previous time stamps of the vehicle's position to provide a better controlled and improved estimation in challenging driving scenarios. We also propose the GyroNet (Gyroscope-based orientation rate estimation neural

Network model), to learn noises in the gyroscope sensor of the INS to provide an improved estimation of the orientation rate of the vehicle. We show that the scenarios such as roundabouts, hard brakes and successive left and right turns etc., are challenging for the accelerometer and gyroscope physics models and that deep learning-based models are able to improve the position and orientation rate of the inertial sensors to provide a robust and accurate localisation output. We also released the first of its kind large scale and information rich ego-motion dataset for vehicular localisation called Inertial Odometry Vehicle Navigation Benchmark Dataset (IO-VNBD) for training and evaluating learning-based ego-motion odometry. These contributions are published in:

Onyekpe, U., Kanarachos, S., Palade, V., & Christopoulos, S.-R. G. (2020). '*Vehicular Localisation at High and Low Estimation Rates during GNSS Outages: A Deep Learning Approach*'. in Deep Learning Applications, Volume 2, Arif Wani, Taghi Khoshgoftaar, Vasile Palade, Ed. Advances in Intelligent Systems and Computing, vol 1232. (pp. 229–248). Springer Singapore. https://doi.org/10.1007/978-981-15-6759-9_10

Onyekpe, U., Palade, V., Kanarachos, S., & Szkolnik, A. (2021). '*IO-VNBD: Inertial and odometry benchmark dataset for ground vehicle positioning*'. Data in Brief, 35, 106885. <https://doi.org/10.1016/j.dib.2021.106885>

Onyekpe, U., Palade, V., & Kanarachos, S. (2021). '*Learning to Localise Automated Vehicles in Challenging Environments Using Inertial Navigation Systems (INS)*'. Applied Sciences 2021, Vol. 11, Page 1270, 11(3), 1270. <https://doi.org/10.3390/app11031270>

Contribution 2: Question 2 is addressed by the formulation of Wheel Odometry neural Network (WhONet) in Chapter 4, however the WhONet model is described in Chapter 3. WhONet is evaluated on several challenging scenarios showing impressive performances and then analysed comparatively to the AccNet, showing that it can provide a more robust and accurate position estimation compared to AccNet, an accelerometer based neural network. These contributions are described in the publications below:

Onyekpe, U., Kanarachos, S., Palade, V., & Christopoulos, S.-R. G. (2020b). '*Learning Uncertainties in Wheel Odometry for Vehicular Localisation in GNSS Deprived Environ-*

ments'. International Conference on Machine Learning Applications (ICMLA), 741–746.

<https://doi.org/10.1109/ICMLA51294.2020.00121>

Onyekpe, U., Palade, V., Herath, A., Kanarachos, S., Fitzpatrick, M. E. (2021) '*WhONet : Wheel Odometry Neural Network for Vehicular Localisation in GNSS-Deprived Environments*'. Engineering Applications of Artificial Intelligence, Vol. 105, <https://doi.org/10.1016/j.engappai.2021.104421>.

Contribution 3: Question 3 is addressed by evaluating the WhONet Model on several test sequences over 490 km. The test sequences are broken down into different scenarios of 30s, 60s, 120s, and 180s. We show that the WhONet is able to capture the noise within the wheel encoder sensor to limit the exponential error growth over time to provide a more robust and accurate position estimation. These contributions are described in the publications below:

Onyekpe, U., Palade, V., Herath, A., Kanarachos, S., Fitzpatrick, M. E. (2021) '*WhONet : Wheel Odometry Neural Network for Vehicular Localisation in GNSS-Deprived Environments*'. Engineering Applications of Artificial Intelligence, Vol. 105, <https://doi.org/10.1016/j.engappai.2021.104421>.

Contribution 4: Question 4 is addressed in chapter 6 by proposing a recalibration model based on transfer learning that adapts the WhONet model from its source domain to the task domain of a new vehicle. Our framework improves the generalization of WhONet to other vehicle domains. These contributions are described in the publications below:

Onyekpe, U., Szkolnik, A., Palade, V., Kanarachos, S. & Fitzpatrick, M. E., (2021). '*R-WhONet: Recalibrated Wheel Odometry Neural Network for New Vehicle Domain Adaptation of Vehicular Position Model using transfer learning*'. International Journal of Robotics Research (Submitted).

During my PhD study, I also contributed to some other research publications as shown below. As these were contributions to similar research fields but not at the core of my PhD research, they will not be discussed further in this thesis.

Onyekpe, U., Kanarachos, S., & Fitzpatrick, M. E. (2019). '*Spontaneous Fruit Fly Optimisation for truss weight minimisation: Performance evaluation based on the no free lunch*

theorem'. International Conference on Sustainable Material and Energy Technologies (ICSMET), 2019.

Onyekpe, U., Palade, V., Kanarachos, S., & Christopoulos, S.-R. G. (2021). 'A Quaternion Gated Recurrent Unit Neural Network for Sensor Fusion. *Information*', 12(3), 117. <https://doi.org/10.3390/info12030117>

Mahmoud, A., Ahmad, Z., Onyekpe, U., Almadani, Y., Ijaz, M., Haas, O., Rajbhandari, S. 'Autonomous Vehicle Positioning with Visible Light Communication using Artificial Neural Networks.' *Journal of Electronics* (under review, second round).

1.8 Thesis outline

This thesis is structured as follows:

Chapter 2 provides an overview of the background for this research. The chapter discusses conventional solutions used in vehicular localisation, coordinate systems used in positioning as well as existing learning based localisation methods.

Chapter 3 introduces the Inertial Odometry Vehicular Navigation Benchmark Dataset (IO-VNBD) and proposes several deep learning and physics-based localisation models for vehicular positioning.

Chapter 4 analyses the performance of the deep learning and physics-based odometry models for position and orientation rate estimation in challenging driving environments. The chapter analysis the potential of the deep learning models to learn the noise in the accelerometer, gyroscope and wheel encoder to provide an accurate localisation information in complex scenarios such as roundabout, wet road, successive left and right turns and sharp cornering, motorway, quick changes in acceleration and hard brake.

Chapter 5 investigates the performance of the WhONet model comparatively to its corresponding physics model for continuous positioning in longer term GNSS outages.

Chapter 6 presents a recalibration model which uses transfer learning to adapt the WhONet's model to vehicles with different dynamics and states.

Finally, Chapter 7 summarises the overall conclusions and suggests directions for future works.

Table 1. Publications from this thesis

No	Publications from this thesis
1	Onyekpe, U., Kanarachos, S., Palade, V., & Christopoulos, S.-R. G. (2020). <i>'Vehicular Localisation at High and Low Estimation Rates during GNSS Outages: A Deep Learning Approach'</i> . in Deep Learning Applications, Volume 2, Arif Wani, Taghi Khoshgoftaar, Vasile Palade,, Ed. Advances in Intelligent Systems and Computing, vol 1232. (pp. 229–248). Springer Singapore. https://doi.org/10.1007/978-981-15-6759-9_10
2	Onyekpe, U., Palade, V., Kanarachos, S., & Szkolnik, A. (2021). <i>'IO-VNBD: Inertial and odometry benchmark dataset for ground vehicle positioning'</i> . Data in Brief, 35, 106885. https://doi.org/10.1016/j.dib.2021.106885
3	Onyekpe, U., Palade, V., & Kanarachos, S. (2021). <i>'Learning to Localise Automated Vehicles in Challenging Environments Using Inertial Navigation Systems (INS)'</i> . Applied Sciences 2021, Vol. 11, Page 1270, 11(3), 1270. https://doi.org/10.3390/app11031270
4	Onyekpe, U., Kanarachos, S., Palade, V., & Christopoulos, S.-R. G. (2020b). <i>'Learning Uncertainties in Wheel Odometry for Vehicular Localisation in GNSS Deprived Environments'</i> . International Conference on Machine Learning Applications (ICMLA), 741–746. https://doi.org/10.1109/ICMLA51294.2020.00121
5	Onyekpe, U., Palade, V., Herath, A., Kanarachos, S., Fitzpatrick, M. E. (2021) <i>'WhONet : Wheel Odometry Neural Network for Vehicular Localisation in GNSS-Deprived Environments'</i> . Engineering Applications of Artificial Intelligence, Vol. 105, https://doi.org/10.1016/j.engappai.2021.104421 .
6	Onyekpe, U., Szkolnik, A., Palade, V., Kanarachos, S. & Fitzpatrick, M. E., (2021). <i>'R-WhONet: Recalibrated Wheel Odometry Neural Network for New Vehicle Domain Adaptation of Vehicular Position Model using transfer learning'</i> . International Journal of Robotics Research (Submitted).

Chapter 2

Background and Literature Review on Positioning Techniques

This chapter provides an overview of conventional localisation solutions, basic concepts related to this research and recent advances in machine learning with respect to vehicle positioning using INS and wheel odometry.

2.1. Land Vehicular Positioning techniques

2.1.1. Global Navigation Satellite Systems (GNSS)

GNSS has been successfully used in position and navigation applications for over two decades. The TRANSIT developed by the United States which used the doppler effect to localise a vehicle was the first GNSS created. The most sophisticated systems in place at the moment are the American GPS (Global Positioning System), Russian GLONASS (Global Navigation Satellite System), Chinese BEIDOU and European GALILEO. The GPS is the main positioning system used in vehicles. It uses signals from at least 3 satellites with known positions to compute positioning. Nevertheless, signal blockage in urban canyons, under dense tree canopies, under bridges and in tunnels affects its accuracy (K. Chiang 2004; Dai et al. 2020; Fang et al. 2020; Noureldin et al. 2011). The errors associated with the use of the GPS signal include: ephemeris error, satellite clock error, multipath error and signal jamming.

2.1.2. Dead Reckoning (DR) Systems

The Dead Reckoning (DR) System operates on the principle of relative position fixing using information on the vehicle's starting point, subsequent direction and speed to determine its present position. A DR system could consist of a wheel odometer that provides information on the vehicle's speed or an accelerometer that provides information on the vehicle's acceleration and a compass or a single-axis gyroscope providing information on the vehicles pitch or heading. DR systems are less expensive but due to their incremental update nature, errors in the estimation increase with every distance travelled. Two main dead reckoning systems are the Inertial Navigation System (INS) and wheel odometry-based system.

2.1.2.1. Inertial Navigation System (INS)

An Inertial Measuring Unit (IMU) usually consists of a three orthogonal axis accelerometer and a three orthogonal axis gyroscope.

Accelerometer - The accelerometer measures the vehicles acceleration in the x, y and z-axis. It measures the specific force f on the sensor in the body frame b (K. Chiang, 2004). This can be expressed as $f^b = R^{bn}(a^n - g^n)$, where R^{bn} is the rotation matrix from the navigation frame to the body frame, g^n represents the gravity vector and a^n denotes the linear acceleration of the sensor expressed in the navigation frame (Kok et al., 2017). The vehicle's linear acceleration in the navigation frame can be broken down as shown in Equation (2.1).

$$a^n = a_n^b + 2\omega_{ie}^n + V_n^n + \omega_{ie}^n + \omega_{ie}^n + p^n \quad (2.1)$$

Where a_n^b is the acceleration of interest, $2\omega_{ie}^n + V_n^n$ is the Coriolis acceleration and $\omega_{ie}^n + \omega_{ie}^n + p^n$ is the centrifugal acceleration.

Gyroscope – The gyroscope measures the attitude change in roll, yaw and pitch. It measures the angular velocity of the body frame (vehicle's frame) with respect to the inertial frame as expressed in the body frame. Represented by ω_{ib}^b , the attitude rate can be expressed as shown in Equation (2.2).

$$\omega_{ib}^b = R^{bn}(\omega_{ie}^n + \omega_{en}^n) + \omega_{nb}^b \quad (2.2)$$

Where ω_{ie}^n is the angular velocity of the earth's frame with respect to the inertial frame and estimated to be approximately $7.29 \cdot 10^{-5}$ rad/s (Kok et al. 2017). The navigation frame is defined stationary with respect to the earth, thus $\omega_{en}^n = 0$ and the angular velocity of interest ω_{nb}^b representing the orientation of the vehicle in the navigation frame. If initial conditions are known, ω_{nb}^b may be integrated over time to determine the vehicle's orientation. The steps involved in determining the position of the vehicle from the INS is as shown in Figure 2.1, more details can be found in Section 3.2.2.1a.

This item has been removed due to 3rd Party Copyright. The unabridged version of the thesis can be found in the Lanchester Library, Coventry University.

Figure 2.1 Dead-reckoning; showing the integration of the INS's measurement to position (Kok et al., 2017).

INS errors - Some of the errors associated with the use of the inertial navigation system are highlighted below:

- **Input Range** – This refers to the maximum acceleration or angular rate the IMU can meaningfully measure. Any motion outside this range would either produce a bad measurement or no measurement at all. More so, when vibrations occur, it is very hard to isolate the true signals from the vibration thus leading to poor measurements.
 - **Bias** – Bias can be said to be an offset to the sensor output given a certain physical input. Generally, it could exist in two ways as described below.
 - **Bias Repeatability (turn-on to turn-off bias)** – It is observed that for every power up of the IMU the initial bias is different due to changes in the initial conditions of signal processing and physical properties of the IMU.

- Bias Stability (in-run bias) – Bias Stability error occurs after the IMU is powered on. The initial bias changes over time due to temperature, time and mechanical stress on the system
- Scale Factor – Scale Factor error occurs due to the relationship between the input and the output. When the actual output is as a result of a linear effect, an error in the input would result in an output proportional to the input but scaled.
- Random Walk - There is always a random noise present when a constant signal is measured by the sensor. The random noise is a stochastic process which is minimised using statistical techniques. The presence of the random walk error in the sensor output leads to a random walk its application.
- Sensor Non-Orthogonality – Sensor Non-Orthogonality refers to the mounting errors of the accelerometers and the gyroscope. The three accelerometers and three gyroscopes are mounted orthogonally in all three axis. However, if the axis are not mounted perfectly at 90 degrees, errors exists.
- Timing errors – This refers to the time difference of measurement between the GNSS and the IMU.

Other positioning techniques used in time past include: Magnetic Compass, Electronic Navigation System and Radio-based navigation System.

2.1.2.2. Wheel Odometer (WO)

Embedded in modern vehicles are a good number of sensors supporting advanced driverless systems such as the wheel encoder for anti-lock braking systems. The wheel encoder operates by measuring the speed of the vehicle's axle or wheel. However, wheel odometry is better in position estimation compared to the accelerometer of the INS. It requires lesser number of integration steps to determine the position of a vehicle, thus minimising the error propagation and making it a desirable and simpler approach. Figure 2.2 shows the operating principles of the WO/INS system (which refers to a system comprising of a gyroscope and a wheel odometer as a replacement to the accelerometer of the INS). More, details about the operation of the WO/INS system can be found in Section 3.2.2.1c.

The wheel speed measurement can be broken down as shown in Equation 2.3, where \hat{w}_{wh}^b is the speed of the wheel in the body frame, w_{wh}^b is the noise free wheel speed measurement and ε_{wh}^b is the uncertainty in the wheel encoder's measurement.

$$\hat{w}_{wh}^b = w_{wh}^b + \varepsilon_{wh}^b \quad (2.3)$$

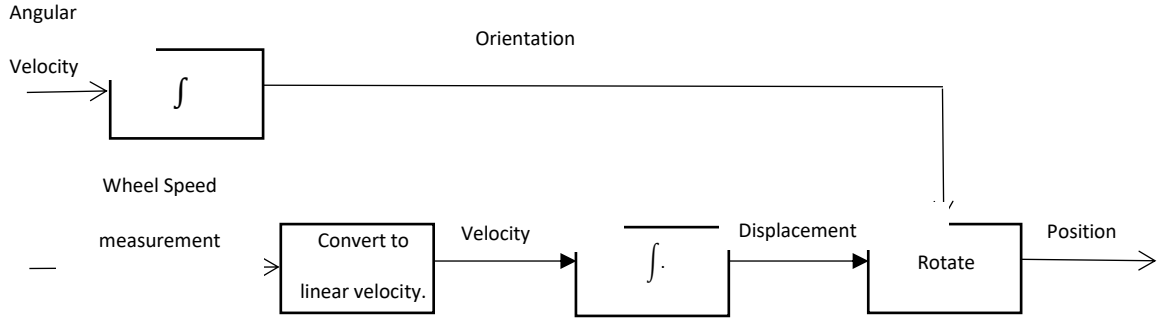


Figure 2.2. Dead reckoning; showing the integration of the WO/INS's measurement to position.

• Wheel Odometry Errors

However, wheel odometry can also accumulate errors due to internal systematic factors and non-systematic factors (Borenstein & Feng 1996; Huang et al. 2015).

Borenstein et.al. in (Borenstein & Feng 1996) based his experiments on systematic errors using differential drive robots and came to the conclusion that “unequal wheel diameters,” “uncertainty about the wheelbase,” and the “difference between the actual and the nominal wheel diameters” are the most common and important systematic error sources. But according to (Borenstein & Feng 1996), these parameters do not cause errors in all driving scenarios. For instance, unequal wheel diameter causes error in straight line motion and wheelbase uncertainty causes error only when turning. Borenstein et.al. further reveal that non-systemic errors such as travel on uneven road surfaces and wheel slippage due to wet and slippery roads, over-acceleration, fast turning (skidding), etc. can also cause uncertainties in wheel odometry. While addressing wheel odometry errors from differences in actual and nominal tyre sizes, in (Onyekpe et al. 2020b), we show that the use of a different tyre pressure than the recommended pressure or replacing tyres with a slightly different tyre diameter can lead to errors in vehicle displacements in odometry. A larger tyre diameter will overestimate the vehicle's displacement while a smaller tyre diameter can underestimate it.

2.1.3. Multi-sensor Augmented Positioning Systems

It is quite common for a stand-alone navigation system to fall short of the accuracy requirement needed for positioning. In such situations, an augmentation of

several sensors to address the limitations of each stand-alone system is preferred. The augmented system can exist as a single high-precision system with characteristics as presented on Table 2.1.

Table 2.1. The requirements of a positioning system

Positioning system requirement	Description
Cost Effective	The sensors must have the best balance between performance and cost.
Continuous Positioning	The system must be able to provide positioning information at all times no matter the environment.
Robust	The ability of the positioning system to be reliable all the time.
Global function	The ability of the system to work anywhere in the world

2.1.3.1. WO/INS and GPS Integration

Modern vehicular navigation systems mostly depend on information provided by the GNSS receiver for positioning. The GNSS can provide positioning information to an unlimited number of users worldwide and as such is widely used in applications which track people, phones, cars, ships, planes, etc. However, the GNSS can only provide precise positioning information under ideal conditions and requires an open environment for unhindered signal transmission. As such, the GNSS doesn't function well around tall buildings, under dense tree canopies, under bridges, in tunnels, etc. This creates the need for GNSS to be integrated with other relevant sensors to cover the periods in which the GNSS signal is unreliable, thus ensuring the provision of continuous position information for navigation.

The INS is a stand-alone system that measures the vehicle's acceleration and angular rates continuously to determine its position and orientation (Jekeli 2012). The wheel odometer on the other hand measures the speed of the vehicles wheels to continuously estimate the vehicles position. The advantage to the use of the WO/INS is that it is able to provide rich information on the vehicle's dynamics due to its high update rate. However, a disadvantage to the use of the INS or WO is in the error accumulation over time due to the double integration of the accelerometer's measurements, single

integration of the gyroscope's measurement or single integration of the wheel speed measurement. Furthermore, misalignment errors project the impact of gravity onto the horizontal plane. The errors grow exponentially as a function of time which makes these systems only able to provide accurate information for a limited time without an external aid.

The use of an integrated system enhances the performance of the navigation system compared to the stand-alone WO/INS or GPS in a way that attempts to overcome each individual system's limitations. An integrated system provides an enhanced navigation system that has superior performance in comparison to either a stand-alone GPS or WO/INS as it can overcome each of their individual limitations. For example, the position and velocity information derived from the GNSS can act as an external aid to update the INS for long-term accuracy improvement. The WO/INS on the other hand, can provide precise positioning information to cover the gap created by the GNSS outage. A performance comparison between the INS, GNSS and the integrated system is provided in Table 2.2. Table 2.3 gives more information on the accuracy requirement for land vehicles.

Table 2.2. Comparison of the WO/ INS, GPS and the integrated WO/INS/GPS system

	WO/INS	GPS	WO/INS/GPS
Advantages	High short-term positional accuracy No signal outage High data output rate.	High long-term position accuracy. Not influenced by gravity. Positional accuracy is independent of time.	High position accuracy at all times (including during GNSS outages). High data output rate. Resistant to jamming.
Disadvantages	Deteriorating accuracy with time. Affected by the influence of gravity. Needs initial and inflight calibration and alignment.	Low data output rate Signal outages. Deteriorating accuracy in certain environments.	Deteriorating accuracy with time. Needs initial and inflight calibration and alignment (for the gyroscope).

Table 2.3. Requirement for land positioning systems in urban areas (Krakiwsky 1994 and Hofmann-Wellenhof et al. 2003), (K. Chiang 2004).

Vehicle Type	Accuracy (m) 2D-95% confidence interval
Autonomous cars	2-5
Taxi car	10-200
Urban Transit buses	20-50
Inter city buses	50-200
Ambulances	10-20
Police cars	10-20
Utility truck	20-50

2.2. Coordinate Systems

Several coordinate systems are used in navigation, with the positioning result expressed relative to a reference. Each navigation sensor also has its measurements resolved with respect to a certain co-ordinate frame. Usually, the sensor's coordinate system would need to be converted to the navigation frame (Kok et al. 2017). Some of the co-ordinate systems are discussed below:

2.2.1. Inertial Frame

The inertial frame has its origin coincident with the centre of mass of the earth. As such, its axis does not rotate with respect to fixed celestial bodies. Its x-axis is directed towards the mean vernal equinox, its z-axis is parallel to the earth's rotational axis and its y-axis completes the orthogonal frame as shown in Figure 2.3 (K. Chiang 2004).

This item has been removed due to 3rd Party Copyright. The unabridged version of the thesis can be found in the Lanchester Library, Coventry University.

2.2.2. Earth Fixed Frame

Similar to the inertial frame, the earth's fixed frame has its origin coincident with the earth's centre of mass. Its x-axis however points towards the mean Greenwich meridian as shown on Figure 2.4. The earth's frame mainly differs from the inertial frame by a mean constant angular rotation of the earth. Equation (2.4) expresses the direction cosine matrix from the earth frame to the inertial frame (K. Chiang 2004).

$$\mathbf{R}^{ie} = \begin{bmatrix} \cos w_e t & -\sin w_e t & 0 \\ \sin w_e t & \cos w_e t & 0 \\ 0 & 0 & 1 \end{bmatrix} \quad (2.4)$$

Where \mathbf{R}^{ie} is the direction cosine matrix or rotation matrix, transforming measurements from the earth frame to the inertial frame, w_e is the constant angular velocity of the earth about the z-axis.

This item has been removed due to 3rd Party Copyright. The unabridged version of the thesis can be found in the Lanchester Library, Coventry University.

Figure 2.4 Earth fixed frame (K. Chiang, 2004).

2.2.3. Body (Sensor) Frame

The body frame has its axis coincident with the sensors input axis. The direction matrix cosine from the body frame to the navigation frame is expressed in Equations (2.5 and 2.6) (K. Chiang 2004). The IMU's outputs are the components of the acceleration and the rotation rate, the sensor block experiences along the body axes. Figure 2.5 shows the axes on the body frame.

$$\mathbf{R}^{nb} = \begin{bmatrix} \cos \Psi & -\sin \Psi & 0 \\ \sin \Psi & \cos \Psi & 0 \\ 0 & 0 & 1 \end{bmatrix} \begin{bmatrix} \cos \theta & 0 & \sin \theta \\ 0 & 1 & 0 \\ -\sin \theta & 0 & \cos \theta \end{bmatrix} \begin{bmatrix} 1 & 0 & 0 \\ 0 & \cos \phi & -\sin \phi \\ 0 & \sin \phi & \cos \phi \end{bmatrix} \quad (2.5)$$

$$\mathbf{R}^{nb} = \begin{bmatrix} \cos \theta \cos \Psi & -\cos \theta \sin \Psi + \sin \phi \sin \theta \cos \Psi & \sin \phi \sin \Psi + \cos \phi \sin \theta \cos \Psi \\ \cos \theta \sin \Psi & \cos \phi \cos \Psi + \sin \phi \sin \theta \sin \Psi & -\sin \phi \cos \Psi + \cos \phi \sin \theta \sin \Psi \\ -\sin \theta & \sin \phi \cos \theta & \cos \phi \cos \theta \end{bmatrix} \quad (2.6)$$

Where R^{bn} is the rotation matrix transforming the measurements from the body frame to the navigation frame, ϕ is the roll, θ is the pitch and ψ is the yaw.

This item has been removed due to 3rd Party Copyright. The unabridged version of the thesis can be found in the Lanchester Library, Coventry University.

Figure 2.5. Body frame axis.

2.2.4. Navigation Frame

The navigation frame also known as the local frame has its origin in the sensor frames origin. Its x-axis points towards the geodetic north, the z-axis orthogonal to the ellipsoidal plane and the y-axis completing the orthogonal frame (K. Chiang 2004).

2.3. Machine Learning Based Localisation Models. Review, Limitations and Challenges

2.3.1. Kalman Filters

Traditionally, Kalman filters (considered a machine learning technique according to (Russell and Norvig 2010)) are used to perform WO/INS/GPS integration. The Kalman filter is used to estimate a linear system's instantaneous state affected by Gaussian white noise. It has become a standard technique for use in WO/INS/GPS applications (K. Chiang 2004). Despite the wide popularity of the Kalman filter, it does possess some drawbacks. For an WO/INS/GPS integrated application, the Kalman filter requires stochastic models to represent the INS errors, but this stochastic models are difficult to determine for most gyroscope and accelerometers (Kai-Wei Chiang & El-Sheimy 2002).

Additionally, there is the need for an accurate a priori information of the covariant matrices of the noises associated with the WO/INS. More so, the WO/INS/GPS problem is one of a non-linear nature. As a result, other types of filters have been studied (K. Chiang 2004).

The limitations of the Kalman filter are discussed in subsequent paragraphs.

2.3.1.1. Model Dependency

The design of a Kalman filter model begins with the creation of a “true error model” which has its order reduced based on prior knowledge of the properties of the system, covariance analysis and knowledge of the physics of the problem (Salychev et al. 2000).

The motion model is usually dependent on the error models of the position error, velocity error and attitude error. These errors are supported by error states such as the accelerometer bias and the gyroscope drift which can be modelled stochastically using the first Gauss Markov or random walk (Rogers 2003). Indeed, there are several errors associated with the INS such as white noise, bias instability, correlated random noise, etc (NovAtel 2014). The variety of these errors makes it difficult to create a single stochastic model that works for all INS's in all environments whilst taking into consideration the long-term behaviour of the sensors. Unfortunately, the Kalman filter model is unable to provide this.

2.3.1.2. Prior Knowledge Dependency

As discussed in previous paragraphs, the Kalman filter requires initial knowledge such as the measurement design matrix, measurement noise covariant matrix (R), state transition matrix, the system noise covariance matrix (Q) and the noise coefficient matrix. The quality of the Kalman filter estimations in the INS/GPS system is majorly dependent on the Q and R matrices. These matrices are however not easy to determine, require tuning for optimal performance (as such require the services of an expert on the systems) and are time consuming. This challenge thus makes the Kalman filter an undesirable tool for use in INS/GPS systems. A dynamic model capable of learning with little

intervention to adapt itself to several environments will be desirable.

2.3.1.3. Linearisation Dependency

The errors characterising the WO/INS/GPS systems are nonlinear in nature. The Kalman filter on the other hand estimates the linear dynamical model using stochastic data and a recursive algorithm. As such the dynamic model of the GPS and INS are usually linearised (G. Chen 1992). The linearisation process involves the use of a first order approximation process that leads to deviations between the real error model and the assumed error model. The use of a technique that accounts for the non-linearity of the error is therefore preferable.

2.3.2. Machine Learning Techniques for Vehicle Positioning

The use of other machine learning techniques in place of Kalman filters to model the errors has been recently explored by some researchers, as they are capable of learning non-linear relationships within the sensor's measurements. Compared to Kalman filters, deep learning techniques have proven to perform better in longer GPS signal outage scenarios. The use of the sigma pi neural network on the positioning problem was explored by Malleswaran et al. in (Malleswaran et al. 2013). Nouredin et al. investigated the use of the Input Delay Neural Network (IDNN) to model the INS/GPS positional error (Nouredin et al. 2011). A Multi-Layer Feed-Forward Neural Network (MFNN) was applied in (K-W. Chiang 2003) on a single point positioning INS/GPS integrated architecture. In (Sharaf et al. 2005), they employed the MFNN on an integrated tactical grade INS and a Differential GPS architecture for a better position estimation solution. More so, Recurrent Neural Networks, which are distinguishable from other neural networks due to their ability to make nodal connections in temporal sequences, have been proven to model the time-dependent error drift of the INS more accurately compared to other neural network techniques (Dai et al. 2019). In (Fang et al. 2020), they compared the performance of the Long Short-Term Memory (LSTM) algorithm to the Multi-Layer Perceptron (MLP) and showed the superiority of the LSTM over the MLP. Similarly, in (Onyekpe et al. 2020a), we investigated the performance of the LSTM algorithm for high data rate positioning and compared it to other techniques, such as the IDNN,

MLP and Kalman filter. The performance of the techniques as demonstrated in published literatures, highlights the potential of intelligent algorithms in autonomous vehicle navigation. More so, a direct comparison of the performances of these techniques is not possible as information of the vehicle's dynamics studied are not publicly available.

2.3.3. Machine Learning Techniques used in this Thesis

The machine learning algorithms used in this thesis are discussed in this section.

2.3.3.1. MLNN - Multi Layer Neural Network

An MLNN consists of an interconnected system of neurons with the ability to map non-linear relationships between the input and output vector. This capability is particularly of interest as the dynamics of vehicles are non-linear in nature. The neurons are connected by weights, with the output defined by a function of the sum of the neuron's input and transformed non-linearly through an activation function. The neuron's input is computed from the product of a randomly initialised weight factor matrix and the input matrix, and a randomly initialised bias. The output from a neuron layer becomes the input to the neuron in the next layer. Through the continuous backpropagation of error signals, the weights are adjusted in what is referred to as the training phase of the MLNN. An adjustable learning rate and momentum can be used to prevent the MLNN from getting trapped in a local minimum while back-propagating the errors (Gardner & Dorling 1998).

The feed-forward operation is governed by:

$$\mathbf{y}_t = \sigma_f(\Sigma \mathbf{x}_t \mathbf{W} + \mathbf{b}) \quad (2.7)$$

Where \mathbf{y}_t is the output vector at time t ; \mathbf{x}_t is the input vector at time t ; \mathbf{W} is the weight matrix \mathbf{b} is the bias vector and σ_f is the sigmoid activation (non-linearity) function.

2.3.3.2. RNN - Recurrent Neural Networks

The success of Recurrent Neural Networks (RNNs) on sequentially based problems has been emphasised in applications such as natural language processing, financial analysis and signal processing problems (El-Moneim et al. 2020; Mao et al. 2019; Purohit et al. 2019; Senturk et al. 2018; Tsang et al. 2018). Other researchers have demonstrated the excellent performance of RNNs on various time series problems such

as on electronic health records (Rajkomar et al. 2018), classifications of acoustic scenes (Nwe et al. 2018), cyber-security (Susto et al. 2018), human activity recognition (Nweke et al. 2018; Wang et al. 2019), and vehicular localisation (Brossard et al. 2020; C. Chen et al. 2018; Dai et al. 2019; Fang et al. 2020). RNNs mainly differ from other neural networks by their ability to take time-based or sequential relationships into account. They are characterised by feedback loops connecting relationships learnt in the past, these connections are sometimes referred to as memory. The sequential information learnt is stored within the RNNs hidden state which extends to as many timesteps whilst it cascades forward in mapping relationships in each observation. The equations governing the operation of the RNN are presented in Equations (2.8 and 2.9).

$$\mathbf{h}_t = \tanh(\mathbf{U}_h \mathbf{h}_{t-1} + \mathbf{W}_x \mathbf{x}_t + \mathbf{b}_h) \quad (2.8)$$

$$\mathbf{y}_t = \sigma_f(\mathbf{W}_o \mathbf{h}_t + \mathbf{b}_o) \quad (2.9)$$

where \mathbf{h}_{t-1} is the previous state, \mathbf{U}_h , \mathbf{W}_x and \mathbf{W}_o are the hidden; input and output weight matrix respectively; \mathbf{b}_h and \mathbf{b}_o are the bias vector of the hidden and output layer respectively; \mathbf{y}_t is the output vector of the network. Figure 2.6 shows the RNN's unrolled architecture.

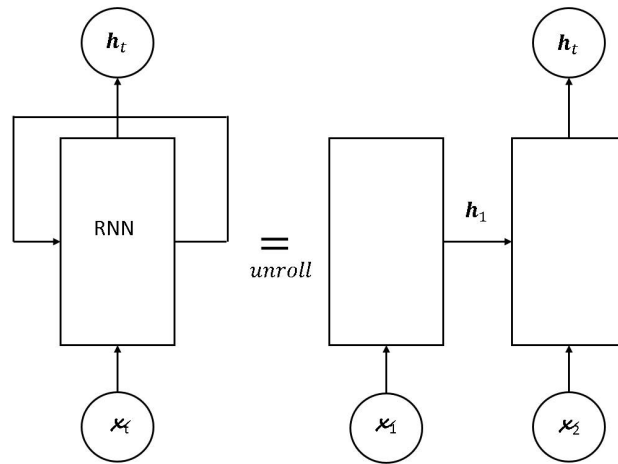


Figure 2.6 Unrolled RNN architecture

2.3.3.3. LSTM - Long Short-Term Neural Networks

Long Short-Term Memory (LSTM) are a variant of RNN created to tackle its shortfall (Hochreiter & Schmidhuber 1997). They are specifically created to solve the long-term dependency problem, hence enabling them to recall information for long periods of time (Gers et al. 2000; Graves & Schmidhuber 2005). Due to the accumulative and patterned nature of the INS positional errors, the LSTM can be used to learn error patterns from

previous sequences to provide a better position estimation. The operation of the LSTM is regulated by gates; the forget, input and output gates, and it operates as shown below:

$$f_t = \sigma_f(W_f \mathbf{x}_t + U_f \mathbf{h}_{t-1} + b_f) \quad (2.10)$$

$$i_t = \sigma_i(W_i \mathbf{x}_t + U_i \mathbf{h}_{t-1} + b_i) \quad (2.11)$$

$$\hat{c}_t = \tanh(W_c \mathbf{x}_t + U_c \mathbf{h}_{t-1} + b_c) \quad (2.12)$$

$$c_t = f_t * c_{t-1} + i_t * \hat{c}_t \quad (2.13)$$

$$o_t = \sigma_o(W_o \mathbf{x}_t + U_o \mathbf{h}_{t-1} + b_o) \quad (2.14)$$

$$\mathbf{h}_t = o_t * \tanh(c_t) \quad (2.15)$$

Where $*$ is the Hadamard product, f_t is the forget gate; i_t is the input gate; o_t is the output gate; c_t is the cell state and \mathbf{h}_{t-1} is the previous state. W_f , W_i , W_c and W_o are the weight matrices of the forget gate; input gate; current memory state respectively and the output gate; U_f , U_i , U_c and U_o are the hidden weight matrices of the forget gate, input gate; current memory state respectively and output gate; b_f , b_i , b_c and b_o are the bias of the forget gate, input gate; current memory state respectively and output gate. Figure 2.7 shows the LSTM's cell structure.

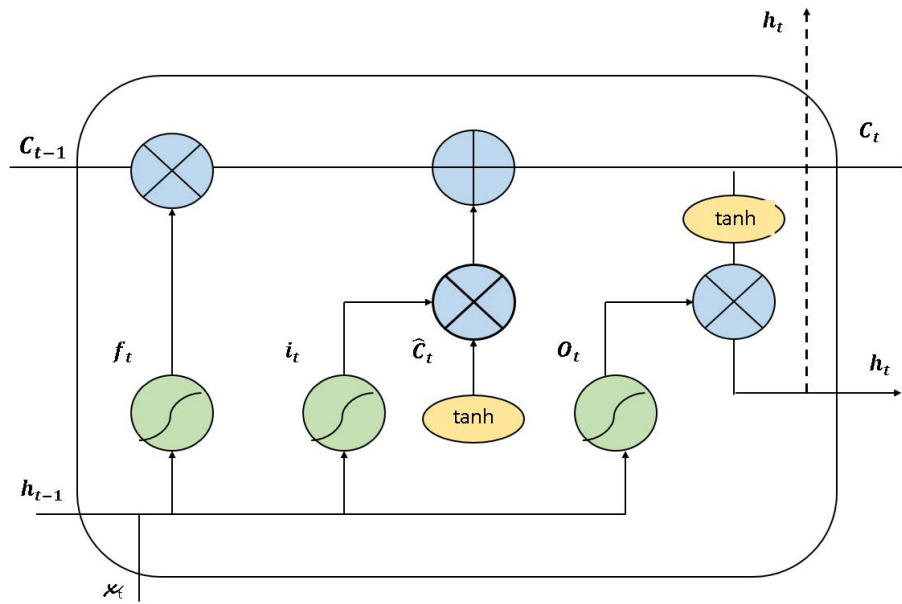


Figure 2.7. Cell structure of the LSTM

2.3.3.4. GRU – Gated Recurrent Unit Neural Network

The GRU which was introduced by Cho et al. in (Cho et al. 2014) addresses the vanishing gradient problem of the RNN giving it the opportunity to learn long term dependencies. The cellular operation is characterised by the combination of the input

gate and the update gate into a single “update gate”. The hidden state and the cell state are also merged to provide a more computationally efficient model compared to the LSTM. The update and reset gate in the GRU operate to solve the vanishing gradient problem by deciding what information should be passed to the output thus removing information which is not relevant to the prediction.

The update gate functions to determine the amount of the previous information to be passed along to the future while the reset gates controls how much of the previous information on the vehicle’s dynamics to forget. A memory content is introduced to store relevant information from the past using the reset gate. The operation of the gates of the GRU are governed by Equations (2.16-2.19).

$$\text{update gate: } \mathbf{z}_t = \sigma_f(\mathbf{W}_z \mathbf{x}_t + \mathbf{U}_z \mathbf{h}_{t-1}) + \mathbf{b}_z \quad (2.16)$$

$$\text{reset gate: } \mathbf{r}_t = \sigma_f(\mathbf{W}_r \mathbf{x}_t + \mathbf{U}_r \mathbf{h}_{t-1}) + \mathbf{b}_r \quad (2.17)$$

$$\text{current memory state: } \hat{\mathbf{h}}_t = \tanh(\mathbf{W}_h \mathbf{x}_t + \mathbf{r}_t * \mathbf{U}_h \mathbf{h}_{t-1}) + \mathbf{b}_h \quad (2.18)$$

$$\text{final memory: } \mathbf{h}_t = \mathbf{z}_t * \mathbf{h}_{t-1} + (1 - \mathbf{z}_t) \hat{\mathbf{h}}_t \quad (2.19)$$

Where $*$ is the Hadamard product; \mathbf{W}_z , \mathbf{W}_r , and \mathbf{W}_h are the weight matrices of the update gate, reset gate and current memory state respectively; \mathbf{U}_z , \mathbf{U}_r and \mathbf{U}_h are the hidden weight matrices of the update gate, reset gate and current memory state respectively; \mathbf{b}_z , \mathbf{b}_r and \mathbf{b}_h are the bias of the update gate, reset gate and current memory state respectively. Figure 2.8 shows the GRU’s cell structure.

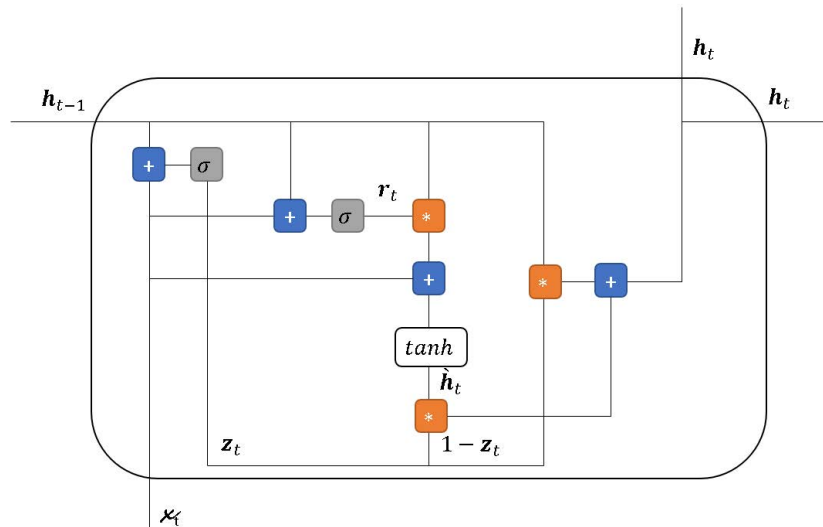


Figure 2.8 Cell Structure of the GRU

2.3.3.5. IDNN – Input Delay Neural Network

The position errors of INS are cumulative and follow a certain pattern (C. Chen et al. 2018). Therefore, previous positional sequences are required for the model to capture the error trend. It is however difficult to utilise a static neural network to model this pattern. A dynamic model can be employed by using an architecture that presents the previous “ t ” values of the signal as inputs to the network thus capturing the error trend present in the previous t timesteps (Noureldin et al. 2011). The model can also be trained to learn time-varying or sequential trends through the introduction of a memory and associator units to the input layer. The memory unit of the dynamic model can store previous INS samples and forecast using the associator unit. The use of such a dynamic model has a significant influence on the accuracy of the INS position prediction in the absence of GPS (Noureldin et al. 2011). Figure 2.9 illustrates an IDNN’s general architecture with p being the tapped delay line memory length, U_i the neurons, W the weights, G the activation function, y_t the target vector and D the delay operator.

This item has been removed due to 3rd Party Copyright. The unabridged version of the thesis can be found in the Lanchester Library, Coventry University.

Figure 2.9 Illustration of an IDNN’s general architecture (Noureldin et al., 2011)

2.4. Summary

In this chapter, we provided an overview of the GNSS; types and errors associated with their use. We also justified the use of Inertial sensors such as accelerometers, wheel encoders and gyroscopes. Their composition, theory of operation, associated errors and limitations, and coordinate frames employed during navigation are also discussed. Furthermore, the limitations to the use of the Kalman filter are highlighted following which the recent advances in the use of machine learning with respect to vehicle positioning and existing learning-based localisation methods were explored. We finally discuss the machine learning techniques used in this thesis .

In the next chapter, datasets characterised by the information gotten from the GNSS and inertial sensors are described. Using the machine learning approaches described in this chapter, several deep learning models for vehicular localisation are also proposed and described.

Chapter 3

Dataset and Methodology for Inertial and Odometry Vehicular Localisation

The previous chapter provided, an overview of common vehicular road-positioning techniques and coordinate systems. The chapter discussed recent advances in the use of machine learning techniques for positioning and justified its use over the Kalman filter. The chapter also described the machine learning techniques used in this thesis. These machine learning techniques are used to design the deep learning models described in the present chapter for position and orientation rate estimation.

This chapter introduces the datasets and experiments used to investigate the vehicular localisation techniques. This work proposes for the first time a labelled inertial odometry dataset with several complex scenarios using a multitude of sensors. The two experiments investigated in this thesis; navigation in challenging scenarios and navigation in longer-term GNSS outages are introduced along with the training datasets and evaluation datasets. We also define the metrics used in evaluating the performance of the localisation models trained. Finally, in this chapter, we define the mathematical approach (physics model) used in obtaining baselines for performance comparison as well as techniques used to determine the ground truth measurement for the position estimation models and orientation rate estimation models.

3.1 Datasets

Several public datasets dedicated to navigation and localisation on specific platforms and environments have been proposed as shown in detail (with references)

in Table A3-1 in the appendix. Such platforms include commercial Vehicles (Veh), Mobile robot (Mob), Unmanned Aerial Vehicles (UAV), Autonomous Underwater Vehicles (AUV), Unmanned Surface Vehicles (USV) and Hand-held devices (Hand) and environments as detailed in Table 3.1. Nevertheless, in this thesis, the focus is on the navigation of autonomous vehicles (commercial vehicles) in urban environment. We thus provide a summarisation of all datasets created for this purpose in Table 3.2. However, these datasets are not usually adopted for inertial and/or wheel odometry localisation in GNSS deprived environments by researchers as reviewed in Section 2.3.2. The datasets are all vision-based odometry datasets and are either characterised by simple driving scenarios, have a very high signal to noise ratio, are too small for robust evaluation, are lacking in information from other relevant sensors or are not labelled for specific investigations into the performance of positioning techniques. The proposed Inertial and Odometry Vehicle Navigation Benchmark Dataset (IO-VNBD) addresses this gap as can be shown in Table 3.2. The IO-VNBD is the largest of all the datasets compared. It is made up of 5700 km of odometry data and information from at least 27 sensors.

Table 3.1. Dataset collection platforms

Environment	Description
Urban	Town, City, Campus and infrastructures
Indoor	Indoor Environment
Underwater	Cave, Underwater floor
Terrain	Underground, farm, rough terrain and lake

Table 3.2. Several datasets for vehicular localisation

		Sensor Information						
Shortname	Complex Scenarios	Pose	IMU	GPS	Labels	Lidar	Camera	Other
IO-VNBD (Ours)	O	O	O	O	O			Wheel Encoder, Smartphone, Temperature sensor, Steering Angle, Brake pressure, Accelerometer Pedal position, etc.
KAIST Day/Night		O	O	O	O	O	O	Thermal Camera
Complex Urban		O	O	O		O		Encoder
Multi Vech Event		O	O	O		O	O	
Cityscape		O		O	O		O	
Oxford-robotcar		O	O	O		O	O	
MPO-Japan			O	O		O	O	FARO 3D

CCSAD	O	O				O		
MRPT-Malaga	O	O			O	O		
KITTI	O	O	O	O	O	O		
SeqSLAM				O		O		
Ford Campus	O	O	O			O	O	
San Francisco	O	O	O	O	O	O	O	DMI
Annotated Laser	O			O	O	O		
MIT-DARPA-Urban	O	O	O	O	O	O		
St Lucia Stereo		O	O				O	
St Lucia Multiple			O				O	
CUPAC	O	O	O	O	O	O	O	Wheel Encoder, Smartphone, Temperature sensor, Steering Angle, Brake pressure, Accelerometer Pedal position, etc.
FABMAP			O				O	

3.1.1. Inertial and Odometry Vehicle Navigation Benchmark Dataset (IO-VNBD)

This subsection introduces the Inertial and Odometry Vehicle Benchmark Dataset (IO-VNBD), a collection of data on the motion dynamics of several four wheeled vehicles for training and evaluation techniques for vehicular localisation. We argue that despite the numerous methods proposed as well as studies on vehicular positioning, each research team has employed the use of several datasets not made available to the public. This has created a challenge for the advancement in the research, comparison and adoption of machine learning based techniques for vehicular positioning in GNSS-deprived environments. In order to facilitate the benchmarking, fast development and evaluation of positioning techniques, we proposed the first of its kind complex, large-scale and information-rich inertial and odometry-focused public dataset called IO-VNBD. The vehicle tracking dataset was recorded using a research vehicle equipped with ego-motion sensors on public roads in the United Kingdom, Nigeria, and France. These sensors include a GPS receiver, inertial navigation sensors, wheel-speed sensors amongst other sensors found on the car as well as the inertial navigation sensors and GPS receiver in an Android smartphone sampling at 10Hz. The dataset consists of a total driving time of about 40 hours over 1,300km for the vehicle-extracted data and about 58 hours over 4,400 km for the smartphone recorded data. A diverse number of driving

scenarios such as traffic congestion, roundabouts, hard-braking, etc. were captured on different road types (e.g., country roads, motorways etc.) and with varying driving patterns. These complex scenarios are the drivers for this research and the data collection.

3.1.1.1. IO-VNBD Experiment Equipment

The equipment used in the collection of IO-VNBD are detailed below.

- Racelogic VBOX Video HD2 CAN – Bus Data Logger (10Hz) (VBOX Video HD2 2019)
- Racelogic VBOX Video HD2 GPS Antenna (10Hz)(VBOX Video HD2 2019)
- Smartphones (Huawei P20 pro, Motorola moto G7 power and Blackberry Priv) using AndroSensor Application (10Hz) (AndroSensor 2019).

The Racelogic VBOX data logger was used to log data from the ECU of the vehicle and the Racelogic GPS antenna for the vehicle extracted data. For the smartphone extracted data, the Androsensor application was used to log the data from the sensors already present within the phone.

3.1.1.2. IO-VNBD Experiment Setup

a) IO-VNBD Vehicle Experiment Setup

The vehicle used for the data collection exercise was a front-wheel drive Ford Fiesta Titanium as shown in Figure 3.1. The Racelogic VBOX Video HD2 was used to record the data from the vehicle CAN bus as well as the corresponding GPS coordinates at each sampling instance. As shown in Figures 3.1 and 3.2, the GPS antenna was placed centrally at the top of the vehicle to ensure optimal signal reception. The Racelogic VBOX Video HD2 CAN – Bus data logger (10Hz) was used to record the data shown in Table 3.5 directly from the CAN bus of the vehicle with a sampling and update frequency of 10Hz.

This item has been removed due to 3rd Party Copyright. The unabridged version of the thesis can be found in the Lanchester Library, Coventry University.



Figure 3.2 Smartphone and GPS antennae setup

b) IO-VNBD Smartphone Experiment Setup

A Ford Fiesta Titanium, Volvo XC70, Renault Mégane and Toyota Corolla Verso were used to collect the smartphone datasets. The smartphone was held with a phone holder attached to the vehicle as shown in Figure 3.2. Using the Androsensor app, the data was sampled every 0.1s with a GPS (smartphone) update rate of 1Hz. Figure 3.1 shows the axis alignment of the smartphone sensors. The smartphone sensors employed were a 3-axis accelerometer, a 3-axis gyroscope, a 3-axis magnetometer and heading, as well as the GPS latitude and longitude coordinates all present within the phone. Other information such as the vehicle's velocity and acceleration were recorded from the smartphone's GPS. Table 3.7 highlights the data recorded from the smartphone. The datasets described in Tables A2-1 to A7 in the appendix were collected using the Huawei P20 pro smartphone.

3.1.1.3. IO-VNBD Data Description

The total dataset consists of about 100 hours of recorded driving data on public roads by 8 different drivers with different driving styles as defined in Table 3.3, where defensive driving refers to situations where the vehicle is turned at less than 0.3g, swerved at less than 3.3 km/hr or decelerated at less than 0.3g, whilst aggressive driving refers to respective situations above these thresholds (U.S. Department of Transportation 2009). The data is divided into sets based on cities and towns driven via, road conditions, weather conditions, driving length and time, driving style and driving features (see Tables A2-1 to A8 in the appendix). The dataset also contains more than 20 minutes of data recorded from the stationary vehicle to aid the estimation of the sensors' bias. To add to the diversity of the data consisting of a number of complex driving scenarios as shown on Table 3.6, the data was recorded with different tyre pressures. Datasets with each unique tyre pressures are indicated in Tables A2-1 to A8 in the appendix using Table 3.4 as a guide. Tables A2-1 to A8 in the appendix reveal more detailed information on each

set of the data. The data logged from the vehicle's CAN bus are denoted with the prefix "V-" and the smartphone data denoted with the prefix "S-". The "S-" datasets are acquired from the sensors in a smartphone attached to the vehicle mimicking its motion*. While all the "V-" datasets were collected uniquely in England, the "S-" datasets were collected in England, France and Nigeria.

Table 3.3. Driving pattern of each driver

Driver	Driving Style
A	Aggressive and Defensive
B	Aggressive
C	Aggressive and Defensive
D	Aggressive and Defensive
E	Aggressive and Defensive
F	Defensive
G	Defensive
H	Defensive

Over the course of the data collection, communication difficulties between the GPS receiver and satellites were encountered. Information on data indexes recorded during these periods were provided in a file titled "GPS outages". Where possible, the "S-" and "V-" datasets which were collected simultaneously¹, were manually synchronised and stored in the folder named "Synchronised V and S datasets".

Importantly, despite the effort lent towards an accurate alignment of the smartphone's sensor axis with that of the vehicle, the precision of the measurements were interfered by vehicular vibrations averagely estimated to be about 0.15 g of acceleration and 0.08 rad/s of yaw rate particularly in peculiar scenarios such as hard brakes or over bumps. Information on the amount of gravitational acceleration measured by each of the three axes are provided in the "S-" datasets to help in the correction of the measured acceleration. The data is stored in csv format in <https://github.com/onyekpeu/IO-VNBD>.

* It is difficult to truly determine the centre of gravity of the car under different dynamic conditions, hence the smartphone recording approximates the true motion of the car.

¹ Not all "V-" and "S-" dataset were collected simultaneously. All the "V-" datasets without a corresponding "S-" dataset and vice-versa are not placed in the "Synchronised V and S datasets" folder.

Table 3.4. Various tyre pressures experimented on

Notation	Tyre Pressure (psi)
A	Front right - 16
	Front left - 15
	Rear right - 14
	Rear left - 14
B	Front right - 31
	Front left - 31
	Rear right - 25
	Rear left - 25
C	Front right - 33
	Front left - 33
	Rear right - 31
	Rear left - 27
D	Front right - 33
	Front left - 33
	Rear right - 26
	Rear left - 26
E	Front right – N/A
	Front left - N/A
	Rear right – N/A
	Rear left – N/A

Table 3.5. Information recorded from the Ford Fiesta's ECU

No	Column Heading	Unit
1	No of GPS satellites available	N/A
2	Time since start of day	seconds
3	Latitude	degrees
4	Longitude	degrees
5	Velocity	km/hr
6	Heading	degrees
7	Height	km
8	Vertical velocity	km/hr
9	Sampleperiod	seconds
10	Steering angle	degrees
11	Wheel speed front left	rad/sec
12	Wheel speed front right	rad/sec
13	Wheel speed rear left	rad/sec
14	Wheel speed rear right	rad/sec
15	Yaw rate	deg/sec
16	Indicated vehicle speed	km/hr
17	Indicated longitudinal acceleration	g
18	Indicated lateral acceleration	g
19	Handbrake	activated or not (0 or 1)
20	Gear requested	number of gear employed (1-5)
21	Gear	number of gear employed (1-5)
22	Engine speed	rev/min
23	Coolant temperature	degree celcius
24	Clutch position	activated or not (0 or 1)

Table 3.6. Environmental and driving scenarios investigated.

No	Scenarios
1	Hard brake
2	Sharp turn left and right
3	Swift maneuvers
4	Roundabout
5	Rain
6	Night and day
7	Skid
8	Mountain/hills
9	Dirt roads/ Gravel Roads
10	Country roads
11	Motorway
12	Town-centre driving
13	Traffic congestion
14	Successive left and right turns
15	Varying accelerations within a short duration
16	A -roads
17	B- roads
18	Wet roads
19	U-turns / Reverse drives
20	Mud road
21	Varying tyre pressure
22	Drifts
23	Bumps
24	Inner city driving
25	Winding roads
26	Zig-Zag drives
27	Approximate straight-line motion
28	Parking
29	Potholes
30	Residential roads
31	Stationary (No Motion)
32	Valleys

Table 3.7. Information recorded from the smartphone sensors.

No	Column Heading	Unit
1	GPS latitude	degrees
2	GPS longitude	degrees
3	GPS altitude	m
4	GPS speed	km/hr
5	GPS accuracy	m
6	GPS orientation	degrees
7	GPS satellites In range	N/A
8	Time since start	ms
9	Date	YYYY-MO-DD HH-MI-SS_SSS
10	Accelerometer X	m/s ²
11	Accelerometer Y	m/s ²
12	Accelerometer Z	m/s ²
13	Gravity X	m/s ²
14	Gravity Y	m/s ²
15	Gravity Z	m/s ²
16	Gyroscope (Yaw)	rad/s
17	Gyroscope (Pitch)	rad/s
18	Gyroscope (Roll)	rad/s
19	Magnetic field X	μT
20	Magnetic field Y	μT
21	Magnetic field Z	μT
22	Orientation (Yaw)	degrees
23	Orientation (Pitch)	degrees
24	Orientation (Roll)	degrees

3.1.2. Coventry University Public road dataset for Automated Cars (CUPAC) Dataset

The CUPAC dataset is similar to the IO-VNBD in terms of the diversity in the number of sensors used in collecting the data. However, the CUPAC dataset offers fewer number of driving scenarios needed to robustly evaluate the performance of the positioning models. The CUPAC dataset was used to validate the performance of the positioning models in Chapter 5 and 6.

This CUPAC dataset was collected on public streets in Coventry, United Kingdom under different weather, traffic and road conditions. A LIDAR unit, a GPS receiver, smartphone sensors, vehicle CAN bus data logger and monocular, infrared are used in capturing the dataset. Although the dataset is focused on vision-based navigation, the wheel speed information from the CAN bus of the vehicle as well as the vehicle's GPS positional coordinates were used in this study. The CUPAC dataset was also collected using a Ford Fiesta at a sample rate of 10Hz. More details of the CUPAC dataset can be found in (Weber and Kanarachos 2020).

3.2 Methodology

In this section, the methodologies used in this thesis are described. This section describes the ground truth formulations used to train the deep learning models. The physics models used as baselines to compare the performance of the deep learning models are also described alongside the deep learning model training parameters.

3.2.1 Ground Truth Formulation – Positioning and Orientation Rate Formulation Using GNSS

The formulation of the ground truths used as the targets for the training of the machine learning models and also for the comparison of the performance of both the physics and machine learning models are described. The positional ground truth and orientation rate ground truth are discussed.

3.2.1.1 Transformation (Rotation) Matrix

Tracking the position of a vehicle is usually done relative to a point of reference. The INS's measurements, usually provided in the body (sensors) frame, would need to be transformed into the navigation frame for tracking purposes (Kok, Hol, and Schön 2017). In this thesis, we adopt the North-East-Down (NED) convention in defining the

navigation frame. The transformation matrix R^{nb} from the body frame to navigation frame for a vehicle is as shown in Equation. (3.1 and 3.2).

$$R^{nb} = \begin{bmatrix} \cos\Psi & -\sin\Psi & 0 \\ \sin\Psi & \cos\Psi & 0 \\ 0 & 0 & 1 \end{bmatrix} \begin{bmatrix} \cos\theta & 0 & \sin\theta \\ 0 & 1 & 0 \\ -\sin\theta & 0 & \cos\theta \end{bmatrix} \begin{bmatrix} 1 & 0 & 0 \\ 0 & \cos\phi & -\sin\phi \\ 0 & \sin\phi & \cos\phi \end{bmatrix} \quad (3.1)$$

$$R^{nb} = \begin{bmatrix} \cos\theta\cos\Psi & -\cos\theta\sin\Psi + \sin\phi\sin\theta\cos\Psi & \sin\phi\sin\Psi + \cos\phi\sin\theta\cos\Psi \\ \cos\theta\sin\Psi & \cos\phi\cos\Psi + \sin\phi\sin\theta\sin\Psi & -\sin\phi\cos\Psi + \cos\phi\sin\theta\sin\Psi \\ -\sin\theta & \sin\phi\cos\theta & \cos\phi\cos\theta \end{bmatrix} \quad (3.2)$$

Where ϕ is the roll, θ is the pitch and Ψ is the yaw. However, as our study is limited to the two-dimensional tracking of vehicles, ϕ and θ are thus considered to be zero, thus the rotation matrix R^{nb} becomes:

$$R^{nb} = \begin{bmatrix} \cos\Psi & -\sin\Psi & 0 \\ \sin\Psi & \cos\Psi & 0 \\ 0 & 0 & 1 \end{bmatrix} \quad (3.3)$$

3.2.1.1 Orientation Rate Estimation

The orientation angles or attitude of the vehicle are used to populate the rotation matrix as shown in Equation (3.3). The populated rotation matrix is in turn used to transform the position of the vehicle from the body frame to the navigation frame as shown later in Equation (3.36 - 3.38). However, as expressed in the previous section, we make use of yaw angle to populate the reduced rotational matrix in Equation (3.3). The yaw angle (heading) information is obtained from the GNSS signal and processed as shown in Equation (3.4) to get the yaw rate (ground truth for the machine learning orientation rate estimation model training). We selected the yaw rate instead of the yaw angle as we observed from experimentation, that the machine learning models produce better estimates when trained to learn the yaw rates.

$$\omega_{GNSS,t}^b = \psi_{GNSS,t} - \psi_{GNSS,t-1} \quad (3.4)$$

3.2.1.2 Position Estimation (Vehicles true displacement estimation x_{GNSS}^b)

The trajectory of the vehicle lies on the surface of the earth. To determine the position of the vehicle, the displacement of the vehicle needs to be traced along the surface of the earth. However, the shape of the earth is neither a perfect sphere nor ellipse but rather an oblate ellipsoid. Due to the unique shape of the earth, complications exist as there is no geometric shape it can be categorised under for analysis. The Haversine formula

applies perfectly to the calculations of distances on spherical shapes while the Vincenty's formula applies to elliptical shapes (Mahmoud and Akkari 2016).

a) Haversine's Formula

The Haversine's formula is used to calculate the distance between two points on the earth's surface specified in longitude and latitude. It assumes a spherical earth (Thomas and Featherstone 2005).

$$\hat{x}_{GPS}^b = 2r \sin^{-1} \left(\sqrt{\sin^2 \left(\frac{\phi_t - \phi_{t-1}}{2} \right) + \cos(\phi_{t-1}) \cos(\phi_t) \sin^2 \left(\frac{\varphi_t - \varphi_{t-1}}{2} \right)} \right) \quad (3.5)$$

Where \hat{x}_t^b is the distance travelled within $t - 1, t$ with longitude and latitude (φ, ϕ) as obtained from the GPS and r is the radius of the earth.

b) Vincenty's Inverse Formula

The Vincenty's formula is used to calculate the distance between two points on the earth's surface specified in longitude and latitude. It assumes an ellipsoidal earth (Vincenty 1975). It calculates the distance between two points as well as its azimuth as shown in *Equations* (3.6 – 3.24).

$$\text{Given: } f = \frac{1}{298.257223563} \quad (3.6)$$

$$b = (1 - f)a \quad (3.7)$$

$$U_1 = \arctan((1 - f) \tan \phi_1) \quad (3.8)$$

$$\varphi = \phi_2 - \phi_1 \quad (3.9)$$

$$U_1 = \arctan((1 - f) \tan \phi_2) \quad (3.10)$$

$$\sin \sigma' = \sqrt{(\cos U_2 \sin \lambda)^2 + (\cos U_1 \sin U_2 - \sin U_1 \cos U_2 \cos \lambda)^2} \quad (3.11)$$

$$\cos \sigma' = \sin U_1 \sin U_2 + \cos U_1 \cos U_2 \cos \lambda \quad (3.12)$$

$$\sigma = \arctan2(\sin \sigma', \cos \sigma') \quad (3.13)$$

$$\sin \alpha = \frac{\cos U_1 \cos U_2 \sin \lambda}{\sin \sigma} \quad (3.14)$$

$$\cos(2\sigma'_m) = \cos \sigma' - \frac{2 \sin U_1 \sin U_2}{\cos^2 \alpha} \quad (3.15)$$

$$C = \frac{f}{16} \cos^2 \alpha [4 + f(4 - 3 \cos^2 \alpha)] \quad (3.16)$$

$$\lambda = \varphi + (1 - C)f \sin \alpha [\sigma' + C \sin \sigma [\cos(2\sigma'_m) + C \cos \sigma'(-1 + 2 \cos^2(2\sigma'_m))]] \quad (3.17)$$

$$u^2 = \cos^2 \alpha \left(\frac{a^2 - b^2}{b^2} \right) \quad (3.18)$$

$$k_1 = \frac{\sqrt{1 + u^2} - 1}{\sqrt{1 + u^2} + 1} \quad (3.19)$$

$$A = \frac{1 + \frac{1}{4}k_1^2}{1 - k_1} \quad (3.20)$$

$$B = k_1 \left(1 - \frac{3}{8}k_1^2\right) \quad (3.21)$$

$$\Delta\sigma' = B \sin \sigma' \left\{ \cos^2(2\sigma'_m) \right. \quad (3.22)$$

$$\left. + \frac{1}{4}B \left(\cos \sigma' [-1 + 2 \cos^2(2\sigma'_m)] - \frac{B}{6} \cos[2\sigma'_m] [-3 + 4 \sin^2 \sigma'] [-3 + 4 \cos^2(2\sigma'_m)] \right) \right\}$$

$$\alpha_1 = \arctan2(\cos U_2 \sin \lambda, \cos U_1 \sin U_2 - \sin U_1 \cos U_2 \cos \lambda) \quad (3.23)$$

$$\alpha_2 = \arctan2(\cos U_1 \sin \lambda, \sin U_1 \cos U_2 - \cos U_1 \sin U_2 \cos \lambda) \quad (3.24)$$

Where \hat{x}_t^b is the distance travelled within $t - 1$ and t with longitude and latitude (φ, \emptyset) , where a is the radius of the earth at the equator, f is the flattening at the ellipsoid, b is the length of the ellipsoid semi-minor axis, U_1 and U_2 is the reduced latitude at t and $t - 1$ respectively, λ is the change in longitude along the auxiliary spheres is the ellipsoidal distance between the position at $t - 1$ and t , σ'_1 angle between the position at $t - 1$ and t , σ angle between the position at $t - 1$ and t , and σ'_m is the angle between the equator and midpoint of the line.

The Vincenty's formula is used in this thesis as it provides a more accurate solution compared to Haversine and other great circle formulas (Mahmoud and Akkari 2016). The python implementation of Vincenty's Inverse Formula is used (Pietrzak 2016).

3.2.2 Physics Model And Machine Learning Schemes For Vehicular Position And Orientation Estimation

The physics models and machine learning models used in this thesis for the localisation of autonomous vehicles problem are discussed in this section.

3.2.2.1 Physics Model

Three physics models are considered, one for the accelerometer-based position estimation, another for orientation rate estimation using the gyroscope and the last for position estimation using the wheel encoder.

a) Accelerometer-based Position Estimation Physics Model (APM)

The accelerometer measures the specific force², f^b on the sensor in the body frame and is as expressed in Equation (3.25); where g^n represents gravity, R^{bn} is the rotation matrix from the navigation frame to the body frame and a^n denotes the linear acceleration of the sensor expressed in the navigation frame.

However, the accelerometer measurements at each time t are usually corrupted by a bias δ_{INS}^b and noise ε_a^b , and are thus represented by F_{INS}^b , as shown in Equation (3.26).

$$f^b = R^{bn}(a^n - g^n) \quad (3.25)$$

$$F_{INS}^b = f_{INS}^b + \delta_{INS}^b + \varepsilon_a^b \quad (3.26)$$

More so, the accelerometer's bias varies slowly with time and as such can be modelled as a constant parameter; whilst the accelerometer's noise is somewhat characterised by a Gaussian distribution and modelled as $\varepsilon_a^b \sim N(0, \Sigma_a)$. Therefore, the specific measurement equation as expressed in Equation (3.25) can be expanded as shown below, where a^b is the linear acceleration in the body frame and g^b is the acceleration due to gravity in the body frame.

$$\text{from Equation (3.25), } a^b = f^b + g^b, \quad (3.27)$$

$$\text{from Equation (3.26), } F_{INS}^b = a_{INS}^b + \delta_{INS,a}^b + \varepsilon_a^b \quad (3.28)$$

$$a^b = F_{INS}^b - \delta_{INS,a}^b - \varepsilon_a^b \quad (3.29)$$

$$a^b + \varepsilon_a^b = F_{INS}^b - \delta_{INS,a}^b \quad (3.30)$$

$$\text{However, } a_{INS}^b = F_{INS}^b - \delta_{INS,a}^b \quad (3.31)$$

$$a_{INS}^b = a^b + \varepsilon_a^b \quad (3.32)$$

Where a_{INS}^b is the bias and gravity compensated acceleration measurement. The vehicle's velocity in the body frame can be estimated through the integration of Equation (3.32) as shown below:

$$v_{INS}^b = \int_{t-1}^t a^b + \varepsilon_v^b \quad (3.33)$$

² In the vehicle tracking application, the centrifugal acceleration is considered absorbed in the local gravity sector and the centrifugal acceleration considered negligible due to its small magnitude

Through the double integration of Equation (3.32), the displacement of the vehicle in the body frame at time t from $t - 1$, x_{INS}^b , can also be determined as shown in Equation (3.34).

$$x_{INS}^b = \iint_{t-1}^t a^b + \varepsilon_x^b \quad (3.34)$$

Where ε_x^b and ε_v^b are the noise characterising the INS's displacement and velocity information formulation derived from ε_a^b , $\delta_{INS,a}^b$ is the sensor's bias in the body frame calculated as a constant parameter from the average reading of a stationary accelerometer ran for 20 min, F_{INS}^b is the corrupted measurement of the accelerometer sensor at time t (sampling time), g is the acceleration due to gravity and $\iint_{t-1}^t a^b$, $\int_{t-1}^t a^b$ and a^b are the uncorrupted (true) displacement, velocity and acceleration, respectively, of the vehicle.

Thus, the vehicle's true displacement is expressed as $x_{GNSS}^b \approx \iint_{t-1}^t a^b$.

Furthermore, ε_x^b can be obtained by:

$$\varepsilon_x^b \approx x_{GNSS}^b - x_{INS}^b \quad (3.35)$$

Using the North-East-Down (NED) system, the noise ε_x^b , displacement x_{INS}^b , velocity v_{INS}^b and acceleration a_{INS}^b of the vehicle in the body frame within the window $t - 1$ to t can be transformed into the navigation frame using R^{nb} as shown in Equations 3.36–3.40. However, the down axis is not considered in this study. More so, the window size in this study is defined as 1 s.

$$R_{INS}^{nb} \cdot a_{INS}^b \rightarrow a_{INS}^n \rightarrow a_{INS}^b \cdot \cos\Psi, a_{INS}^b \cdot \sin\Psi, \quad (3.36)$$

$$R_{INS}^{nb} \cdot v_{INS}^b \rightarrow v_{INS}^n \rightarrow v_{INS}^b \cdot \cos\Psi_{INS}, v_{INS}^b \cdot \sin\Psi, \quad (3.37)$$

$$R_{INS}^{nb} \cdot x_{INS}^b \rightarrow x_{INS}^n \rightarrow x_{INS}^b \cdot \cos\Psi, x_{INS}^b \cdot \sin\Psi, \quad (3.38)$$

$$\text{Where: } R_{INS}^{nb} = \begin{bmatrix} \cos\Psi_{INS} & -\sin\Psi_{INS} & 0 \\ \sin\Psi_{INS} & \cos\Psi_{INS} & 0 \\ 0 & 0 & 1 \end{bmatrix}, \quad (3.39)$$

$$\begin{bmatrix} a_{INS}^{n,North} \\ a_{INS}^{n,North} \\ v_{INS}^{n,North} \\ v_{INS}^{n,North} \\ x_{INS}^{n,North} \\ x_{INS}^{n,East} \end{bmatrix} = \begin{bmatrix} a_{INS}^b \cdot \cos\Psi_{INS} \\ a_{INS}^b \cdot \sin\Psi_{INS} \\ v_{INS}^b \cdot \cos\Psi_{INS} \\ v_{INS}^b \cdot \sin\Psi_{INS} \\ x_{INS}^b \cdot \cos\Psi_{INS} \\ x_{INS}^b \cdot \sin\Psi_{INS} \end{bmatrix}. \quad (3.40)$$

b) Gyroscope-based orientation rate estimation Physics Model (GPM)

The gyroscope measures the rate of change of attitude (angular velocity) in yaw, roll and pitch with respect to the inertial frame as expressed in the body frame (Kok, Hol, and Schön 2017). Giving initial orientation information Ψ_0 , the attitude rate from the gyroscope ω_{INS}^b can be integrated to provide continuous orientation Ψ_{INS} information in the absence of the GNSS signal.

$$\Psi_{INS} = \Psi_0 + \int_{t-1}^t \omega_{INS}^b \quad (3.41)$$

c) Wheel encoder-based position estimation Physics Model (WPM)

The angular velocity of the wheels at a given time (t) is measured by the wheel speed sensors. But there can be uncertainties in the tyre's diameter due to the condition of the tyre (such as tyre wearing), tyre pressure, and wheel slip. These uncertainties affect the accuracy of displacement estimation from the wheel speed measurement ω . Equations (3.42) - (3.45) consider the errors which can affect the vehicle speed calculations.

$$\hat{\omega}_{whrl}^b = \omega_{whrl}^b + \varepsilon_{whrl}^b \quad (3.42)$$

$$\hat{\omega}_{whrr}^b = \omega_{whrr}^b + \varepsilon_{whrr}^b \quad (3.43)$$

$$\hat{\omega}_{whfl}^b = \omega_{whfl}^b + \varepsilon_{whfl}^b \quad (3.44)$$

$$\hat{\omega}_{whfr}^b = \omega_{whfr}^b + \varepsilon_{whfr}^b \quad (3.45)$$

Where $\hat{\omega}_{whrl}^b$, $\hat{\omega}_{whrr}^b$, $\hat{\omega}_{whfl}^b$ and $\hat{\omega}_{whfr}^b$ are the noisy wheel speed measurements of the rear left, rear right, front left and front right wheels, whereas ε_{whrl}^b , ε_{whrr}^b , ε_{whfl}^b and ε_{whfr}^b are the corresponding errors (uncertainties), and ω_{whrl}^b , ω_{whrr}^b , ω_{whfl}^b and ω_{whfr}^b are the respective error-free wheel speed measurements.

Equations (3.46) and (3.47) show the calculation of the angular velocity (wheel speed) of the rear axle.

$$\hat{\omega}_{whr}^b = \frac{\omega_{whrr}^b + \omega_{whrl}^b}{2} + \frac{\varepsilon_{whrr}^b + \varepsilon_{whrl}^b}{2} \quad (3.46)$$

expressing $\frac{\varepsilon_{whrr}^b + \varepsilon_{whrl}^b}{2}$ as ε_{whr}^b and $\frac{\omega_{whrr}^b + \omega_{whrl}^b}{2}$ as ω_{whr}^b

$$\hat{\omega}_{whr}^b = \omega_{whr}^b + \varepsilon_{whr}^b \quad (3.47)$$

From $v = \omega r$, the linear velocity of the vehicle in the body frame can be found, with r as a constant which maps the wheel speed of the rear axle to the linear velocity of the vehicle:

$$v_{wh}^b = \omega_{whr}^b r + \varepsilon_{whr}^b r \quad (3.48)$$

Take $\varepsilon_{whr}^b r$ as $\varepsilon_{whr,v}^b$

$$v_{whr}^b = \omega_{whr}^b r + \varepsilon_{whr,v}^b \quad (3.49)$$

The displacement of the vehicle in the body frame can be found through the integration of the vehicle's velocity from *Equation (3.49)* and incrementally updated for continuous tracking. $\varepsilon_{whr,x}^b$ in *Equation (3.50)* is the integral of $\varepsilon_{whr,v}^b$ from *Equation (3.49)*.

$$x_{whr}^b = \int_{t-1}^t (\omega_{whr}^b r) + \varepsilon_{whr,x}^b \quad (3.50)$$

The uncertainty in the position estimation can be found through *Equation (3.51)* during the presence of the GNSS signal. The task thus becomes that of estimating $\varepsilon_{whr,x}^b$ during GNSS outages needed to correct the vehicles displacement x_{whr}^b .

$$\varepsilon_{whr,x}^b \approx x_{whr}^b - x_{GNSS}^b \quad (3.51)$$

x_{GNSS}^b is the vehicle's true displacement measured according to (Vincenty 1975) using Vincenty's formula for geodesics on an ellipsoid based on the longitudinal and latitudinal positional information of the vehicle as in (Pietrzak 2016). The accuracy of x_{GNSS}^b is however limited to the accuracy of the GNSS which is defined as $\pm 3m$ according to (VBOX Video HD2 2019).

3.2.1.2 Deep Learning - based Models.

Three machine learning models are discussed in this section. The first predicts position using the sensor data from the accelerometer as well as inputs from the previous known position of the vehicle as input into the machine learning model. The second model uses the data from the gyroscope as an input to the machine learning model with the aim of learning the noise within the gyroscope's measurement in order to predict the orientation rate of the vehicle. The last machine learning model uses the sensor data from the wheel encoder to learn the uncertainty present within the measurements of the wheel encoder needed for continuous positioning correction.

a) Accelerometer-based position estimation neural Network (AccNet)

A position estimation model called AccNet is proposed to minimise the effect of the noise in the accelerometer, as illustrated in Figure 3.3. The proposed model, which is analogous to the functioning of a closed-loop or feedback control system, operates in

prediction mode by feeding back the output of the neural network at $t - 1/t - 2$ and the vehicle's acceleration at time window $t/t - 1$ into the neural network in order to estimate the distance covered by the vehicle within the current window $t/t - 1$, as shown in Figure 3.3. NED refers to the North-East-Down coordinates defining the navigation frame.

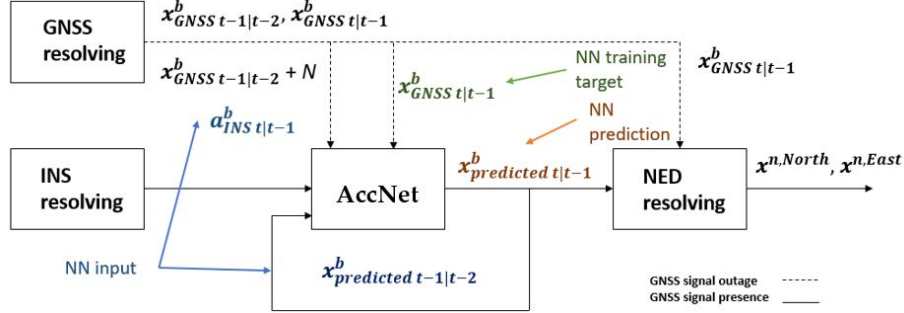


Figure 3.3. Prediction setup of the proposed AccNet displacement estimation model.

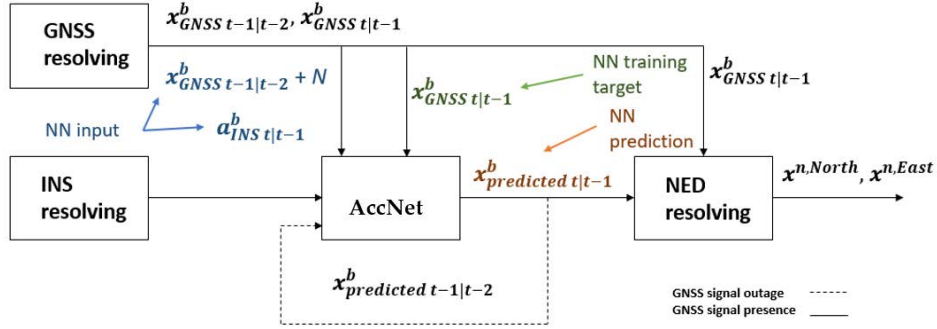


Figure 3.4. Training setup of the proposed AccNet displacement estimation model.

However, as presented in Figure 3.3, during the training phase, the Neural Network (NN) is fed with the GNSS estimated displacement rather than the output of the NN. Both models (training and prediction) are structured this way due to the availability of the GNSS signal during the training phase and its absence in the prediction phase. The NN's output is thus setup to mimic the functionality of the GNSS resolved displacement at window $t - 1/t - 2$ during the prediction operation.

Howbeit, as the NN's output never matches the GNSS displacement, the challenge becomes one of minimising the effect of the inexactness of the previous NN's estimation on the performance of the prediction model. We set about to address this by introducing a controlled random white Gaussian noise N with a normal distribution $N \sim N(\mu, \sigma^2)$ to one of the inputs of the NN: the GNSS resolved displacement within the previous time window, during the training phase. Where the mean μ , and the variance σ^2 , are determined experimentally from a sample displacement resolving of the GNSS and INS signals. This approach attempts to aid the NN to account for the impreciseness

in the prediction output. Figures 3.3 and 3.4 show the prediction and training set-up of the displacement model, respectively. Figure 3.5 shows the learning rate of the AccNet

where during training, \mathbf{x}_t refers to the information from the accelerometer at time t , and the vehicle's displacement from the GNSS resolving at time $t-1$; and \mathbf{y}_t is the vehicle's estimated displacement at time t . During the prediction step (which is methodologically implemented after the training step), \mathbf{x}_t refers to the information from the accelerometer at time t , and the vehicle's estimated displacement from AccNet at time $t-1$; and \mathbf{y}_t is the vehicle's estimated displacement at time t .

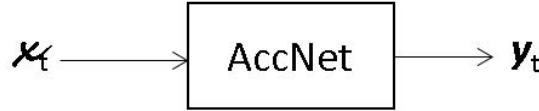


Figure 3.5. AccNet's learning scheme

b) Gyroscope-based orientation rate estimation neural Network (GyroNet)

We adopt a much simpler approach towards the estimation of the vehicle's orientation rate as we found no performance benefit in utilising the feedback approach presented in Section 3.2.1.2.a. On the orientation rate estimation, GyroNet (an Input Delay Neural Network as justified in Section 3.2.3.2) is made to learn the relationship between the yaw rate ω_{INS}^b as provided by the gyroscope and the ground truth (yaw rate) ω_{GNSS}^b calculated from the information provided by the GNSS. The GyroNets learning scheme is illustrated in Figure 3.6 and 3.7, where \mathbf{x}_t is the yaw rate ω_{INS}^b input to the model from the gyroscope at time t and \mathbf{y}_t is the error free yaw rate information of the vehicle at time t .



Figure 3.6. GyroNet's learning scheme

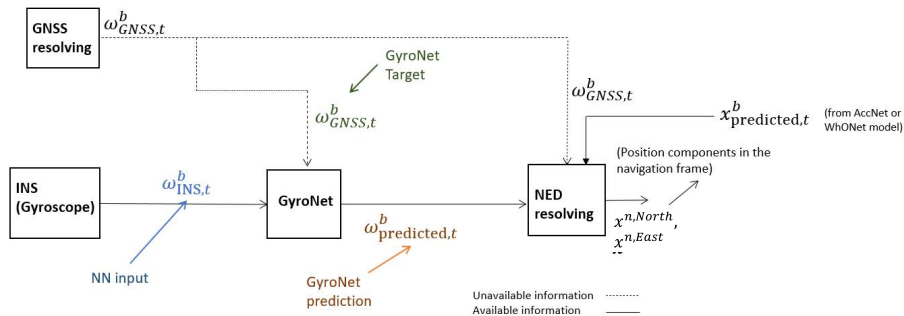


Figure 3.7. GyroNet's orientation rate prediction block during GNSS outages

c) Wheel Odometry position estimation neural Network (WhONet)

The learning scheme for the WhONet is as presented in Figure 3.8. WhONet uses a simple Recurrent Neural Network as justified in Section 3.2.3.2. For every time t , the input to the Neural Network (NN), $\mathbf{x}_{t|t-0.9}$, is made up of the wheel speed information of all four wheels of the vehicle from every tenth of a second within the previous second;

$\mathbf{x}_t, \mathbf{x}_{t-0.1}, \dots$ and $\mathbf{x}_{t-0.9}$. The NN is tasked with predicting \mathbf{y}_t , which is the error $\epsilon_{whr,x}^b$ between the wheel-speed-derived displacement x_{whr}^b and the GNSS-derived displacement x_{GNSS}^b .

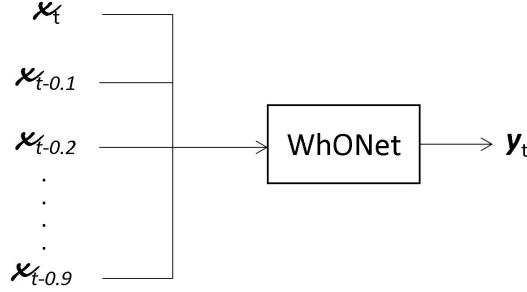


Figure 3.8. WhONet's learning scheme

The proposed prediction block for the positioning of vehicles in the absence of GNSS signals using the wheel speed information is presented in Figure 3.9.

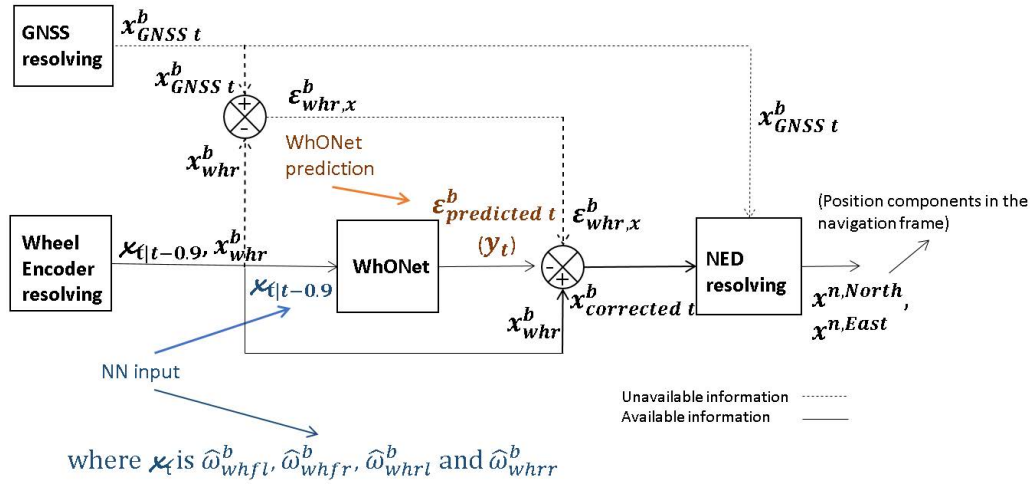


Figure 3.9. WhONet's position prediction block during GNSS outages

3.2.3 Model Selection, Training and Evaluation

This subsection describes the metrics used to evaluate the performance of both the deep learning models and physics models. Furthermore, we justify the selection of the NN algorithm for each deep learning model, and discuss the training process, datasets and parameters. Finally, we describe how both the physics models and deep learning models are evaluated and describe the two scenarios used in evaluating the performance of the models in this thesis.

3.2.3.1 Performance Evaluation Metrics

The performances of all models investigated are evaluated using the metrics defined below:

Cumulative Root Square Error (CRSE): The CRSE describes the cumulative root mean squared of the prediction error for every one second of the total duration of the GNSS outage. This method ignores the negative sign of the estimated errors thus providing a better understanding of the performance of the positioning techniques being analysed. The CRSE is defined mathematically in Equation (12).

$$CRSE = \sum_{t=1}^{N_t} \sqrt{e_{pred}^2} \quad (3.52)$$

Where N_t is GNSS outage length of 10s in the challenging scenarios and 30s, 60s, 120s and 180s in the longer-term GNSS outage scenario, t is the sampling period and e_{pred} is the prediction error.

Cumulative True Error (CTE): The CTE measures the summation of the prediction error from every one second time interval of the total GNSS outage duration. Since no root squared value is taken in this method, the positive and negative signs of the error estimations are considered in the calculation. Over estimations and under estimations of the position errors during the GNSS outage can be better understood with this metric. The CTE is less realistic in comparing the performances of positioning techniques compared to the CRSE. Equation (13) describes the CTE method.

$$CTE = \sum_{t=1}^{N_t} e_{pred} \quad (3.53)$$

Mean (μ): Mean refers to the statistical mean of the CRSE and CTE across all test sequences in each scenario investigated.

$$\mu_{CRSE} = \frac{1}{N_s} \sum_{i=1}^{N_s} CRSE, \mu_{CTE} = \frac{1}{N_s} \sum_{i=1}^{N_s} CTE \quad (3.54)$$

Where N_s is the total number of test sequences in each scenario.

Standard deviation (σ): Standard deviation provides information on the variations of the CRSE and CTE of all test sequences in each scenario investigated. The standard deviation is used in this thesis to measure the robustness of the models investigated.

$$\sigma_{CRSE} = \sqrt{\frac{\sum (CRSE_i - \mu_{CRSE})^2}{N_s}}, \sigma_{CTE} = \sqrt{\frac{\sum (CTE_i - \mu_{CTE})^2}{N_s}} \quad (3.55)$$

Minimum: This refers to the minimum of CRSE and CTE of all test sequences in each scenario investigated.

Maximum: This refers to the maximum of CRSE and CTE of all test sequences in each scenario investigated. The *max* metric holds more significance compared to the μ and *min* in the challenging driving scenarios experiment, as it captures the performance of the vehicle in each challenging scenario explored and further informs on the accuracy of the investigated techniques in each scenario.

3.2.3.2 NN Model Selection (Experiments)

The proliferation of Deep Learning and the internet of things on low memory devices, increasing sensing and computing applications and capabilities promise to transform the performance of such devices on complex sensing tasks. The key impediment to the wider adoption and deployment of neural network-based sensing application is their high computation cost. Therefore, there is the need to have a more compact parameterisation of the neural network models. To this end, we evaluate the performance of the MLP, IDNN, simple RNN (sRNN), GRU and LSTM on the roundabout scenario across different parameterisation for model efficiency.

From our study, as reported on Tables 3.9 and 3.10, we observe that the IDNN, sRNN and GRU achieves a max CRSE orientation rate of 0.34, followed by the LSTM recording a max *CRSE* of 0.35 rad/s, whilst the MLP provided the worst performance of them all with a max *CRSE* of 0.97 rad/s. In an almost similar fashion, the IDNN, sRNN, LSTM and GRU obtain a max CRSE displacement of 17.96 m, whilst the MLP obtains a max *CRSE* of 156.23 m. However, as the IDNN is characterised by a significantly lower number of parameters compared to the GRU, LSTM and sRNN whilst providing similar CRSE scores across all NN studied and weight connections explored, we adopt it for use in learning the sensor noise in the accelerometer and gyroscope in this study. Table 3.8 shows the number of parameters characterising each NN across the various weights investigated; 8, 16, 32, 64, 96, 128, 192, 256 and 320.

Table 3.8. Number of trainable parameters in each Neural Network (NN) across various weighted connections.

Number of Weighted Connections	Number of Trainable Parameters				
	MLNN (2-Layer)	sRNN (2-Layer)	GRU (2-Layer)	LSTM (2-Layer)	IDNN (2-Layer)
8	33	65	185	245	65
16	97	225	657	873	161
32	321	833	2465	3281	449
64	1153	3201	9537	2705	1409
128	4353	12,545	37,505	49,985	4865
192	9601	28,033	83,905	111,841	10,369
256	16,897	49,665	148,737	198,273	17,921
320	26,241	77,441	232,001	309,281	27,521

Furthermore, we observe that the number of weighted parameters has little influence on the performance of the displacement and orientation rate estimation model. However, we notice that the number of time steps in the recurrent NN models (recurrent in both layer architecture and input structure such as the IDNN) significantly influences the accuracy of the model's prediction in both AccNet and GyroNet, but the change in the number of time steps had no impact on the WhONet model. The performance of the IDNN across several time steps ranging from 2–14 are presented in Tables 3.9 and 3.10.

Table 3.9. The performance evaluation based on the Cumulative Root Squared Error (CRSE) metric of the Input Delay Neural Network (IDNN) in each investigated scenario across several time steps on the orientation rate estimation (GyroNet model).

Number of Time Steps	Motorway (Rad/s)	Roundabout (Rad/s)	Quick Changes in		
			Vehicle Acceleration (Rad/s)	Hard Brake (Rad/s)	Sharp Cornering (Rad/s)
2	0.05	0.41	0.38	0.28	0.52
3	0.06	0.62	0.33	0.33	0.56
4	0.06	0.59	0.34	0.35	0.51
5	0.06	0.60	0.38	0.34	0.41
6	0.05	0.61	0.39	0.35	0.43

7	0.05	0.63	0.37	0.32	0.47
8	0.05	0.60	0.37	0.32	0.46
9	0.05	0.60	0.35	0.34	0.45
10	0.06	0.61	0.35	0.28	0.51
11	0.06	0.58	0.36	0.25	0.50
12	0.05	0.38	0.38	0.28	0.51
13	0.06	0.62	0.33	0.32	0.51
14	0.06	0.59	0.34	0.35	0.49

Table 3.10. Performance evaluation based on the CRSE metric of the IDNN in each investigated scenario across several time steps on the AccNet model.

NN	Number of Time Steps	Motorway (m)	Roundabout (m)	Quick Changes in Vehicle Acceleration (m)	Hard Brake (m)	Sharp Cornering (m)
IDNN	2	651.41	702.17	571.99	648.57	425.56
	4	616.60	655.22	546.76	580.01	373.03
	6	610.61	599.22	524.41	577.19	346.92
	8	592.27	595.09	474.55	557.50	292.78
	10	3.60	17.96	8.71	15.80	14.55
	12	3.23	19.52	8.62	19.36	14.43
	14	3.63	20.53	9.58	20.45	12.71
sRNN	2	17.11	55.58	33.30	64.09	42.64
	4	7.87	47.92	22.45	51.81	25.95
	6	7.28	29.10	16.56	25.28	22.58
	8	3.83	21.08	10.27	16.39	14.02
	10	3.60	17.96	8.71	15.80	14.55
	12	3.23	19.52	8.62	19.36	14.43
	14	3.63	20.53	9.58	20.45	12.71
GRU	2	21.19	51.54	36.66	62.04	45.82
	4	25.01	42.62	30.11	45.05	26.19
	6	20.24	33.72	24.64	23.87	22.20
	8	11.33	24.14	15.16	17.59	15.47

	10	3.60	17.96	8.71	15.80	14.55
	12	3.23	19.52	8.62	19.36	14.43
	14	3.63	20.53	9.58	20.45	12.71
	2	32.97	54.21	34.74	60.78	37.53
	4	18.20	41.62	26.73	51.94	28.21
	6	6.19	33.82	16.48	34.68	20.39
LSTM	8	4.12	21.75	11.49	16.18	13.8227
	10	3.60	17.96	8.71	15.80	14.55
	12	3.23	19.52	8.62	19.36	14.43
	14	3.63	20.53	9.58	20.45	12.71

We also comparatively analyse the performance of the IDNN, GRU, sRNN and LSTM on compact parameterisation for use in the proposed WhONet for accurate positional tracking. A detailed comparison of the IDNN, GRU, sRNN and LSTM is presented on Table 3.11. With an analysis performed on the 180s longer GNSS outage using the CTE and CRSE metric, the result so obtained shows that the sRNN is able to provide the most accurate estimations of the NNs compared while using a lower number of weighted parameters as presented on Table 3.8. Although the IDNN has fewer weighted parameters compared to the sRNN, the sRNN offers the best balance between accuracy and computational complexity. The performance of the sRNN on the wheel-speed-based position tracking reveals that the dynamic information from the short-term memory of the vehicle's motion is more important than long-term memory and, as such, is less affected by the vanishing gradient issue of the sRNN. As such, the sRNN is selected for use in WhONet.

Table 3.11. Performance comparison of the IDNN, LSTM, GRU and sRNN using the CTE and CRSE metric on the WhONet model.

Dataset	Performance Metrics	CTE (m)				CRSE (m)			
		IDNN	LSTM	GRU	sRNN	IDNN	LSTM	GRU	sRNN
V_Vtb3	Max	1.15	1.13	1.12	1.06	5.42	6.20	5.23	5.29
	Min	0.00	0.00	0.00	0.00	2.99	4.02	2.90	3.06
	μ	0.44	0.63	0.53	0.55	4.20	4.97	4.23	4.22
	(σ)	0.19	0.17	0.22	0.17	0.24	0.51	0.26	0.19
V_Vfb01c	Max	7.66	6.20	5.52	4.99	10.19	10.41	9.53	9.16

	Min	0.01	0.01	0.03	0.01	4.89	6.37	4.88	4.74
	μ	3.68	3.02	3.22	3.00	7.06	8.03	7.06	6.64
	(σ)	2.19	1.29	0.68	0.29	1.62	1.42	1.39	1.33
	Max	9.05	9.45	8.43	5.80	14.74	15.29	14.15	13.41
V_Vfb02a	Min	0.00	0.00	0.00	0.00	4.36	4.14	4.59	3.77
	μ	3.99	3.30	3.65	2.80	7.79	7.90	8.01	7.19
	(σ)	2.33	2.50	2.12	1.45	2.02	2.48	1.94	1.82
	Max	5.86	6.13	4.63	4.28	13.84	14.99	13.66	13.68
V_Vta1a	Min	0.00	0.00	0.00	0.00	5.19	6.02	5.09	5.44
	μ	3.07	3.24	2.10	2.07	8.18	9.95	8.11	7.71
	(σ)	1.04	1.44	1.07	0.94	1.99	2.27	2.06	2.08
	Max	1.65	2.94	1.54	1.34	9.87	14.99	10.33	9.70
V_Vfb02b	Min	0.00	0.00	0.01	0.01	4.63	7.61	4.74	4.55
	μ	0.87	1.53	0.95	0.76	7.62	11.05	7.50	7.29
	(σ)	0.41	0.82	0.45	0.42	1.53	2.23	1.39	1.28
	Max	7.44	10.62	7.68	6.94	10.09	14.25	10.39	9.57
V_Vfb02g	Min	0.05	0.01	0.00	0.00	5.60	6.80	5.49	5.03
	μ	5.31	4.74	4.98	3.76	8.21	9.31	8.15	7.24
	(σ)	1.97	1.58	2.16	1.84	1.21	1.73	1.03	1.11
	Max	9.72	5.03	9.21	9.12	11.11	10.95	12.11	10.78
V_St6	Min	0.00	0.00	0.00	0.00	3.49	3.91	3.25	3.46
	μ	2.72	2.13	2.93	2.78	6.40	6.13	6.54	6.29
	(σ)	2.29	1.17	2.65	2.32	1.62	1.44	1.97	1.69
	Max	4.30	4.47	4.01	4.15	9.60	10.98	9.65	9.70
V_St7	Min	0.00	0.00	0.00	0.00	2.85	3.45	2.92	2.71
	μ	1.85	1.69	1.60	1.61	5.74	6.96	5.58	5.70
	(σ)	0.81	1.32	0.85	0.78	1.49	2.28	1.72	1.61
	Max	5.38	4.54	5.42	5.14	11.86	12.30	12.24	12.00
V_S3a	Min	0.00	0.00	0.00	0.01	4.79	5.65	4.76	4.61
	μ	2.20	2.67	2.08	2.06	7.93	9.35	7.67	7.85
	(σ)	1.34	1.37	1.23	1.20	1.60	1.60	1.60	1.56

3.2.3.3 Model Training

The machine learning models are trained using the Keras–Tensorflow platform on the IO-VNB data subsets presented in Table 3.13. The IO-VNB datasets used to train the WhONet Model are characterised by about 1590 mins of drive time over a total distance of 1,165 km, whilst the CUPAC trainset is characterised by about 104 mins of drive over 54.9 km. The trained model on the IO-VNB dataset is used to evaluate the challenging driving scenarios in Chapter 4 and the IO-VNBD longer-term GNSS outage scenarios discussed in Chapter 5. The model trained on the CUPAC trainsets are used to evaluate the CUPAC longer-term GNSS outages also discussed in chapter 5. The CUPAC dataset

is used only in the longer term GNSS outage experiment as the dataset doesn't provide any information or label to suggest it contain features on complex driving scenarios. The models were optimised using the adamax optimiser with initial learning rates as shown in Table 3.12 and trained using the mean absolute error loss function and a dropout rate indicated in Table 3.12. Furthermore, the input features to the models were normalised between 0 and 1 to reduce learning bias. Table 3.12 highlights the parameters characterising the training of the WhONet model.

Table 3.12. Training parameters of models used in this thesis.

Parameters	AccNet	GyroNet	WhONet
Learning rate	0.004	0.001	0.0007
Dropout rate	10%	10%	5%
Time step	See Table 3	See Table 2	1
Hidden layers	2	2	2
Hidden neurons	32 per layer	32 per layer	72 per layer
Batch size	256	256	128

Table 3.13: IO-VNB data subsets used in training the models.

IO-VNB Dataset	Features
V-S1	B-road (B4101), roundabout (x9), reverse (x5), hilly road, A4053 (ring-road), hard-brake, tyre pressure E
V-S2	B-road (B4112, B4065), roundabout (x18), reverse drive (x8), motorway, dirt road, u-turn (x5), country road, successive left-right turns, hard-brake, A-roads (A4600), tyre pressure E
V-S3c	Roundabout(x4), A-road (A428), country roads, tyre pressure E
V-S4	Roundabout (x14), u-turn, A-road, successive left-right turns, swift maneuvers, change in speed, night-time, A-road (A429, A45, A46), ring-road (A4053), tyre pressure E
V-St1	Roundabout (x9), A-road (A452), B-road, car park navigation, tyre pressure E
V-M	Roundabout (x30), successive left-right turns, hard-brake (x21), swift maneuvers(x5), country roads, sharp turn left/right, daytime, u-turn (x1), u-turn reverse (x7), tyre pressure E
V-Y2	Roundabout(x9), u-turn/reverse(x1), A-road, B-road, country road, tyre pressure E
V-Vta2	Round About (x2), A Road (A511, A5121, A444), Country Road, Hard Brake, Tyre Pressure A

V-Vta8	Town Roads (Build-up), A-Roads (A511), Tyre Pressure A
V-Vta9	Hard-brakes, A-road (A50), tyre pressure A
V-Vta10	Round About (×1), A—Road (A50), Tyre Pressure A
V-Vta13	A-road (A515), country road, hard-brakes, tyre pressure A
V-Vta16	Round-About (×3), Hilly Road, Country Road, A-Road (A515), Tyre Pressure A
V-Vta17	Hilly Road, Hard-Brake, Stationary (No Motion), Tyre Pressure A
V-Vta20	Hilly Road, Approximate Straight-line travel, Tyre Pressure A
V-Vta21	Hilly Road, Tyre Pressure A
V-Vta22	Hilly Road, Hard Brake, Tyre Pressure A
V-Vta27	Gravel Road, Several Hilly Road, Potholes, Country Road, A-Road (A515), Tyre Pressure A
V-Vta28	Country Road, Hard Brake, Valley, A-Road (A515)
V-Vta29	Hard Brake, Country Road, Hilly Road, Windy Road, Dirt Road, Wet Road, Reverse (×2), Bumps, Rain, B-Road (B5053), Country Road, U-Turn (×3), Windy Road, Valley, Tyre Pressure A
V-Vta30	Rain, Wet Road, U-Turn (×2), A-Road (A53, A515), Inner Town Driving, B-Road (B5053), Tyre Pressure A
V-Vtb1	Valley, rain, Wet-Road, Country Road, U-Turn (×2), Hard-Brake, Swift-Manoeuvre, A—Road (A6, A6020, A623, A515), B-Road (B6405), Round About (×3), day Time, Tyre Pressure A
V-Vtb2	Country Road, Wet Road, Dirt Road, Tyre Pressure A
V-Vtb5	Dirt Road, Country Road, Gravel Road, Hard Brake, Wet Road, B Road (B6405, B6012, B5056), Inner Town Driving, A-Road, Motorway (M42, M1), Rush hour (Traffic) Round-About (×6), A-Road (A5, A42, A38, A615, A6), Tyre Pressure A
V-Vtb9	Approximate straight-line motion, night-time, wet road, hard-brakes, A-road (A5), tyre pressure A
V-Vw4	Round-About (×77), Swift-Manoeuvres, Hard-Brake, Inner City Driving, Reverse, A-Road, Motorway (M5, M40, M42), Country Road, Successive Left-Right Turns, Daytime, U-Turn (×3), Tyre Pressure D
V-Vw5	Successive Left-Right Turns, Daytime, Sharp Turn Left/Right, Tyre Pressure D
V-Vw14b	Motorway (M42), Night-time, Tyre Pressure D
V-Vw14c	Motorway (M42), Round About (×2), A-Road (A446), Night-time, Hard Brake, Tyre Pressure D
V-Vfa01	A-Road (A444), Round About (×1), B—Road (B4116) Day Time, Hard Brake, Tyre Pressure A

V-Vfa02	B-Road (B4116), Round About (×5), A Road (A42, A641), Motorway (M1, M62) High Rise Buildings, Hard Brake, Tyre Pressure C
V-Vfb01a	City Centre Driving, Round-About (×1), Wet Road, Ring Road, Night, Tyre Pressure C
V-Vfb01b	Motorway (M606), Round-About (×1), City Roads Traffic, Wet Road, Changes in Acceleration in Short Periods of Time, Night, Tyre Pressure C

Table 3.14. CUPAC data subsets used in training the models.

CUPAC Dataset	Features	Total Time Driven, Distance Covered, Velocity and Acceleration
Alpha 1	Inner-city, Parking lot, High traffic	6.37 mins, 2.31 km, 0.518 to 39.35 km/hr, -0.25 to 0.16 g
Alpha 2	Parking lot, Country road, Low	8.33 mins, 4.46 km, 0.004 to 64.577 km/hr, -0.22 to 0.27 g
Alpha 2	Inner-city, Country road, High traffic	8.33 mins, 3.93 km, 0.0 to 55.174 km/hr, -0.21 to 0.21 g
Alpha 2	Inner-city, High traffic	8.33 mins, 3.99 km, 0.007 to 70.376 km/hr, -0.36 to 0.24 g
Bravo 1	Inner-city, Medium traffic	5.89 mins, 1.57 km, 0.0 to 40.374 km/hr, -0.27 to 0.16 g
Bravo 2	Residential area, Road bumps, Low traffic	16.92mins 7.46 km, 0.004 to 65.405 km/hr, -0.44 to 0.33 g
Bravo 3	Residential area, Road bumps, Inner-city, Medium traffic	25.38 mins, 12.51m, 0.0 to 69.48 km/hr, -0.68 to 0.31 g
Charlie 1	Country road, Parking lot, Medium traffic	4.86 mins, 3.03 km, 0.004 to 62.68 km/hr, -0.26 to 0.21 g
Charlie 2	Inner-city, Country road, Low traffic	11.23 mins, 5.85 km, 0.004 to 58.104 km/hr, -0.38 to 0.27 g
Delta 1	Highway, Residential area, Low traffic	8.33 mins, 3.79 km, 0.004 to 53.654 km/hr, -0.19 to 0.25 g

3.2.3.4 Model Evaluation

In this research work, the models are evaluated on two scenarios; challenging scenarios as analysed in Chapter 4 and Longer-term GNSS outage scenarios as analysed in Chapter 5 and 6.

a) Challenging Scenarios

The data subsets used to investigate the performance of the localisation models on the challenging scenarios are presented in Tables 3.15 and 3.16. Although then evaluated on complex scenarios such as quick changes in acceleration, successive left and right turns, wet road, hard brake, sharp cornering or roundabouts, the performance of the models are first examined on the V-Vw12 dataset of the IO-VNBD, which presents a relatively easy scenario; i.e., an approximate straight-line travel on the motorway. The evaluation of the latter scenario aims at gauging the performance of the technique in a relatively simple driving situation. Nonetheless, the Motorway scenario could be challenging to track due to the large distance covered per second.

Before the evaluation of the datasets from each challenging scenario, the datasets are down sampled from 10 Hz to 1 Hz and broken down into test sequences of 10 seconds length. For the purpose of investigating the robustness of the positioning models, GNSS outages are assumed on the datasets in Table 3.15 and 3.16. The maximum, minimum, average and standard deviation, of the CRSE's and CTE's of all the test sequences evaluated within each dataset are recorded in each scenario and used in evaluating the performance of each model.

Table 3.15. IO-VNB data test subset used in the motorway scenario.

Scenario	IO-VNB Data Subset	Total Time Driven, Distance covered, Velocity and Acceleration
Motorway V-Vw12		1.75 min, 2.64 km, 82.6 to 97.4 km/hr, -0.06 to +0.07 g

Table 3.16. IO-VNB data test subset used in the challenging scenarios.

Challenging Scenarios	IO-VNB Data Subset	Total Time Driven, Distance Covered, Velocity and Acceleration
Roundabout	V-Vta11	1.0 min, 0.92 km, 26.8 to 97.7 km/hr, -0.45 to +0.15 g
	V-Vfb02d	1.5 min, 0.84 km, 0.0 to 57.3 km/hr, -0.33 to +0.31 g

Changes in acceleration	V-Vfb02e	1.6 min, 1.52 km, 37.4 to 73.9 km/hr, -0.24 to +0.19 g
	V-Vta12	1.0 mins, 1.27 km, 44.7 to 85.3 km/hr, 0.44 to +0.13 g
Hard Brake	V-Vw16b	2.0 mins, 1.99 km, 1.3 to 86.3 km/hr, -0.75 to +0.29 g
	V-Vw17	0.5 min, 0.54 km, 31.5 to 72.7 km/hr, -0.8 to +0.19 g
	V-Vta9	0.4 min, 0.43 km, 48.9 to 87.7 km/hr, -0.6 to +0.14 g
Sharp Cornering and Successive Left and Right Turns	V-Vw6	2.1 mins, 1.08 km, 3.3 to 40.7 km/hr, -0.34 to +0.26 g
	V-Vw7	2.8 mins, 1.23 km, 0.4 to 42.2 km/hr, -0.37 to +0.37 g
	V-Vw8	2.7 mins, 1.12 km, 0.0 to 46.4 km/hr, -0.37 to +0.27 g
Wet Road	V-Vtb8	1.2 mins, 1.35 km, 60.9 to 76.5 km/hr, -0.35 to 0.08 g
	V-Vtb11	0.7 min, 0.84 km, 65.1 to 75.3 km/hr, -0.05 to 0.12 g
	V-Vtb13	2.1 mins, 0.99 km, 7.5 to 43.3 km/hr, -0.31 to 0.22 g

b) Long-Term Outages

The data subsets used in investigating the performance of the WhONet models and the physical model in the longer-term outage scenarios are presented in Tables 3.17 and 3.18. The models are evaluated on longer GNSS scenarios of 30s, 60s, 120s and 180s. In the longer term GNSS outage scenarios, each dataset is broken down into test sequences of 30s, 60s, 120s or 180s depending on the outage scenario being evaluated. The maximum, minimum, average and standard deviation, of the CRSE's and CTE's of all the test sequences evaluated within each dataset are recorded in each scenario and used in evaluating the performance of each model.

GPS outages are assumed on the test scenarios, for the purpose of the investigation with a prediction frequency of 1s just as in the challenging scenario.

Table 3.17. IO-VNB data subsets used for the longer GNSS outage scenario performance evaluation

IO-VNB Dataset	Features	Total Time Driven, Distance Covered, Velocity and Acceleration
V-Vtb3	Reverse, Wet Road, Dirt Road, Gravel Road, Night-time, Tyre Pressure A	13.8 mins, 0.71 km, 0.0 to 37.5 km/hr, -0.23 to 0.33 g
V_Vfb01c	Motorway (M62), wet-road, heavy traffic, nighttime, tyre pressure C	10.5 mins, 10.66 km, 0.2 to 104.5 km/hr, -0.36 to 0.38 g
V_Vfb02a	Motorway (M1), roundabout (x2), A-road (A650), nighttime, hard-brakes, tyre pressure D	59.9 mins, 96.5 km, 0.0 to 122.3 km/hr, -0.5 to 0.37 g

V_Vta1a	Wet road, gravel road, country road, sloppy roads, roundabout (x3), hard-brake on wet road, tyre pressure A	43.0 mins, 40.74 km, 0.0 to 103.4 km/hr, -0.54 to 0.35 g
V_Vfb02b	Roundabout (x1), bumps, successive left-right turns, hard-brakes (x7), swift-maneuvers, nighttime, tyre pressure D	18.3 mins, 7.69 km, 0.0 to 84.3 km/hr, -0.5 to 0.35 g
V_Vfb02g	Motorway (M1), A-road (A42, A444, A5), country road, roundabout (x2), hard-brakes, nighttime, tyre pressure D	45.3 mins, 63.56 km, 0.0 to 119.4 km/hr, -0.51 to 0.35 g
V_St6	Motorway(M40), daytime, tyre pressure E	85.6 mins, 113.63 km, 0.0 to 122.1 km/hr, -0.32 to 0.35 g
V_St7	Motorway (M40), residential roads, A-road (A46), tyre pressure E	74.0 mins, 90.06 km, 0.0 to 117.9 km/hr, -0.3 to 0.3 g
V-S3a	Round-about (x15), u-turn/reverse drive (x4), motorway (M6), A-road (A4600, A426), hard-brake, swift maneuvers, country roads, change in speed, night-time, sharp turn left/right, tyre pressure E	41.1 mins, 26.0 km, 0.0 to 98.0 km/hr, -0.57 to 0.4 g

Table 3.18. CUPAC data subsets used for the longer GNSS outage scenario performance evaluation

CUPAC Dataset	Total Time Driven, Distance Covered, Velocity and Acceleration
Charlie3	13.8 mins, 0.71 km, 0.004 to 77.252 km/hr, -0.42 to 0.25 g
Charlie 4	10.5 mins, 10.66 km, 0.007 to 58.694 km/hr, -0.34 to 0.31 g
Delta 2	59.9 mins, 96.5 km, 0.004 to 37.224 km/hr, -0.26 to 0.25 g
Delta 3	43.0 mins, 40.74 km, 0.004 to 60.75 km/hr, -0.36 to 0.25 g

3.3 Summary

This chapter defined the datasets and methodology used in designing the deep learning and physics models for vehicular localisation. Firstly, the chapter introduced the IO-VNB dataset and CUPAC dataset which were used to train the deep learning models and used for the performance analysis in the rest of the thesis. The chapter then

discussed the methodology used in this thesis. The ground-truth formulations needed as targets for training the deep learning models and needed as baselines for comparing during the model evaluation were described. Furthermore, we defined the physics models and deep learning models for position estimation using the accelerometer and wheel encoder as well as orientation rate estimation using the gyroscope. We defined the metric used to evaluate the performance of each model and the training procedure for each of the deep learning models. Finally, we justified the selection of the IDNN for AccNet and GyroNet as well as sRNN for the WhONet and described the datasets used in evaluating the performance of each model in the remainder of this thesis. The choice of the IDNN and the sRNN highlights the vehicular positioning problem as one characterised by short memory (a characteristics not previously known prior to this research).

In the next chapter, the results from the performance analysis of the deep learning models and physics models are evaluated on the challenging scenarios discussed in Section 3.2.3.4.a.

Chapter 4

Results and Analysis on Position and Orientation Estimation in Challenging (Complex) GNSS Environments.

In the previous chapter, we described the datasets, trained deep learning models and physics models, in this chapter, we will now apply the trained deep learning models and physics models to estimate the position and orientation of the vehicle in challenging or complex Scenarios. The deep learning models; AccNet, WhONet and GyroNet, are compared to their corresponding physics derivations: APM, WPM and GPM using several performance metrics, all defined in Chapter 3. The superiority of the deep learning models over the physics models are demonstrated over six scenarios we consider challenging; Motorway, Roundabout, Quick change in acceleration, Successive left and right turns and sharp cornering, Hard brake and Wet road.

4.1. Challenging Localisation Environments

Previous research on vehicle positioning does not take into consideration complex scenarios such as hard brake, sharp cornering or roundabouts. Hence, the evaluation of the performance of positioning algorithms present in most published works may not accurately reflect real-life vehicular driving experience. Moreover, as those complex scenarios present strong challenges for vehicle tracking, it seems essential for the reliability of the algorithms that they are assessed under such scenarios:

4.1.1 Roundabout

Roundabouts present a particular struggle due to their shape. The circular and unidirectional traffic flow makes it a challenge to track the vehicle's orientation and displacement particularly due to the continuous change in the vehicle's direction whilst navigating the roundabout. Different roundabout sizes were considered in this study.

4.1.2 Quick Changes in Acceleration

The accuracy of the displacement estimation of the inertial sensors are affected by quick and varied changes to the acceleration of the vehicle within a short period of time. This is particularly a challenge as the inertial sensors struggle to capture the quick change in the vehicle's displacement thereafter.

4.1.3 Hard Brake

According to (Simons-Morton et al. 2009), hard brakes are characterised by a longitudinal deceleration of ≤ -0.45 g. They occur when the brake pad of the vehicle has a large force applied to it. The sudden halt to the motion of the vehicle leads to a steep decline in the velocity of the vehicle, thus making it difficult to predict the vehicle coming to a stop and to track the motion of the vehicle thereafter. This scenario poses a major challenge to the displacement estimation of the vehicle.

4.1.4 Successive Left and Right Turns and Sharp Cornering.

The sudden and consecutive change in the direction of the vehicle also poses a challenge to the orientation estimation of the vehicle. The inertial sensors struggle to accurately capture the sudden sharp changes to the orientation of the vehicle as well as continuous consecutive changes to the vehicle in relatively short periods of time.

4.1.5 Wet Road

When a vehicle is driven over a wet/muddy road, the wheels tend to slip whilst driving. This introduces uncertainties to the wheel speed estimation, leading to errors in the displacement calculation of the vehicle.

4.2. Results and Discussion

The performance of the dead reckoned APM, WPM and GPM as well as the proposed deep learning approaches (WhONet, AccNet and GyroNet) are analysed comparatively across several GPS outage simulated sequences, each of 10s length. The positioning techniques are first analysed on a less challenging scenario involving vehicle travel on an approximate straight line on the motorway to gauge their performance on a relatively easy driving situation. Further analysis is then done on more challenging scenarios such as hard brake, roundabouts, quick changes in acceleration and sharp cornering and successive left and right turns using the performance metrics defined in Chapter 3. Nonetheless, the motorway scenario could be considered challenging due to the large distance covered per second. GPS outages are assumed on the test scenarios with a prediction frequency of 1s. Each test set used in the challenging (complex) scenario is divided into several test sequences of 10 seconds length each. The maximum, minimum, average and standard deviation, of the CRSE's and CTE's of all the test sequences evaluated within each dataset are recorded in each scenario and used in evaluating the performance of each model.

4.2.1. Motorway Scenario

In evaluating the performance of the physics models and the deep learning approaches on vehicular motion tracking, both techniques are investigated on a less challenging trajectory characterised by an approximate straight-line drive on the motorway. The results, as shown on Table 4.1-4.3, shows that across all 10 test sequences evaluated on the motorway scenario, the deep learning model significantly outperforms the physics model across all metrics considered. The APM, WPM and GPM records its best CRSE of 1.21 m, 0.36 m and 0.07 rad/s respectively compared to 0.84 m, 0.13 m and 0.02 rad/s respectively of the AccNet, WhONet and GyroNet. Essentially, this shows that WhONet is able to reduce the positional CRSE of the WPM by up to 83% after about 268 m of travel. Furthermore, the AccNet offers up to an 89% improvement on the displacement max CRSE metric of the APM and the GyroNet offers an improvement of 69% over the GPM's CRSE. Even more, it can be seen that the WhONet provides better position estimations compared to the AccNet as is shown on

Figures 4.1-4.4. Achieving a CTE best of 0.0001 m Northwards and 0.0002 m Eastwards, the results also indicate that it is possible to localise the vehicle with lane-level accuracy using WhONet and GyroNet within 10 s of travel. Being the lowest errors across all scenarios evaluated as shown in Figures 4.5 and 4.6 we can infer that the motorway scenario was the least challenging scenario due to minimal accelerations and directional changes. Furthermore, the reliability of WhONet in consistently tracking the vehicles' motion with such accuracy is highlighted by its low standard deviation of 0.04. Figure 4.11b shows the trajectory of the vehicle along the motorway.

Table 4.1. The experimental results of AccNet and APM on the motorway scenario.

IO-VNB Dataset	Performance Metrics	Position Estimation Error (m)				Total Distance Travelled (m)	Number of Test Sequences evaluated
		CTE		CRSE			
		AccNet	APM	AccNet	APM		
V_w12	Max	2.56	30.30	3.23	30.30	268	10
	Min	0.19	0.28	0.84	1.21	235	
	(μ)	0.96	14.41	1.93	14.80	250	
	(σ)	0.84	10.00	0.84	9.50	11	

Table 4.2. The experimental results of WhONet and WPM on the motorway scenario.

IO-VNB Dataset	Performance Metrics	Position Estimation Error (m)				Total Distance Travelled (m)	Number of Test Sequences evaluated
		CTE		CRSE			
		WhONet	WPM	WhONet	WPM		
V_w12	Max	0.23	1.34	0.33	1.96	268	10
	Min	0.00	0.04	0.13	0.36	235	
	(μ)	0.10	0.52	0.26	1.07	250	
	(σ)	0.08	0.46	0.04	0.45	11	

Table 4.3. The experimental results of GyroNet and GPM on the motorway scenario.

IO-VNB Dataset	Performance Metrics	Orientation Rate Estimation Error (rad/s)	Total Distance	Number of Test
----------------	---------------------	---	----------------	----------------

		CTE		CRSE		Travelled (m)	Sequences evaluated
		GyroNet	GPM	GyroNet	GPM		
V_w12	Max	0.06	0.15	0.06	0.19	268	10
	Min	0.00	0.03	0.02	0.07	235	
	(μ)	0.03	0.10	0.04	0.13	250	
	(σ)	0.02	0.04	0.01	0.04	11	

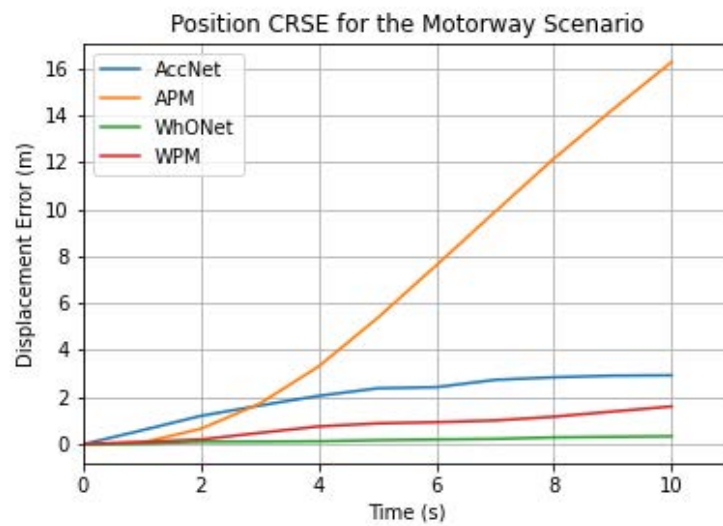


Figure 4.1. Sample evolution of the estimation error over time in the motorway scenario based on the position CRSE

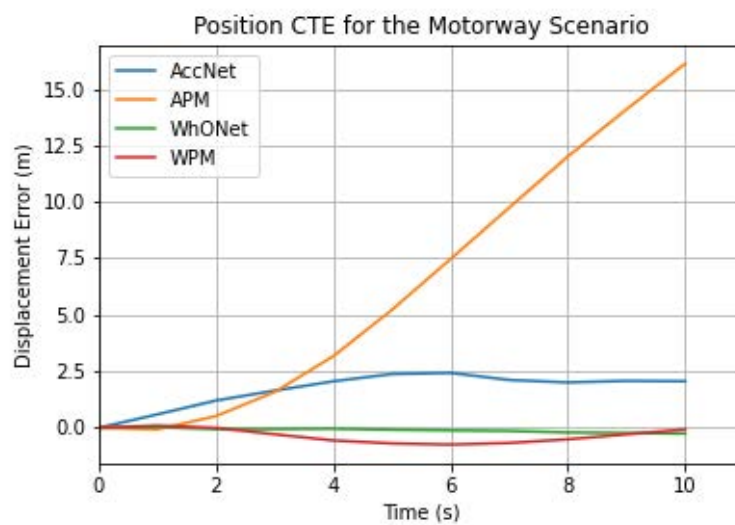


Figure 4.2. Sample evolution of the estimation error over time in the motorway scenario based on the position CTE

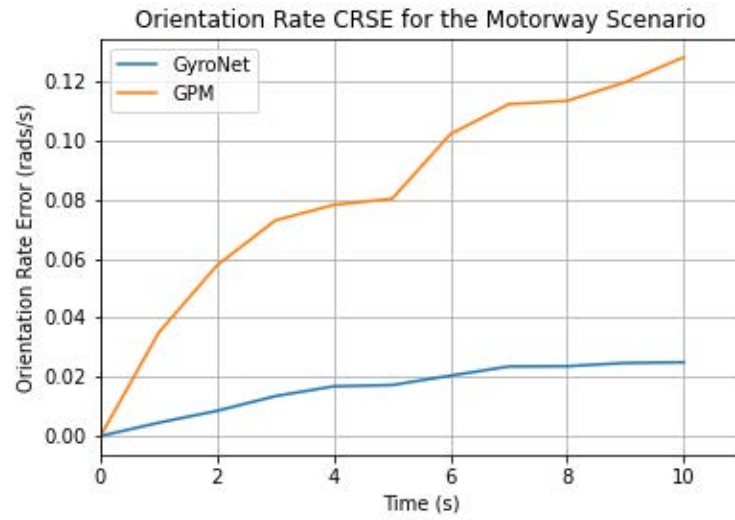


Figure 4.3. Sample evolution of the estimation error over time in the motorway scenario based on the orientation rate CRSE

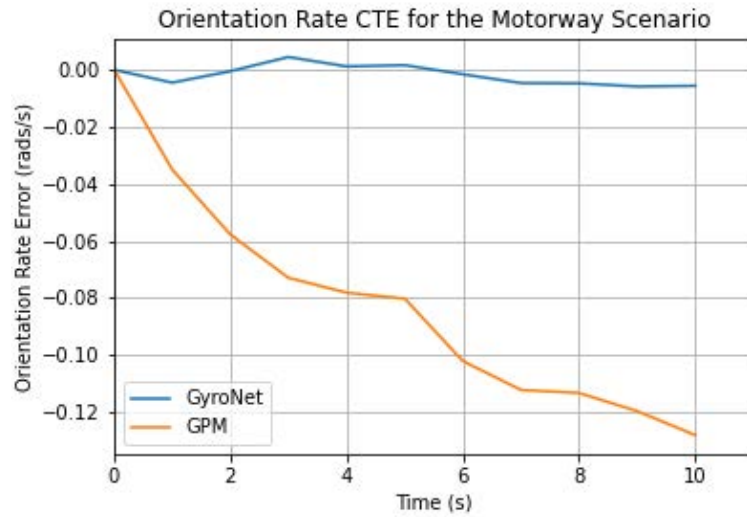


Figure 4.4. Sample evolution of the estimation error over time in the motorway scenario based on the orientation rate CTE

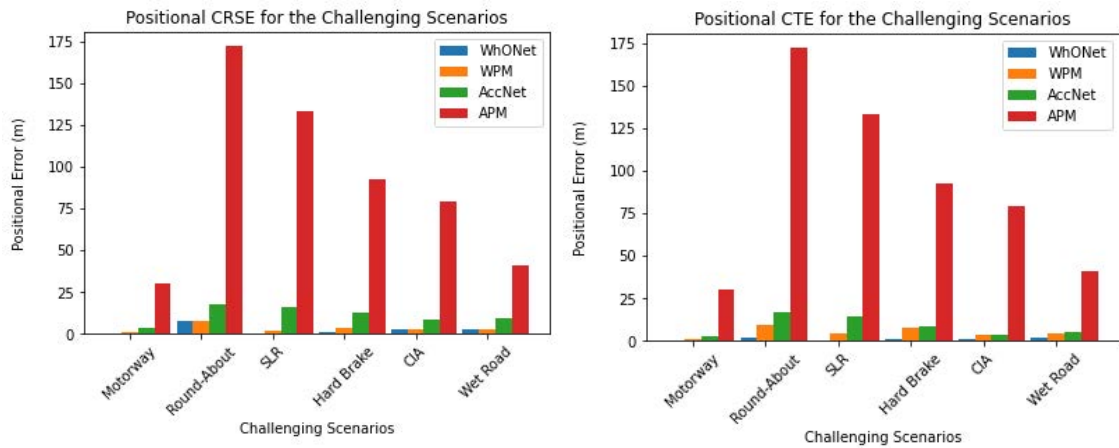


Figure 4.5. The comparison of the CRSE and CTE performance of the WhONet, WPM, AccNet and APM across all investigated challenging scenarios on the displacement estimation.

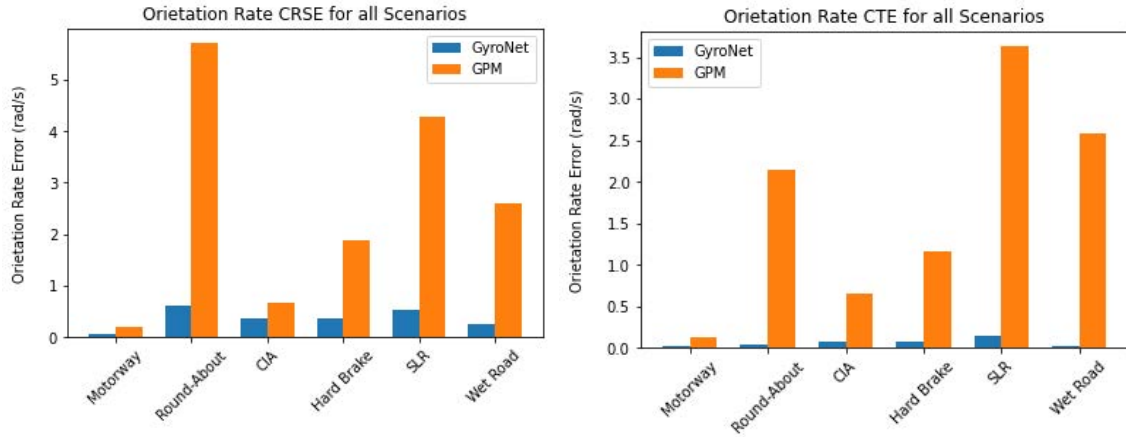


Figure 4.6. The comparison of the CRSE and CTE performance of the GyroNet and GPM across all investigated challenging scenarios on the orientation rate estimation.

4.2.2. Roundabout Scenario

The roundabout scenario is one of the most challenging for both the estimation of vehicular position and orientation rate. The difficulty encountered by the physics models and deep learning models in accurately tracking the vehicle's motion is graphically shown in Figure 4.7-4.10 with a comparative illustration to other investigated scenarios presented in Figures 4.5 and 4.6. The results so obtained as presented on Table 4.4-4.6 show that the deep learning models recorded a lower position estimation (maximum CRSE and CTE of 17.96 m and 16.80 m respectively for AccNet, and 7.35 m and 1.66 m respectively for WhONet) than the physics models (maximum CRSE and CTE displacement of 171.92 m for APM and 8.61 and 7.32 respectively for the WPM) as well as a lower orientation rate (maximum CRSE and CTE of 0.38 rad/s and 0.04 rad/s, respectively) than the GPM (maximum CRSE and CTE of 5.71 rad/s and 2.14 rad/s, respectively). The relatively lower standard deviation across all analysed metrics is evidence that the deep learning models are able to more consistently track the vehicle's position and orientation on the roundabout scenario but less consistently on other investigated scenarios. As expected, the WhONet provides an improvement of up to 99% over the AccNet position estimations across the two datasets investigated and numerous test sequences evaluated. The roundabout scenario study was carried out across 13 test sequences over a maximum travel

distance of approximately 262 m. Figure 4.11a shows a sample trajectory of the vehicle on the roundabout scenario analysis.

Table 4.4. The experimental results of AccNet and APM on the roundabout scenario.

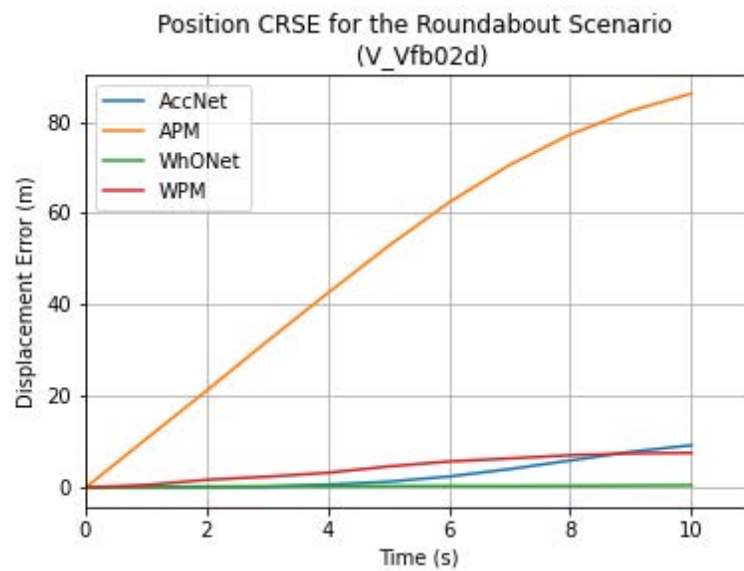
IO-VNB Dataset	Performance Metrics	Position Estimation Error (m)				Total Distance Travelled (m)	Number of Test Sequences evaluated
		CTE		CRSE			
		AccNet	APM	AccNet	APM		
V_Vta11	Max	16.80	171.92	17.96	171.92	262	5
	Min	2.01	29.34	4.61	35.44	85	
	(μ)	7.61	123.95	12.09	125.47	159	
	(σ)	5.63	56.12	5.76	53.55	67	
V_Vfb02d	Max	15.01	98.23	15.01	98.23	151	8
	Min	0.50	19.43	2.36	19.43	14	
	(μ)	4.24	48.56	6.66	51.37	96	
	(σ)	4.77	27.37	4.24	25.84	52	

Table 4.5. The experimental results of WhONet and WPM on the roundabout scenario.

IO-VNB Dataset	Performance Metrics	Position Estimation Error (m)				Total Distance Travelled (m)	Number of Test Sequences evaluated
		CTE		CTE			
		WhONet	WPM	WhONet	WPM		
V_Vta11	Max	1.66	7.31	7.35	8.61	262	5
	Min	0.00	0.00	0.11	0.78	85	
	(μ)	0.56	2.30	1.75	3.95	159	
	(σ)	0.48	2.44	2.66	2.85	67	
V_Vfb02d	Max	0.22	2.91	0.49	9.37	151	8
	Min	0.00	0.80	0.14	5.11	14	
	(μ)	0.11	1.94	0.30	6.70	96	
	(σ)	0.07	0.87	0.09	1.90	52	

Table 4.6. The experimental results of GyroNet and GPM on the roundabout scenario.

IO-VNB Dataset	Performance Metrics	Orientation Rate Estimation Error (rad/s)				Total Distance Travelled (m)	Number of Test Sequences evaluated
		CTE		CRSE			
		GyroNet	GPM	GyroNet	GPM		
V_Vta11	Max	0.06	6.71	0.61	6.71	262	5
	Min	0.00	0.62	0.08	0.62	85	
	(μ)	0.03	2.61	0.21	3.26	159	
	(σ)	0.02	2.15	0.19	2.23	67	
V_Vfb02d	Max	0.09	2.43	0.35	2.44	151	8
	Min	0.00	0.05	0.03	0.17	14	
	(μ)	0.04	0.49	0.15	0.66	96	
	(σ)	0.03	0.77	0.12	0.72	52	

**Figure 4.7.** Sample evolution of the estimation error over time in the roundabout scenario based on the position CRSE

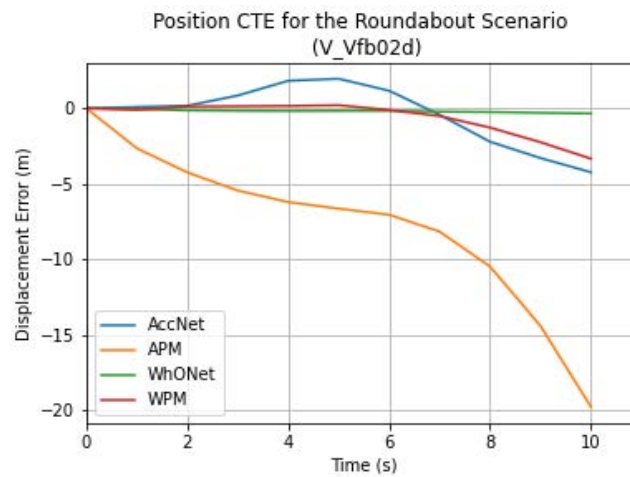


Figure 4.8. Sample evolution of the estimation error over time in the roundabout scenario based on the position CTE

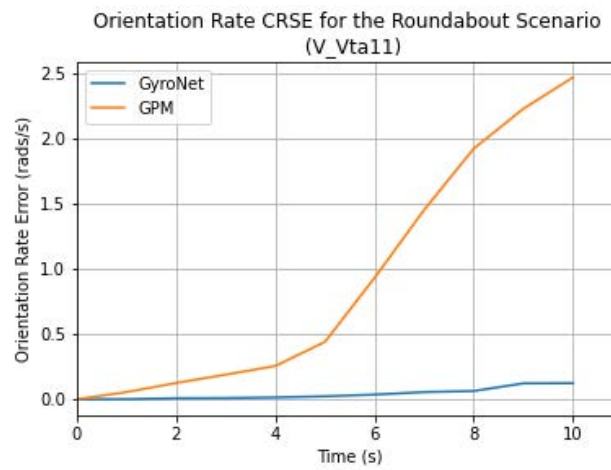


Figure 4.9. Sample evolution of the estimation error over time in the roundabout scenario based on the position CRSE

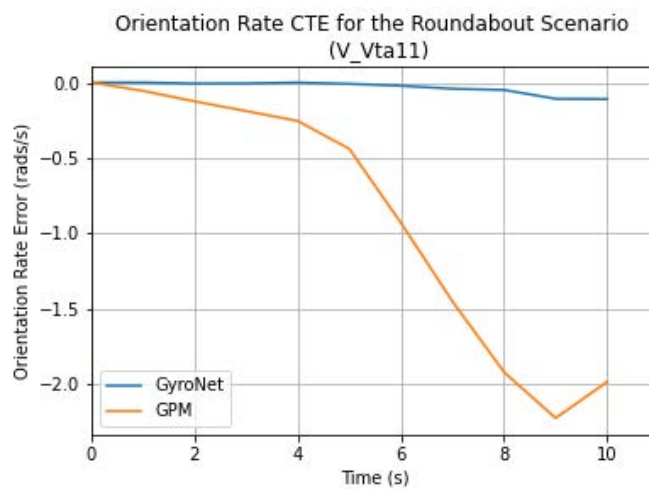


Figure 4.10. Sample evolution of the estimation error over time in the roundabout scenario based on the Orientation rate CTE.



Figure 4.11. Sample trajectory of the (a) V-Vta11 roundabout data subset of the Inertia and Odometry Vehicle Navigation Dataset (IO-VNBD) and (b) V-Vw12 motorway data subset of the IO-VNBD.

4.2.3. Quick Changes in Vehicle Acceleration Scenario

The results presented in Table 4.7-4.9 illustrate the performance of the deep learning-based models over the physics models in the quick changes in acceleration scenario. From observation, it can be seen that the deep learning models significantly outperform the physics models across all metrics employed, with a maximum CRSE of 2.82 m, 7.45 m, 0.34 rad/s for the WhONet, AccNet and GyroNet against 4.64 m, 79.41 m and 0.41 rad/s for the WPM, APM and GPM over a maximum distance of approximately 192 m covered on the V_Vta11 dataset. However, on the V_Vfb02d dataset, over a maximum distance of 218 m, the WhONet, AccNet and GyroNet obtained a maximum CRSE of 2.27 m, 8.62 m, 0.20 rad/s respectively, while the WPM, APM and GPM obtained a maximum CRSE of 5.39 m, 40.26 m, 0.53 rad/s respectively. This shows, as expected, that the physics models and deep learning models found it more challenging to estimate the position of the vehicle compared to the orientation rate.

Furthermore, considering both datasets, the WhONet, AccNet and GyroNet obtain a maximum CTE of 1.62 m, 6.99 m and 0.05rad/s compared to that of the WPM, APM and GPM recorded as 38.92 m, 26.23 m and 3.72 rad/s across all 15 test sequences evaluated. By comparison, the WhONet offers up to a 99% error reduction on the

AccNet. Figure 4.12-4.15 graphically illustrates the evolution of the error across sample sequences on the CRSE and CTE metrics. A comparison of the performance of both approaches across all scenarios investigated is further presented in Figures 4.5 and 4.6.

Table 4.7. The performance of AccNet and APM on the quick changes in acceleration scenario.

IO-VNB Dataset	Performance Metrics	Position Estimation Error (m)				Total Distance Travelled (m)	Number of Test Sequences evaluated
		CTE		CRSE			
		AccNet	APM	AccNet	APM		
V_Vta11	Max	4.24	79.41	7.45	79.41	192	9
	Min	0.10	23.60	2.38	23.60	123	
	(μ)	1.65	45.78	4.68	45.78	156	
	(σ)	1.51	17.20	1.94	17.20	19	
V_Vfb02d	Max	6.99	40.26	8.62	40.26	218	6
	Min	0.23	2.01	2.93	16.62	145	
	(μ)	3.20	22.41	6.30	26.79	178	
	(σ)	2.19	14.57	2.18	9.94	24	

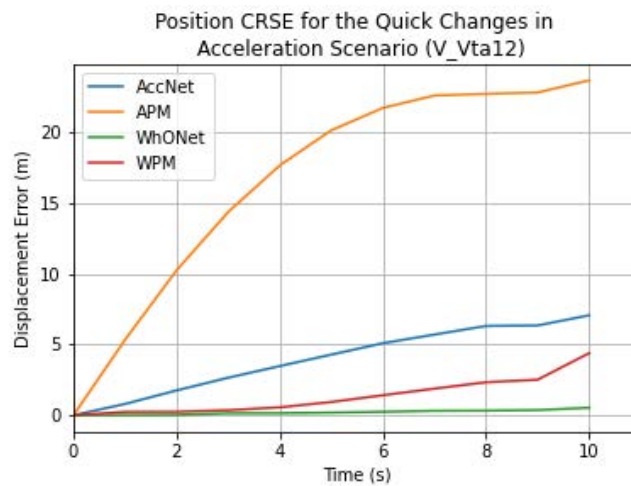
Table 4.8. The performance of WhONet and WPM on the quick changes in acceleration scenario.

IO-VNB Dataset	Performance Metrics	Position Estimation Error (m)				Total Distance Travelled (m)	Number of Test Sequences evaluated
		CTE		CRSE			
		WhONet	WPM	WhONet	WPM		
V_Vta11	Max	1.20	3.35	2.82	4.64	192	9
	Min	0.00	0.08	0.17	1.49	123	
	(μ)	0.53	1.65	1.14	2.94	156	
	(σ)	0.39	1.17	0.81	1.01	19	
V_Vfb02d	Max	1.62	3.72	2.27	5.39	218	6
	Min	0.00	0.20	0.14	2.16	145	
	(μ)	0.63	1.83	0.89	3.76	178	

(σ)	0.38	1.03	0.49	1.13	24
------------	------	------	------	------	----

Table 4.9. The performance of GyroNet and GPM on the quick changes in acceleration scenario.

IO-VNB Dataset	Performance Metrics	Orientation Rate Estimation Error (rad/s)				Total Distance Travelled (m)	Number of Test Sequences evaluated
		CTE		CRSE			
		GyroNet	GPM	GyroNet	GPM		
V_Vta11	Max	0.05	0.39	0.34	0.41	192	9
	Min	0.00	0.04	0.04	0.14	123	
	(μ)	0.02	0.15	0.16	0.27	156	
	(σ)	0.02	0.12	0.10	0.08	19	
V_Vfb02d	Max	0.03	0.53	0.20	0.53	218	6
	Min	0.00	0.11	0.04	0.18	145	
	(μ)	0.02	0.27	0.11	0.32	178	
	(σ)	0.01	0.15	0.05	0.12	24	

**Figure 4.12.** Sample evolution of the estimation error over time in the quick changes in acceleration scenario based on the position CRSE

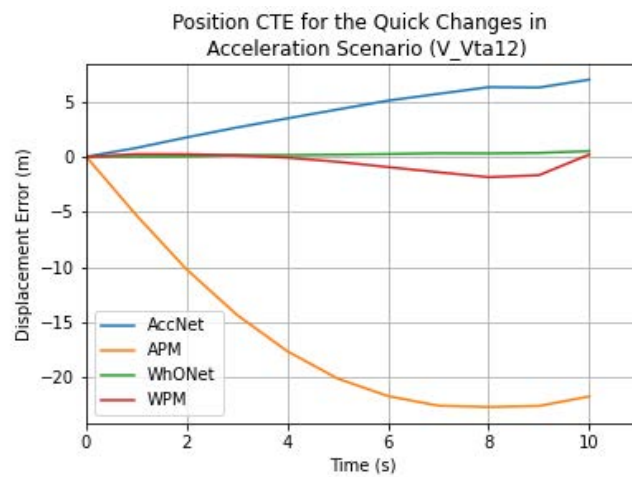


Figure 4.13. Sample evolution of the estimation error over time in the quick changes in acceleration scenario based on the position CTE

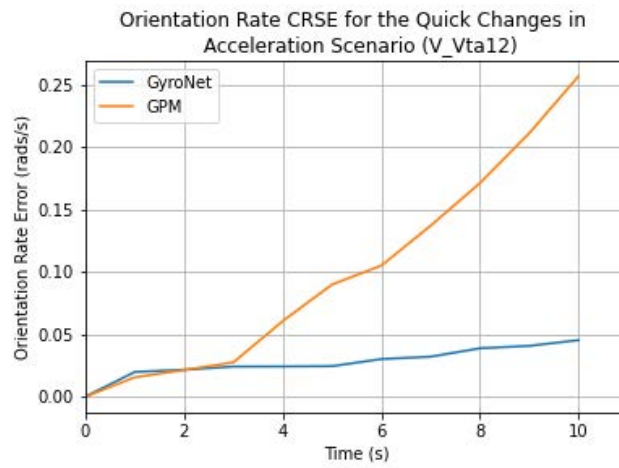


Figure 4.14. Sample evolution of the estimation error over time in the quick changes in acceleration scenario based on the Orientation rate CRSE

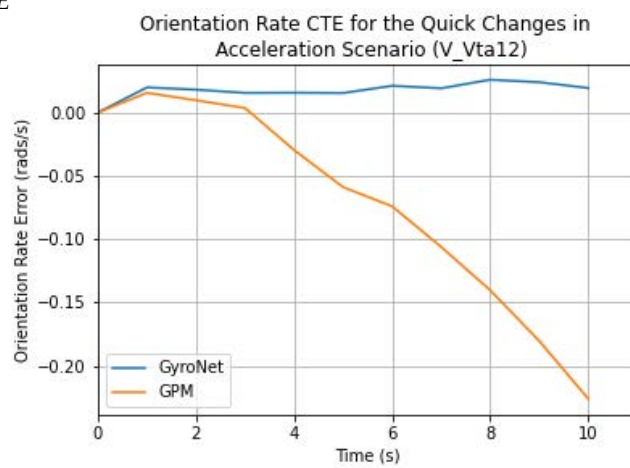


Figure 4.15. Sample evolution of the estimation error over time in the quick changes in acceleration scenario based on the Orientation rate CTE.

4.2.4. Hard Brake Scenario

The performance of the deep learning models over the physics models in the hard-brake scenario is evaluated over 14 test sequences averaging 170 m of travel with a 234 m maximum journey length. From Table 4.10-4.12, we observe that much to our expectations, the hard brake scenario proves to be more of a challenge for the accelerometer than the wheel encoder or the gyroscope, as the APM struggles to accurately estimate the vehicle's position within the simulated GNSS outage period. As further emphasized on Figures 4.16 - 4.19, the deep learning models significantly outperform the physics models across all performance metrics employed. The WhONet model offers up to a 91% reduction of the WPM's CRSE, AccNet offers an 89% improvement compared to the APM's estimation, and the GyroNet offers up to 83% improvement on the GPM's estimations. The reliability of the WhONet, AccNet and GyroNet in consistently correcting their corresponding physics model estimations to such accuracy is further established by their σ value of 0.01, 4.23 and 0.48 respectively. The WhONet outperforms the AccNet in the vehicle's position estimation with a maximum CRSE of 0.88 m compared to 15.80 m of the of the AccNet.

Table 4.10. The performance of AccNet and APM on the hard brake scenario.

IO-VNB Dataset	Performance Metrics	Position Estimation Error (m)				Total Distance Travelled (m)	Number of Test Sequences evaluated
		CTE		CRSE			
		AccNet	APM	AccNet	APM		
V_Vw16b	Max	14.75	133.12	15.80	133.12	234	11
	Min	0.39	12.01	1.53	14.09	87	
	(μ)	4.82	57.13	7.44	57.34	170	
	(σ)	4.84	38.99	4.99	38.75	50	
V_Vw17	Max	3.59	41.56	12.03	41.56	175	3
	Min	2.78	22.95	9.37	23.03	157	
	(μ)	3.19	32.26	10.70	32.30	169	
	(σ)	0.40	9.31	1.33	9.27	8	

Table 4.11. The performance of WhONet and WPM on the hard brake scenario.

IO-VNB Dataset	Performance Metrics	Position Estimation Error (m)				Total Distance Travelled (m)	Number of Test Sequences evaluated
		CTE		CRSE			
		WhONet	WPM	WhONet	WPM		
V_Vw16b	Max	0.81	7.31	0.88	9.99	234	11
	Min	0.00	0.00	0.10	0.80	87	
	(μ)	0.20	2.30	0.36	4.04	170	
	(σ)	0.23	2.44	0.22	3.04	50	
V_Vw17	Max	0.37	2.91	0.87	8.07	175	3
	Min	0.20	0.80	0.61	5.52	157	
	(μ)	0.26	1.94	0.78	6.40	169	
	(σ)	0.01	0.87	0.01	1.19	8	

Table 4.12. The performance of GyroNet and GPM on the hard brake scenario.

IO-VNB Dataset	Performance Metrics	Orientation Rate Estimation Error (rad/s)				Total Distance Travelled (m)	Number of Test Sequences evaluated
		CTE		CRSE			
		GyroNet	GPM	GyroNet	GPM		
V_Vw16b	Max	0.02	0.60	0.36	2.08	234	11
	Min	0.00	0.01	0.03	0.08	87	
	(μ)	0.01	0.12	0.10	0.35	170	
	(σ)	0.01	0.19	0.09	0.57	50	
V_Vw17	Max	0.02	0.05	0.05	0.13	175	3
	Min	0.00	0.01	0.05	0.09	157	
	(μ)	0.02	0.03	0.05	0.11	169	
	(σ)	0.00	0.02	0.00	0.02	8	

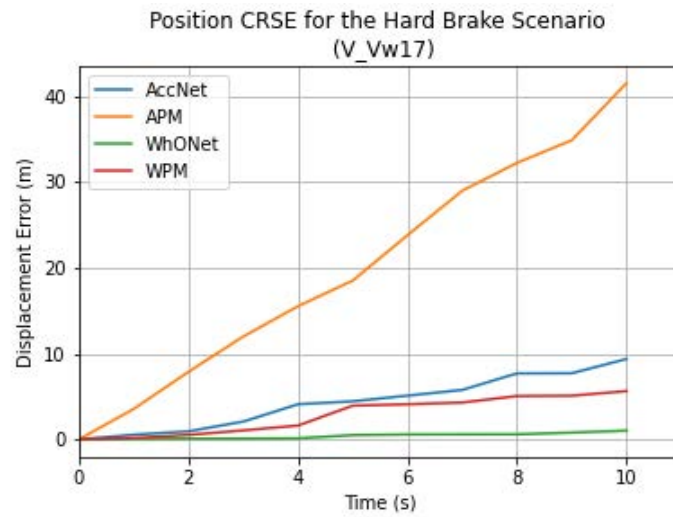


Figure 4.16. Sample evolution of the estimation error over time in the hard brake scenario based on the position CRSE

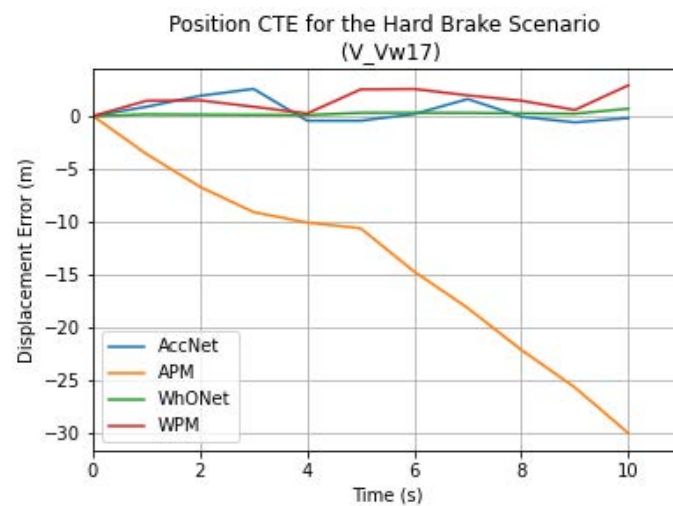


Figure 4.17. Sample evolution of the estimation error over time in the hard brake scenario based on the position CTE.

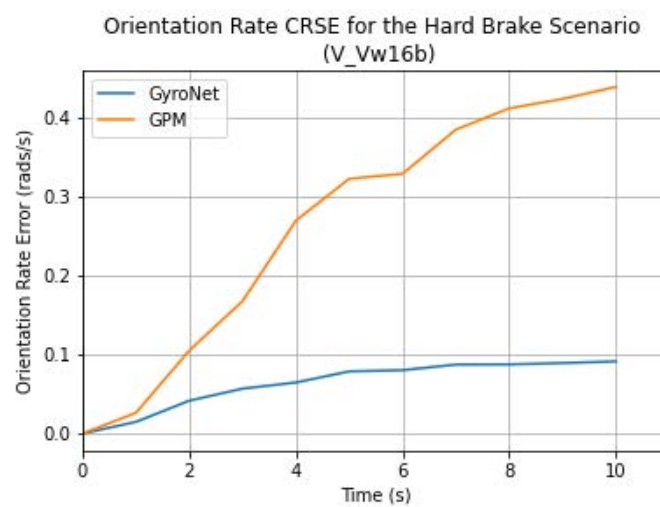


Figure 4.18. Sample evolution of the estimation error over time in the hard brake scenario based on the Orientation rate CRSE

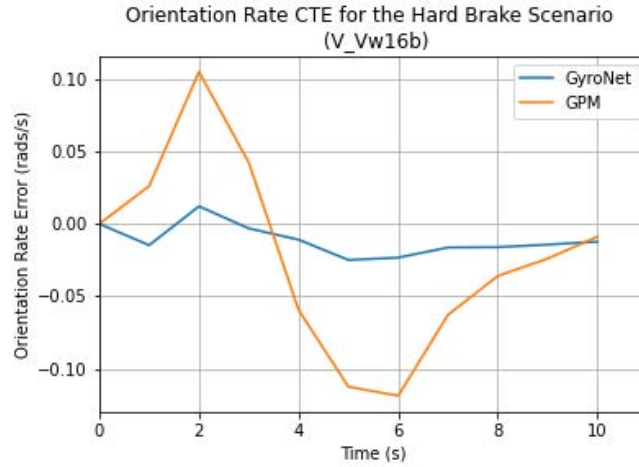


Figure 4.19. Sample evolution of the estimation error over time in the hard brake scenario based on the Orientation rate CTE.

4.2.5. Sharp Cornering and Successive Left–Right Turns Scenario

The sharp cornering and successive right–left turn scenario appears to be one of the most challenging for the inertial physics models on the CTE and CRSE metric (see Figures 4.22–4.25). This scenario investigation involves analysis on 43 test sequences over a maximum travel distance of approximately 115m. Reporting on the results presented in Table 4.13–4.15, across all three datasets, it can be observed that the APM obtained a maximum positional CRSE and CTE of 92.06m and 92.06m respectively, comparatively, the CRSE of the AccNet is 12.71m and the CTE is 8.49m. The WPM also obtained a CRSE and CTE of 5.08m and 8.19m respectively, compared to the WhONet which obtained a CRSE and CTE of 0.50m and 0.61m respectively. On the orientation rate, the GyroNet performs significantly better than the GPM with a maximum CRSE and CTE of 0.41rad/s and 0.13rad/s against the GPM’s performance of 4.29rad/s and 3.47rad/s. These results further highlight the capability of the deep learning models to significantly improve vehicular localisation during GPS outages with their reliability assured by their relatively low standard deviation. Like in other scenarios analysed, the WhONet outperforms the AccNet by up to 99% and continuously proves to be a robust, accurate and reliable option compared to the AccNet. An example trajectory of the vehicle during the sharp cornering and successive left and right turn is shown in Figure 4.11b.

Table 4.13. The performance of AccNet and APM on the sharp cornering and successive left and right turns scenario.

IO-VNB Dataset	Performance Metrics	Position Estimation Error (m)				Total Distance Travelled (m)	Number of Test Sequences evaluated
		CTE		CRSE			
		AccNet	APM	AccNet	APM		
V_Vw6	Max	2.94	92.06	9.84	92.06	107	12
	Min	0.13	54.42	1.43	54.42	60	
	(μ)	1.23	75.61	5.05	75.61	86	
	(σ)	0.98	10.61	2.46	10.61	12	
V_Vw7	Max	7.62	60.54	12.71	60.54	115	15
	Min	0.10	2.02	2.72	5.20	16	
	(μ)	2.86	18.87	7.42	22.15	70	
	(σ)	2.06	17.77	2.85	16.01	25	
V_Vw8	Max	8.49	58.83	11.06	58.83	109	16
	Min	1.21	6.51	2.77	7.41	36	
	(μ)	4.24	26.55	7.41	29.28	73	
	(σ)	2.38	17.79	2.48	15.97	20	

Table 4.14. The performance of WhONet and WPM on the sharp cornering and successive left and right turns scenario.

IO-VNB Dataset	Performance Metrics	Position Estimation Error (m)				Total Distance Travelled (m)	Number of Test Sequences evaluated
		CTE		CRSE			
		WhONet	WPM	WhONet	WPM		
V_Vw6	Max	0.35	3.68	0.57	5.00	107	12
	Min	0.00	0.09	0.11	0.73	60	
	(μ)	0.14	0.97	0.36	2.75	86	
	(σ)	0.11	1.15	0.09	1.42	12	
V_Vw7	Max	0.50	5.08	0.61	6.90	115	15

V_Vw8	Min	0.00	0.03	0.08	1.50	16	16
	(μ)	0.21	2.06	0.36	3.87	70	
	(σ)	0.14	1.40	0.13	1.33	25	
	Max	0.46	4.05	0.57	8.19	109	
	Min	0.00	0.05	0.11	1.13	36	
	(μ)	0.17	1.36	0.37	4.09	73	
	(σ)	0.12	1.30	0.12	2.04	20	
	Max	0.46	4.05	0.57	8.19	109	

Table 4.15. The performance of GyroNet and GPM on the sharp cornering and successive left and right turns scenario.

IO-VNB Dataset	Performance Metrics	Orientation Rate Estimation Error (rad/s)				Total Distance Travelled (m)	Number of Test Sequences evaluated
		CTE		CRSE			
		GyroNet	GPM	GyroNet	GPM		
V_Vw6	Max	0.13	3.08	0.27	4.64	107	12
	Min	0.00	0.02	0.08	0.32	60	
	(μ)	0.05	1.02	0.16	1.59	86	
	(σ)	0.04	0.97	0.05	1.37	12	
V_Vw7	Max	0.09	3.99	0.53	4.10	115	15
	Min	0.00	0.03	0.07	0.41	16	
	(μ)	0.03	1.63	0.23	2.18	70	
	(σ)	0.03	1.24	0.12	1.18	25	
V_Vw8	Max	0.08	3.80	0.36	4.02	109	16
	Min	0.00	0.04	0.04	0.51	36	
	(μ)	0.03	1.62	0.18	1.97	73	
	(σ)	0.02	1.46	0.09	1.25	20	

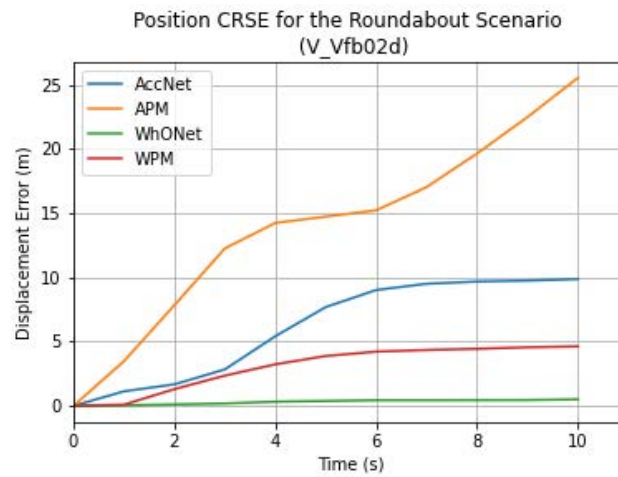


Figure 4.20. Sample evolution of the estimation error over time in the sharp cornering and successive left and right turns scenario based on the position CRSE

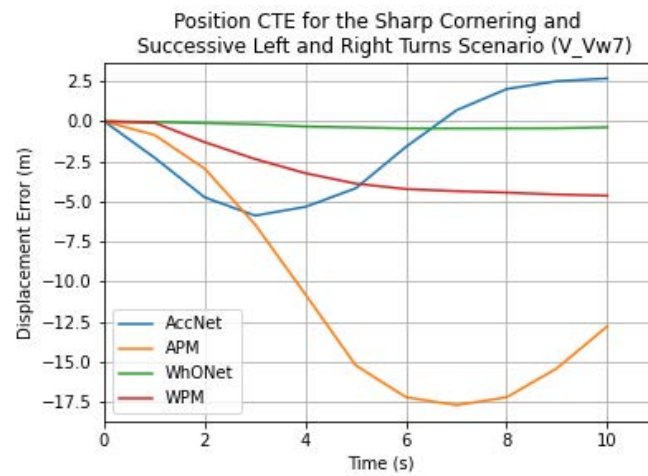


Figure 4.21. Sample evolution of the estimation error over time in the sharp cornering and successive left and right turns scenario based on the position CTE

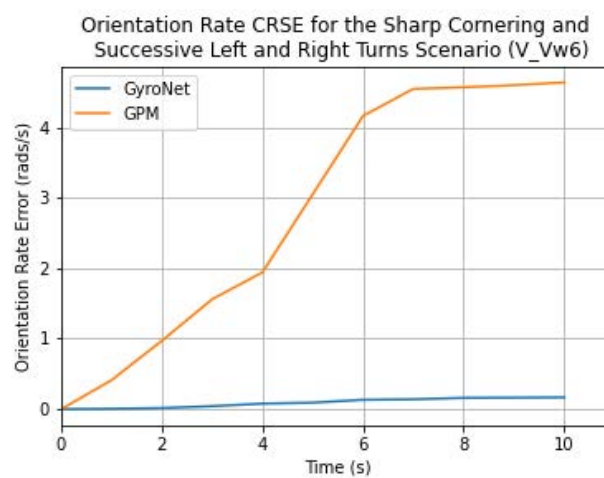


Figure 4.22. Sample evolution of the estimation error over time in the sharp cornering and successive left and right turns scenario based on the Orientation rate CRSE

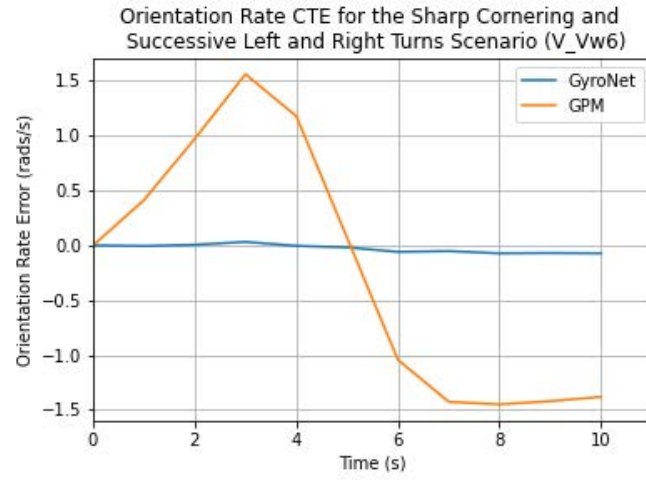


Figure 4.23. Sample evolution of the estimation error over time in the sharp cornering and successive left and right turns scenario based on the Orientation rate CTE.

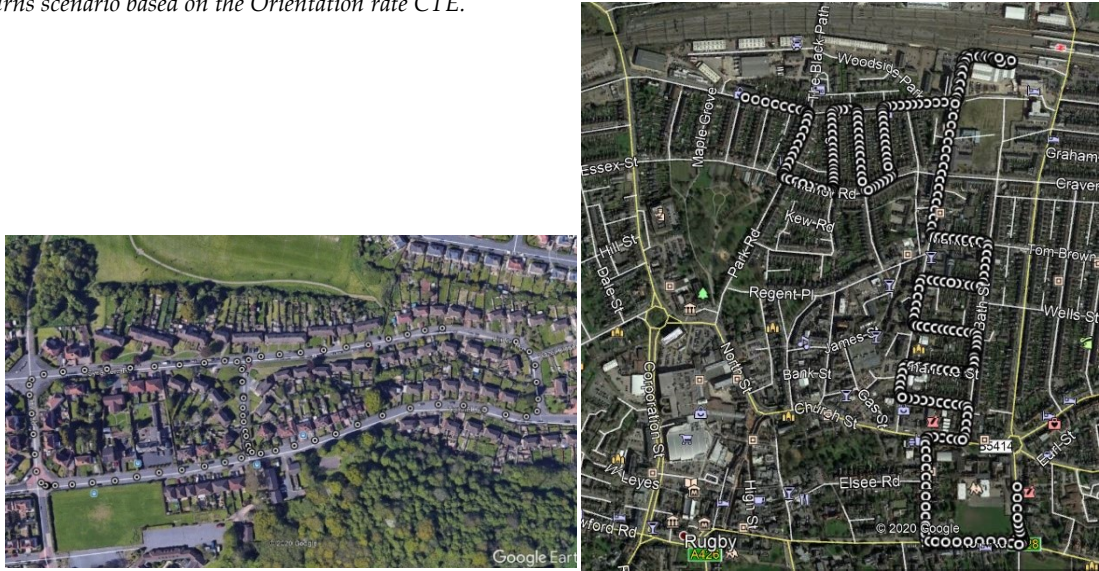


Figure 4.24. Trajectory of V-Vw8 sharp cornering and successive left and right turns data subset of the IO-VNBD.

4.2.6. Wet Road

Wet road conditions are one of the most critical driving scenarios that challenges an accurate tracking of wheeled vehicles due to wheel drifts, particularly on wet and muddy roads. However, the results presented on Table 4.16-4.18 show that the WhONet is able to capture the uncertainties caused by the wheel slippage. As reported on Table 4.16-4.18, it can be observed that the standard deviations of the error estimations of WhONet on datasets V_Vtb8 and V_Vtb11 are in the range of 0.01- 0.02 on both the CTE and CRSE metrics, making the WhONet a reliable method for tracking in such scenarios. On the max CRSE and CTE metric, the WhONet achieves a percentage error reduction of up to 94% and 97%, respectively, compared to that

obtained from the WPM. The WhONet also offers up to a 99% improvement on its position estimation counterpart, AccNet. On the orientation rate estimation, the GyroNet outperforms the GPM with a maximum CRSE of 0.25 rad/s compared to 2.59 rad/s. The wet road scenario was analysed over 22 test sequences, with a sample evolution of the error over time shown on Figures 4.25-4.28

Table 4.16. The performance of AccNet and APM on the wet road scenario.

IO-VNB Dataset	Performance Metrics	Position Estimation Error (m)				Total Distance Travelled (m)	Number of Test Sequences evaluated
		CTE		CRSE			
		AccNet	APM	AccNet	APM		
V_Vtb8	Max	2.31	18.42	3.47	18.42	202.8	6
	Min	0.06	3.43	1.62	4.20	180.4	
	(μ)	1.21	10.81	2.27	11.26	192.7	
	(σ)	0.81	6.09	0.66	5.82	8.4	
V_Vtb11	Max	0.87	8.66	3.68	8.66	199.7	4
	Min	0.30	2.72	1.96	4.42	191.3	
	(μ)	0.59	5.69	2.82	6.54	194.5	
	(σ)	0.28	2.97	0.86	2.12	3.4	
V_Vtb13	Max	5.44	41.00	9.37	41.00	114.9	12
	Min	0.17	4.11	3.18	10.42	46.3	
	(μ)	1.68	23.49	6.09	25.28	79.2	
	(σ)	1.45	13.86	2.22	11.80	24.2	

Table 4.17. The performance of WhONet and WPM on the wet road scenario.

IO-VNB Dataset	Performance Metrics	Position Estimation Error (m)				Total Distance Travelled (m)	Number of Test Sequences evaluated
		CTE		CRSE			
		WhONet	WPM	WhONet	WPM		
V_Vtb8	Max	0.07	2.21	0.19	2.21	202.8	6
	Min	0.00	0.02	0.08	1.28	180.4	

V_Vtb11	(μ)	0.03	1.17	0.14	1.66	192.7	4
	(σ)	0.02	0.69	0.02	0.39	8.4	
	Max	0.06	1.81	0.14	2.28	199.7	
	Min	0.00	0.55	0.05	1.03	191.3	
V_Vtb13	(μ)	0.04	1.07	0.11	1.63	194.5	12
	(σ)	0.01	0.46	0.02	0.49	3.4	
	Max	1.82	4.01	2.33	5.36	114.9	
	Min	0.00	0.03	0.06	1.85	46.3	
V_Vtb13	(μ)	0.59	1.28	0.75	3.53	79.2	12
	(σ)	0.39	1.22	0.49	1.17	24.2	
	Max	1.82	4.01	2.33	5.36	114.9	
	Min	0.00	0.03	0.06	1.85	46.3	

Table 4.18. The performance of GyroNet and GPM on the wet road scenario.

IO-VNB Dataset	Performance Metrics	Orientation Rate Estimation Error (rad/s)				Total Distance Travelled (m)	Number of Test Sequences evaluated
		CTE		CRSE			
		GyroNet	GPM	GyroNet	GPM		
V_Vw6	Max	0.02	0.04	0.09	0.12	202.8	6
	Min	0.00	0.00	0.02	0.05	180.4	
	(μ)	0.01	0.02	0.04	0.09	192.7	
	(σ)	0.00	0.01	0.02	0.03	8.4	
V_Vw7	Max	0.03	0.08	0.05	0.15	199.7	4
	Min	0.01	0.03	0.03	0.12	191.3	
	(μ)	0.02	0.06	0.04	0.14	194.5	
	(σ)	0.01	0.03	0.00	0.01	3.4	
V_Vw8	Max	0.03	2.59	0.25	2.59	114.9	12
	Min	0.00	0.00	0.05	0.09	46.3	
	(μ)	0.01	0.74	0.12	1.00	79.2	
	(σ)	0.01	0.81	0.06	0.81	24.2	

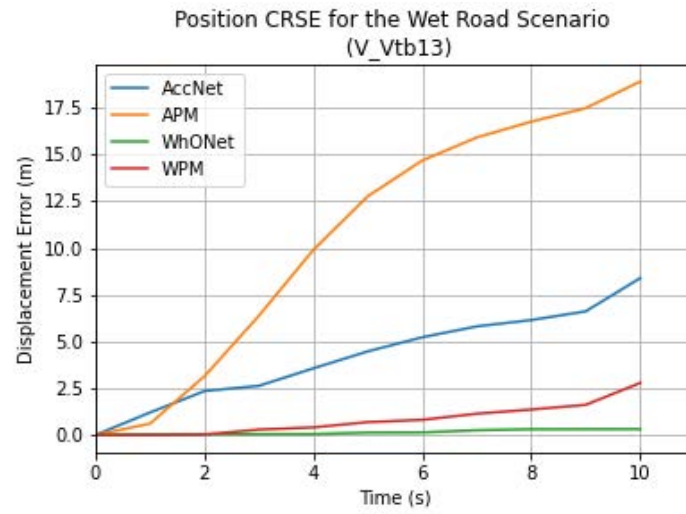


Figure 4.25. Sample evolution of the estimation error over time in the wet road scenario based on the position CRSE

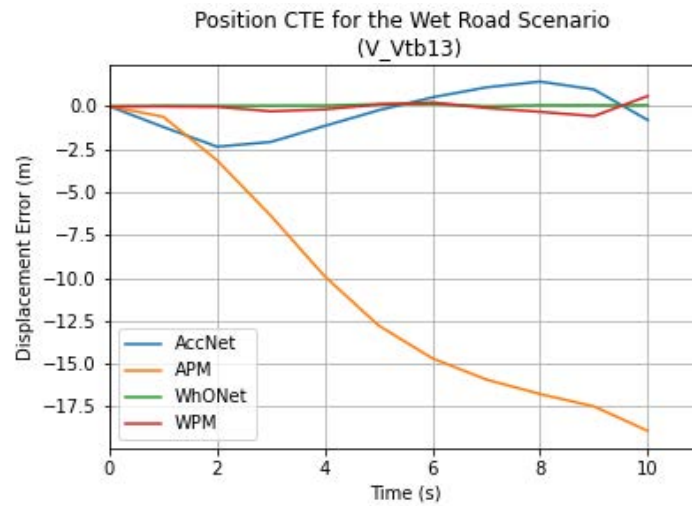


Figure 4.26. Sample evolution of the estimation error over time in the wet road scenario based on the position CTE

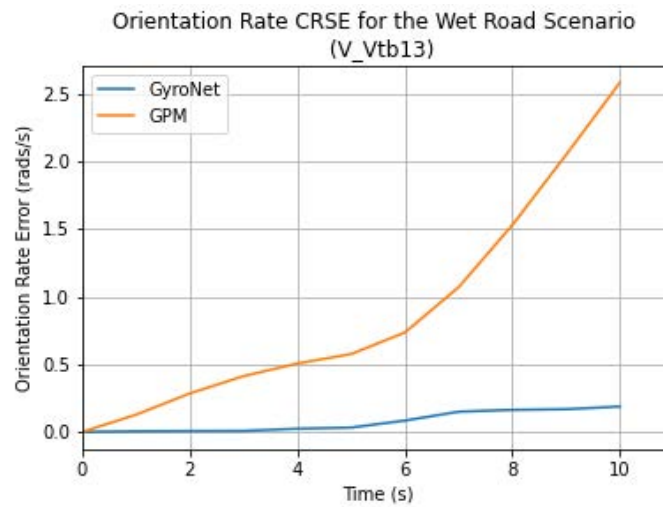


Figure 4.27. Sample evolution of the estimation error over time in the wet road scenario based on the Orientation rate CRSE

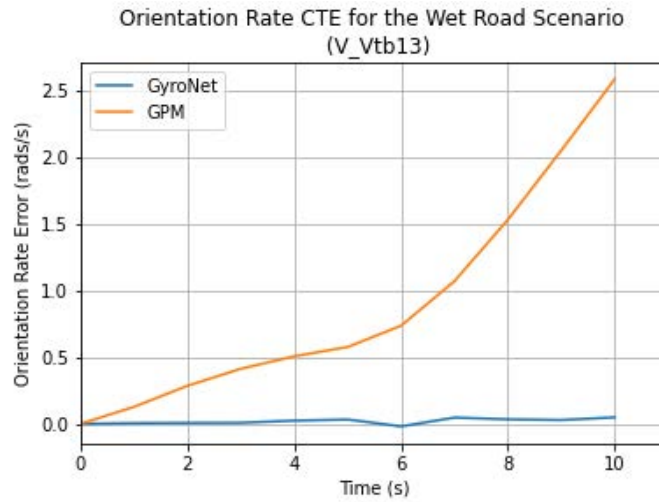


Figure 4.28. Sample evolution of the estimation error over time in the wet road scenario based on the Orientation rate CTE.

4.3. Summary

In this chapter, the deep learning models (WhONet, AccNet and GyroNet) and physics models (WPM, APM and GPM) described in Chapter 3, were evaluated on several complex scenarios; motorway, roundabout, hard brake, quick changes in acceleration, sharp cornering and successive left and right turns and wet road scenarios. Through a comparison using the performance metrics defined in chapter 3, we showed that the wheel encoder is a better sensor for position estimation in challenging driving scenarios. We further showed that the WhONet error estimation model is able to provide a more robust and accurate vehicle positioning compared to its counterpart AccNet. A comparison of the performance of the deep learning models compared to the physics model can be found in Figures 4.5 and 4.6.

Having established the superiority of the WhONet model for vehicular positioning in specific complex driving environments during short-term GNSS outages, we set out to investigate the performance of the WhONet in longer GNSS outages in the next chapter. The orientation estimation is not further analysed in the next chapter as orientation estimation in longer term GNSS outages is already an established field. For more details on this, readers can see (Brossard et al. 2020).

Chapter 5

Result and Analysis on Position Estimation in Longer Term GNSS Outages

Having established the superiority of the WhONet and wheel encoder based measurement for position estimation in the previous chapter, the robustness, accuracy and reliability of WhONet (a NN model) is for the first time evaluated over longer term GNSS outages (defined as up to 180 s) in this chapter. We however, focus on position estimation only as orientation estimation in longer term outages is a well-established research area with state-of-the-art performances such as found in (Brossard et al., 2020).

The problem of vehicular localisation in longer term GNSS outages (defined as outages up to 180 seconds) is particularly important for navigation in tunnels and valleys but also finds relevance in other GNSS outage scenarios such as navigation under bridges, through dense tree canopies, urban canyons, etc. The longer term GNSS outage scenarios studied are characterised by a mixture of complex scenarios as discussed in the previous chapter, and more scenarios as can be found in everyday driving. To assess the relevance of WhONet for vehicular positioning in everyday navigation in longer term GNSS absence, its performance is evaluated over a total distance of 493 km in assumed GNSS outages of 30s, 60 s, 120 s and 180 s using the IO-VNBD and CUPAC datasets as described in Chapter 3.

5.1 Performance Evaluation on the Longer term GNSS outages

5.1.1 30s GNSS Outage Scenario

In this section, the result from the 30s GNSS outage experiment using the IO-VNBD and CUPAC datasets are discussed.

5.1.1.1 IO-VNB Dataset

In the 30 seconds GNSS outage scenario, WhONet provides an error reduction on the WPM's estimation by up to 92%. As presented on Tables 5.1, the WhONet achieves the best average CTE and CRSE of 0.23 m and 0.67 m compared to 0.84 m and 2.31 m of the WPM over a max distance per test sequence of 987 m of all 688 sequences evaluated on the IO-VNB dataset (see Table 3.17). Moreover, on the maximum metric, the WhONet achieves the best CTE and CRSE of 0.72 m and 1.35 m respectively while the WPM achieves the best CTE and CRSE of 5.75 m and 8.37 m respectively.

The robustness of the WhONet is further emphasised by the low standard deviation of 0.18 obtained compared to 1.14 of the WPM as reported by Table 5.1. The result so obtained shows that the WhONet is able to significantly improve the accuracy of wheel odometry in the 30s outage scenario as shown in Figures 5.1 and 5.2. The evolution of the WhONet and WPM error estimations over time on both the CTE and CRSE metric is illustrated on Figures 5.3.

5.1.1.2 CUPAC Dataset

On the CUPAC dataset (see Table 3.18), the WhONet also obtains the best average CTE and CRSE of 0.34 m and 0.94 m compared to 1.88 m and 7.13 m of the WPM over a max distance per test sequence of 629 m of all 121 sequences evaluated, as shown on Table 5.2. As well, on the maximum metric, the WhONet obtains the best CTE and CRSE of 0.84 m and 1.42 m respectively in comparison to 5.45 m and 11.08 m of the WPM as clearly seen on Table 5.2.

The robustness of the WhONet is further accentuated by the low standard deviation of 0.24 obtained compared to 1.48 of the WPM as seen on Table 5.2. The result obtained shows that the WhONet is able to greatly enhance the accuracy of WPM in the 30s outage scenario as shown in Figures 5.1 and 5.2.

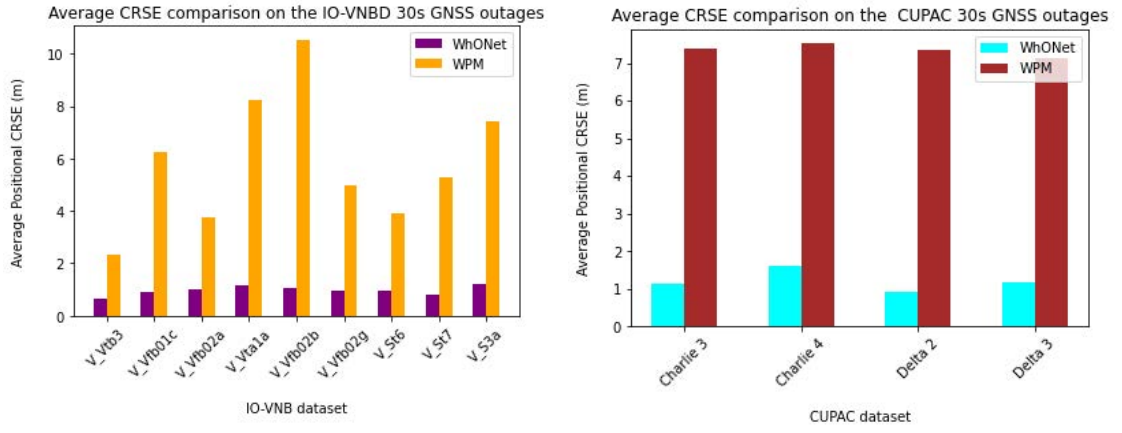


Figure 5.1 Comparison of the average positional CRSE on the IO-VNB and CUPAC dataset during the 30s GNSS signal outage experiment

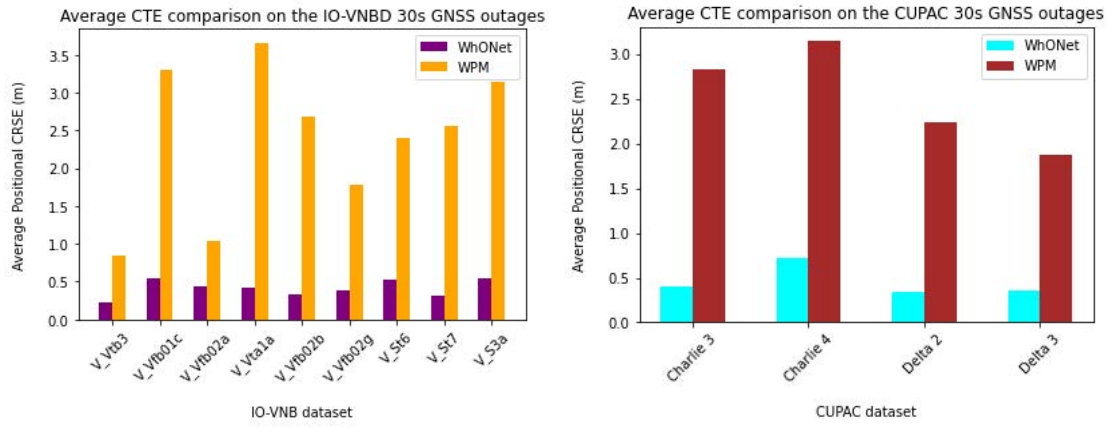


Figure 5.2 Comparison of the average positional CTE on the IO-VNB and CUPAC dataset during the 30s GNSS signal outage experiment

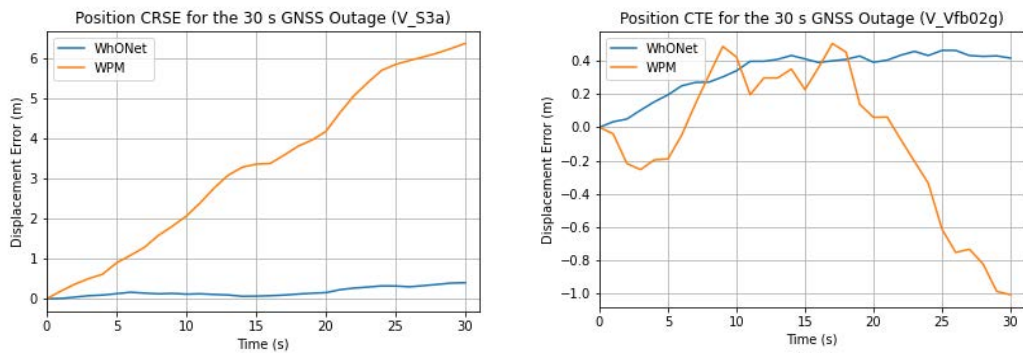


Figure 5.3. Sample evolution of the estimation error over time in the 30 s GNSS outage scenario based on the position CRSE and CTE

Table 5.1 The 30 seconds GNSS outage experiment results on the IO-VNB dataset

IO-VNB		Position Estimation Error (m)		Total	Number of Test
Dataset	Performance	CTE	CRSE		

Metrics		WPM	WhONet	WPM	WhONet	Distance Travelled	Sequences evaluated
V_Vtb3	Max	5.75	0.72	8.37	1.35	222	27
	Min	0.03	0.00	0.44	0.11	0	
	(μ)	0.84	0.23	2.31	0.67	24	
	(σ)	1.14	0.18	1.63	0.20	46	
V_Vfb01c	Max	9.62	1.38	17.73	2.41	830	21
	Min	0.20	0.00	2.19	0.22	50	
	(μ)	3.30	0.55	6.27	0.90	507	
	(σ)	2.46	0.40	3.36	0.43	259	
V_Vfb02a	Max	8.89	2.71	18.25	8.57	961	119
	Min	0.02	0.00	1.72	0.28	11	
	(μ)	1.04	0.43	3.73	1.01	807	
	(σ)	1.18	0.43	2.13	0.83	156	
V_Vta1a	Max	14.29	2.00	19.22	3.66	768	86
	Min	0.12	0.00	1.87	0.43	9	
	(μ)	3.66	0.42	8.24	1.15	473	
	(σ)	2.76	0.47	3.72	0.63	144	
V_Vfb02b	Max	11.60	0.88	17.04	1.70	570	36
	Min	0.12	0.00	4.46	0.37	47	
	(μ)	2.68	0.33	10.54	1.04	207	
	(σ)	2.73	0.23	2.94	0.30	109	
V_Vfb02g	Max	11.69	1.87	12.84	3.94	947	90
	Min	0.08	0.00	2.17	0.34	206	
	(μ)	1.78	0.38	4.97	0.94	706	
	(σ)	1.81	0.38	2.03	0.47	174	
V_St6	Max	11.67	1.92	14.14	2.46	987	171
	Min	0.00	0.00	0.82	0.21	7	
	(μ)	2.40	0.52	3.89	0.93	664	
	(σ)	1.81	0.44	2.24	0.42	269	
V_St7	Max	8.71	1.09	12.85	1.90	713	56
	Min	0.01	0.00	0.54	0.24	1	
	(μ)	2.56	0.31	5.28	0.80	337	
	(σ)	2.11	0.26	2.87	0.43	218	
V_S3a	Max	9.37	3.03	18.89	4.19	770	82
	Min	0.03	0.00	0.98	0.22	1	
	(μ)	3.14	0.55	7.44	1.22	316	
	(σ)	2.00	0.62	3.69	0.65	166	

Table 5.2. The 30 seconds GNSS outage experiment results on the CUPAC dataset

CUPAC Dataset	Performance Metrics	Position Estimation Error (m)				Total Distance Travelled	Number of Test Sequences evaluated
		CTE		CRSE			
		WPM	WhONet	WPM	WhONet		
Charlie 3	Max	10.50	2.34	14.52	5.36	629	45
	Min	0.02	0.00	2.44	0.37	113	
	(μ)	2.83	0.40	7.39	1.14	309	
	(σ)	2.56	0.48	2.75	0.73	151	
Charlie 4	Max	7.68	5.16	17.47	8.53	441	22
	Min	0.41	0.00	2.77	0.41	30	
	(μ)	3.15	0.72	7.52	1.62	218	
	(σ)	1.93	1.02	3.11	1.69	97	
Delta 2	Max	5.45	0.84	11.08	1.42	246	16
	Min	0.34	0.00	4.35	0.51	19	
	(μ)	2.24	0.34	7.35	0.94	188	
	(σ)	1.55	0.24	2.08	0.24	64	
Delta 3	Max	6.81	1.29	13.26	5.07	358	38
	Min	0.00	0.00	2.54	0.43	6	
	(μ)	1.88	0.36	7.13	1.18	130	
	(σ)	1.48	0.31	2.29	0.72	90	

5.1.2 60s GNSS Outage Scenario

In this section, the result from the 60s GNSS outage experiment using the IO-VNBD and CUPAC datasets are discussed.

5.1.2.1 IO-VNB Dataset

Table 5.3 reports the result from the 60 seconds GNSS outage experiment on the IO-VNBD. On the CTE and CRSE metric, the WhONet provides the best average of 0.30 m and 1.31 m compared to 1.02 m and 4.56 m of the WPM over a max test sequence distance covered of 1960 m across all 342 sequences evaluated on the IO-VNBD (see Table 3.17). Also, on the maximum metric, the WhONet obtains the best CTE of 0.62 m and CRSE of 2.29 m in contrast to the WPM best CTE and CRSE of 2.53 m and 14.51 m.

The consistency of the WhONet is highlighted by the low standard deviation of 0.16 obtained compared to 0.68 of the WPM as reported by Table 5.3. The result so

obtained shows that the WhONet is able to enhance the accuracy of WPM in the 60s outage scenario as shown in Figures 5.4 and 5.5. The evolution of the WhONet and WPM error estimations over time on both the CTE and CRSE metric is illustrated on Figures 5.6.

5.1.2.2 CUPAC Dataset

The performance evaluation on the CUPAC dataset, as presented on Table 5.4, reveals the best average of 0.49 m and 1.88 m compared to 2.53 m and 14.25 m of the WPM over 57 test sequences evaluated with a max displacement of 1238 m per sequence. Overall, the results show the WhONet is able to provide an error reduction of up to 91% on the WPM's estimation in the 60s outage scenario as illustrated in Figures 5.4 and 5.5. Moreover, for the maximum metric, the WhONet achieves the best CTE and CRSE of 0.96 m and 2.48 m respectively while for the WPM, we have the best CTE of 6.13 m and CRSE of 19.22 m.

The dependability of the WhONet is further proven by the low standard deviation of 0.21 obtained in comparison to 1.63 of the WPM as reported by both Table 5.4. The result so obtained shows that the WhONet is able to significantly improve the accuracy of WPM in the 60s outage scenario as shown in Figures 5.4 and 5.5. The evolution of the WhONet and WPM error estimations over time on both the CTE and CRSE metric is illustrated on Figures 5.6.

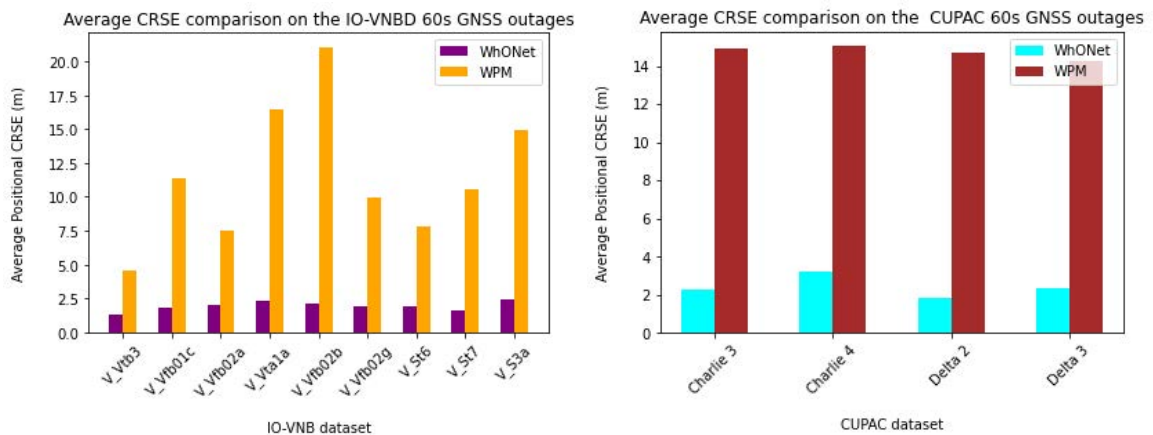


Figure 5.4. Comparison of the average positional CRSE on the IO-VNB and CUPAC dataset during the 60s GNSS signal outage experiment

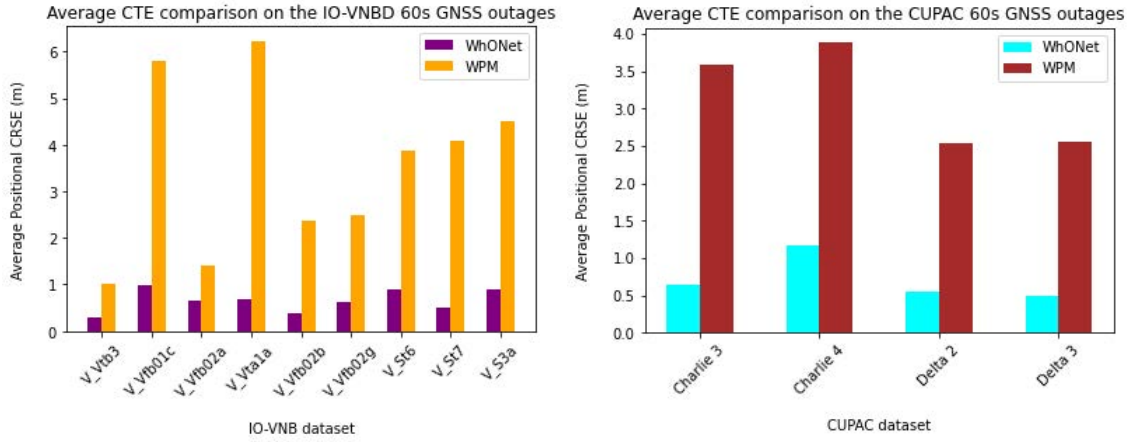


Figure 5.5. Comparison of the average positional CTE on the IO-VNB and CUPAC dataset during the 60s GNSS signal outage experiment

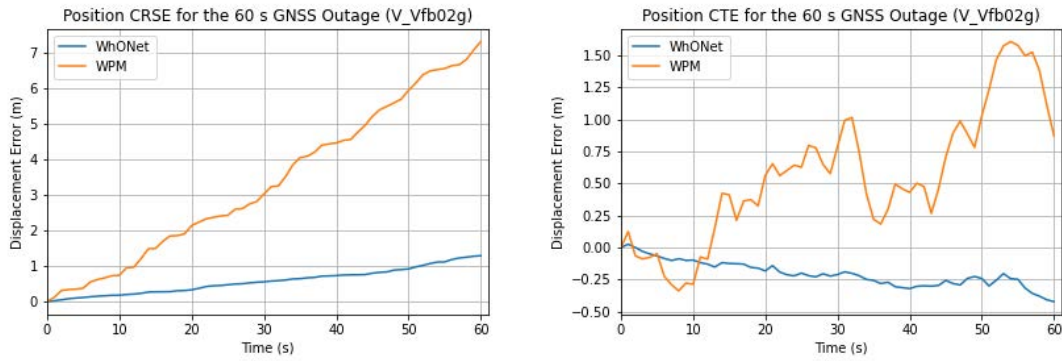


Figure 5.6. Sample evolution of the estimation error over time in the 60s GNSS outage scenario based on the position CRSE and CTE

Table 5.3. The 60 seconds GNSS outage experiment results on the IO-VNB dataset

IO-VNB Dataset	Performance Metrics	Position Estimation Error (m)				Total Distance Travelled	Number of Test Sequences evaluated
		CTE		CRSE			
		WPM	WhONet	WPM	WhONet		
V_Vtb3	Max	2.53	0.62	15.04	2.29	358	13
	Min	0.03	0.00	0.95	0.29	1	
	(μ)	1.02	0.30	4.56	1.31	50	
	(σ)	0.68	0.16	3.22	0.25	90	
V_Vfb01c	Max	9.95	2.38	14.51	3.73	1557	10
	Min	0.15	0.00	5.97	0.58	149	
	(μ)	5.79	0.98	11.40	1.77	1042	
	(σ)	3.59	0.69	2.53	0.73	500	

V_Vfb02a	Max	8.68	2.43	31.34	9.62	1883	59
	Min	0.01	0.00	4.56	0.87	45	
	(μ)	1.42	0.66	7.48	2.02	1615	
	(σ)	1.63	0.56	3.81	1.11	310	
V_Vta1a	Max	17.45	3.02	30.94	6.27	1446	43
	Min	0.47	0.00	7.69	1.06	217	
	(μ)	6.23	0.67	16.47	2.29	947	
	(σ)	3.66	0.73	5.83	1.07	250	
V_Vfb02b	Max	7.73	0.96	30.67	2.94	1052	18
	Min	0.01	0.00	11.94	1.10	213	
	(μ)	2.38	0.39	21.08	2.08	415	
	(σ)	2.18	0.24	4.91	0.48	187	
V_Vfb02g	Max	7.94	2.16	22.41	4.42	1864	45
	Min	0.05	0.00	5.04	0.77	730	
	(μ)	2.49	0.62	9.95	1.88	1411	
	(σ)	2.22	0.54	3.72	0.65	334	
V_St6	Max	11.88	3.30	26.03	4.32	1960	85
	Min	0.13	0.00	2.78	0.76	81	
	(μ)	3.88	0.90	7.77	1.86	1336	
	(σ)	2.24	0.73	4.05	0.71	522	
V_St7	Max	12.44	1.31	21.99	3.57	1393	28
	Min	0.15	0.00	1.57	0.59	2	
	(μ)	4.08	0.50	10.56	1.61	674	
	(σ)	3.13	0.32	5.04	0.75	420	
V_S3a	Max	12.73	4.44	30.88	5.63	1514	41
	Min	0.08	0.00	3.37	0.83	8	
	(μ)	4.50	0.88	14.89	2.43	632	
	(σ)	2.76	0.96	6.33	0.90	304	

Table 5.4. The 60 seconds GNSS outage experiment results on the CUPAC dataset

CUPAC Dataset	Performance Metrics	Position Estimation Error (m)				Total Distance Travelled	Number of Test Sequences evaluated
		CTE		CRSE			
		WPM	WhONet	WPM	WhONet		
Charlie 3	Max	10.04	2.10	22.81	6.42	1238	22
	Min	0.29	0.00	5.88	1.06	280	
	(μ)	3.58	0.64	14.90	2.28	622	
	(σ)	2.46	0.57	4.74	1.01	295	
Charlie	Max	8.52	3.87	23.03	9.59	669	11

4	Min	0.13	0.00	10.28	1.01	169	
	(μ)	3.88	1.17	15.04	3.23	435	
	(σ)	2.71	1.02	3.42	2.64	145	
Delta 2	Max	6.24	0.96	19.22	2.48	481	8
	Min	0.37	0.00	10.51	1.25	153	
	(μ)	2.53	0.56	14.70	1.88	376	
Delta 3	(σ)	1.63	0.21	3.07	0.39	100	16
	Max	6.13	1.53	20.40	5.99	625	
	Min	0.12	0.00	8.75	1.51	23	
Delta 3	(μ)	2.56	0.49	14.25	2.36	261	
	(σ)	1.77	0.45	2.84	0.97	165	

5.1.3 120s GNSS Outage Scenario

In this section, the result from the 120s GNSS outage experiment using the IO-VNBD and CUPAC datasets are discussed.

5.1.3.1 IO-VNB Dataset

The WhONet outperforms the WPM providing up to a 91% error reduction on the 120 seconds GNSS outage scenario as illustrated in Figures 5.7 and 5.8. When evaluated on the IO-VNBD, as shown on Table 5.5, the WhONet achieves the best average CTE and CRSE of 0.34 m and 2.62 m compared to 1.78 m and 9.11 m respectively of the WPM over a max distance per test sequence of 3.9 km of all 168 sequences. In addition, on the maximum metric, the WhONet has the best CTE and CRSE of 0.63 m and 4.01 m while WPM has 2.67 m and 15.99 m CTE and CRSE respectively.

The robustness of the WhONet is further emphasised by the low standard deviation of 0.19 obtained in comparison to 0.66 of the WPM as reported on Tables 5.5. The result so obtained shows that the WhONet is able to improve the accuracy of WPM in the 120s outage scenario.

5.1.3.2 CUPAC Dataset

On the CUPAC dataset (see table 3.18), the WhONet also obtains the best average CTE and CRSE of 0.46 m and 3.75 m compared to 3.73 m and 28.49 m of the WPM over a max distance per test sequence of 2.3 km out of all 29 sequences evaluated as shown on Table 5.6. As well, on the maximum metric, the WhONet achieves the best CTE and CRSE of 0.85 m and 4.68 m respectively, on the other hand WPM achieves the best CTE AND CRSE of 7.93 m and 36.18 m.

The validity of the WhONet is again obvious as we obtained a low standard deviation of 0.06 compared to 2.07 of the WPM as reported in Table 5.6. The result so obtained shows that the WhONet is able to significantly improve the accuracy of wheel odometry in the 120s outage scenario as shown in Figures 5.7 and 5.8. The evolution of the WhONet and WPM error estimations over time on both the CTE and CRSE metric is illustrated on Figures 5.9.

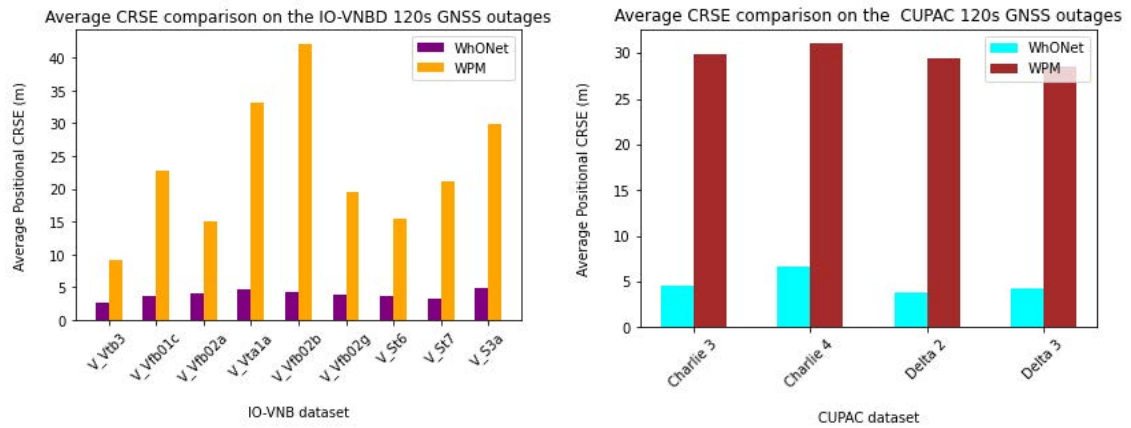


Figure 5.7. Comparison of the average positional CRSE on the IO-VNB and CUPAC dataset during the 120s GNSS signal outage experiment

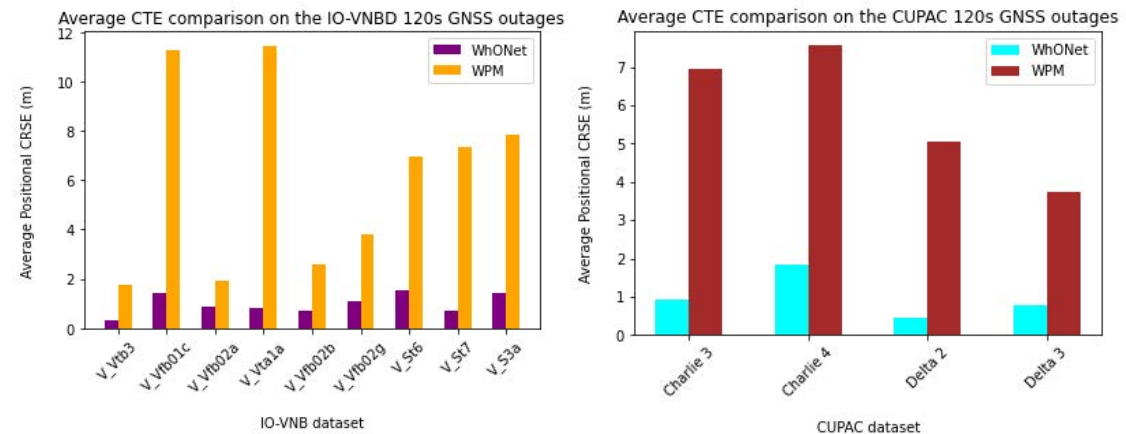


Figure 5.8. Comparison of the average positional CTE on the IO-VNB and CUPAC dataset during the 120s GNSS signal outage experiment

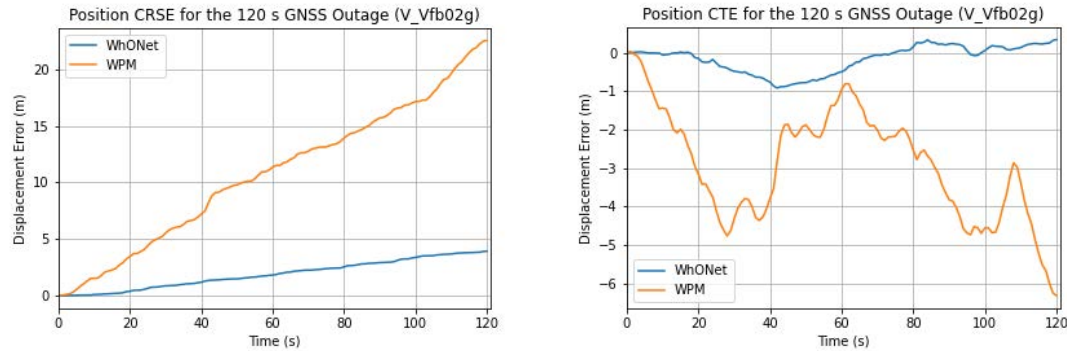


Figure 5.9. Sample evolution of the estimation error over time in the 120s GNSS outage scenario based on the position CRSE and CTE

Table 5.5. The 120 seconds GNSS outage experiment results on the IO-VNB dataset

IO-VNB Dataset	Performance Metrics	Position Estimation Error (m)				Total Distance Travelled	Number of Test Sequences evaluated
		CTE		CRSE			
		WPM	WhONet	WPM	WhONet		
V_Vtb3	Max	2.67	0.63	15.99	4.01	359	6
	Min	0.61	0.01	6.74	1.75	25	
	(μ)	1.78	0.30	9.11	2.62	102	
	(σ)	0.66	0.21	3.21	0.19	117	
V_Vfb01c	Max	19.55	3.18	27.18	5.05	3058	5
	Min	3.54	0.01	19.23	1.95	543	
	(μ)	11.26	1.41	22.80	3.54	2083	
	(σ)	5.13	0.90	3.42	0.67	888	
V_Vfb02a	Max	9.79	2.24	46.50	11.75	3671	29
	Min	0.10	0.00	9.91	2.05	683	
	(μ)	1.90	0.89	15.04	4.07	3234	
	(σ)	2.13	0.63	6.66	1.41	577	
V_Vta1a	Max	19.61	1.99	51.34	10.35	2579	21
	Min	1.26	0.00	20.26	2.64	785	
	(μ)	11.46	0.79	33.06	4.62	1893	
	(σ)	4.59	0.56	9.53	1.81	430	
V_Vfb02b	Max	7.42	1.26	56.24	5.76	1489	9
	Min	0.44	0.00	27.49	2.52	514	

	(μ)	2.59	0.68	42.17	4.15	830	
	(σ)	2.33	0.34	8.66	0.88	288	
V_Vfb02g	Max	8.55	2.53	34.39	5.66	3716	22
	Min	0.00	0.00	11.34	2.13	1707	
	(μ)	3.79	1.11	19.48	3.79	2852	
	(σ)	2.64	0.73	5.66	0.83	581	
V_St6	Max	14.95	5.13	35.61	6.39	3870	42
	Min	0.75	0.00	7.49	1.63	256	
	(μ)	6.97	1.52	15.44	3.69	2700	
	(σ)	3.52	1.31	7.01	1.07	977	
V_St7	Max	18.22	1.73	36.17	6.49	2435	14
	Min	0.57	0.00	11.75	1.43	216	
	(μ)	7.35	0.68	21.13	3.21	1348	
	(σ)	4.69	0.45	7.34	1.23	784	
V_S3a	Max	15.22	4.81	51.50	8.07	2623	20
	Min	0.94	0.00	13.18	2.37	422	
	(μ)	7.84	1.43	29.89	4.82	1269	
	(σ)	3.97	1.31	10.24	1.26	558	

Table 5.6. The 120 seconds GNSS outage experiment results on the CUPAC dataset

CUPAC Dataset	Performance Metrics	Position Estimation Error (m)				Total Distance Travelled	Number of Test Sequences evaluated
		CTE		CRSE			
		WPM	WhONet	WPM	WhONet		
Charlie 3	Max	17.82	2.27	36.18	9.40	2339	11
	Min	2.05	0.00	14.78	2.27	681	
	(μ)	6.95	0.92	29.80	4.57	1245	
	(σ)	4.34	0.58	5.94	1.61	510	
Charlie 4	Max	9.18	2.91	37.42	12.10	1229	5
	Min	3.50	0.00	25.21	2.60	612	
	(μ)	7.56	1.83	31.02	6.65	923	
	(σ)	2.07	0.52	4.13	3.71	214	
Delta 2	Max	8.54	0.85	37.15	4.68	850	4
	Min	1.95	0.00	26.23	2.70	634	
	(μ)	5.06	0.46	29.41	3.75	752	
	(σ)	2.47	0.06	4.49	0.45	78	
Delta 3	Max	7.93	2.10	37.73	5.74	990	9
	Min	0.29	0.00	22.02	3.15	173	
	(μ)	3.73	0.77	28.49	4.30	481	

(σ)	2.27	0.49	4.56	0.66	263
------------	------	------	------	------	-----

5.1.4 180s GNSS Outage Scenario

In this section, the result from the 180s GNSS outage experiment using the IO-VNBD and CUPAC datasets are discussed.

5.1.4.1 IO-VNB Dataset

In the 180 seconds GNSS outage scenario, WhONet provides an error reduction on the WPM's estimation by up to 90%. As presented on Table 5.7, the WhONet achieves the best average CTE and CRSE of 0.26 m and 3.93 m compared to 2.28 m and 13.67 m of WPM over a max distance per test sequence of 5.6 km of all 111 sequences evaluated on the IO-VNB dataset (see Table 3.17). Furthermore, on the maximum metric, the WhONet achieves the best CTE and CRSE of 0.38 m and 4.97 m and comparing that to the WPM's best CTE and CRSE of 4.26 m and 18.29 m.

The reliability of the WhONet is better accentuated by the low standard deviation of 0.01 obtained, compared to 1.25 of the WPM as reported by Table 5.7. The result so obtained shows that the WhONet is able to significantly improve the accuracy of wheel odometry in the 180s outage scenario as seen in Figures 5.10 and 5.11. The evolution of the WhONet and WPM error estimations over time on both the CTE and CRSE metric is illustrated on Figure 5.12.

5.1.4.2 CUPAC Dataset

On the CUPAC dataset (see Table 3.18), the WhONet also obtains the best average CTE and CRSE of 0.51 m and 5.13 m compared to 4.59 m and 42.74 m of the WPM over a max distance per test sequence of 3.4 km of all 18 sequences evaluated as shown on Table 5.8. Moreover, on the maximum metric, the WhONet achieves the best CTE and CRSE of 0.57 m and 5.15 m respectively in comparison to WPM's CTE of 10.17 m and CRSE of 50.38 m.

The robustness of the WhONet is further emphasised by the low standard deviation of 0 on the Delta 2 dataset obtained compared to 2.69 of the WPM as reported in Tables 5.8. The result obtained shows that the proposed model is able to significantly improve the performance of wheel odometry in the 180s outage scenario.

The WhONet's improvement over the WPM on each dataset evaluated on the average CTE and CRSE is presented on Figures 5.10, 5.11 and 5.12. Figure 5.13 shows a sample trajectory of the vehicle during the longer-term outage scenario.

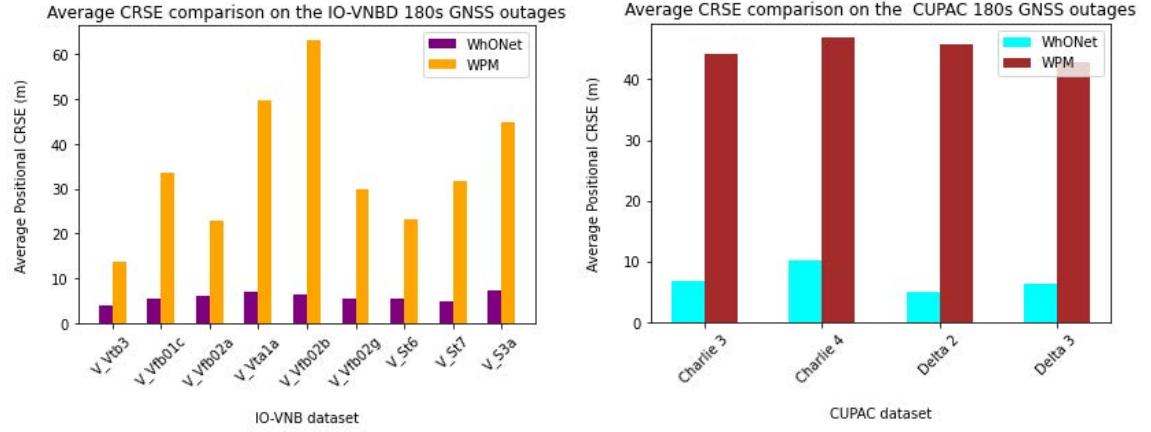


Figure 5.10. Comparison of the average positional CRSE on the IO-VNB and CUPAC dataset during the 180s GNSS signal outage experiment

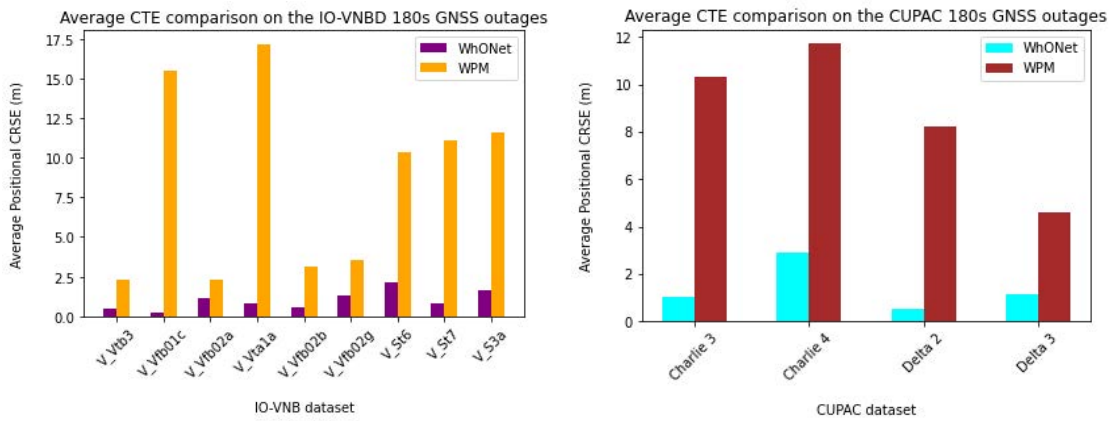


Figure 5.11. Comparison of the average positional CTE on the IO-VNB and CUPAC dataset during the 180s GNSS signal outage experiment

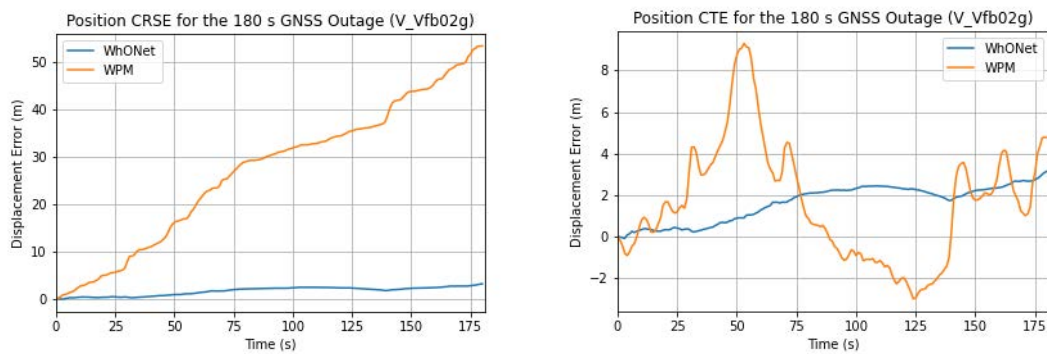


Figure 5.12. Sample evolution of the estimation error over time in the 180 s GNSS outage scenario based on the position CRSE and CTE

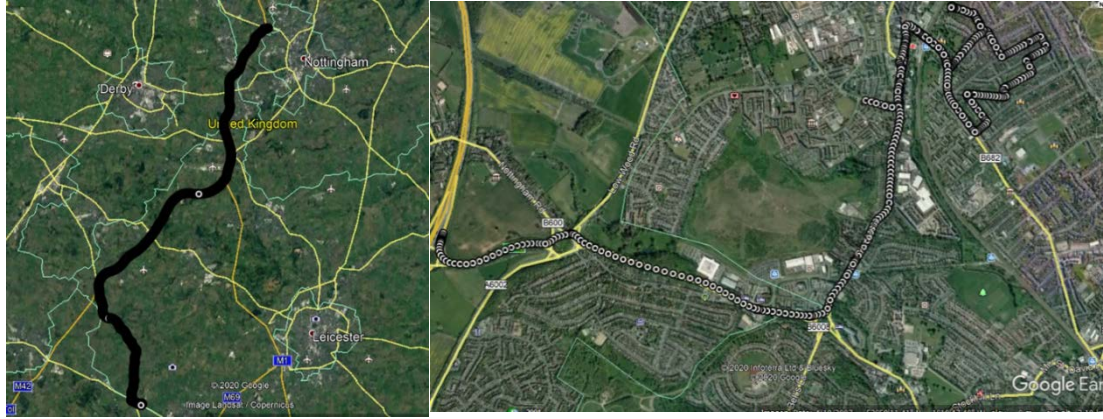


Figure 5.13. The vehicle trajectory on the V-Vfb02g dataset (left) and V-Vfb02b dataset (right) used in evaluating WhONet's performance during the 30s, 60s, 120s and 180s GNSS outage experiment.

Table 5.7. The results from the 180 seconds GNSS outage experiment results on the IO-VNB dataset

IO-VNB Dataset	Performance Metrics	Position Estimation Error (m)				Total Distance Travelled	Number of Test Sequences evaluated
		CTE		CRSE			
		WPM	WhONet	WPM	WhONet		
V_Vtb3	Max	4.26	1.02	18.29	4.97	369	4
	Min	0.85	0.01	10.32	2.81	46	
	(μ)	2.30	0.49	13.67	3.93	153	
	(σ)	1.25	0.18	2.89	0.21	127	
V_Vfb01c	Max	21.97	0.38	36.12	7.42	4407	3
	Min	3.39	0.00	31.92	3.97	1835	
	(μ)	15.53	0.26	33.57	5.43	3340	
	(σ)	8.59	0.01	1.82	0.66	1095	
V_Vfb02a	Max	12.63	3.02	52.18	13.02	5447	19
	Min	0.03	0.00	15.67	3.67	1102	
	(μ)	2.28	1.17	22.72	6.08	4858	
	(σ)	3.02	0.85	8.21	1.55	915	
V_Vta1a	Max	27.18	1.68	73.89	14.19	3692	14
	Min	10.71	0.00	31.29	4.20	1173	
	(μ)	17.19	0.79	49.59	6.93	2840	
	(σ)	4.41	0.48	10.84	2.42	661	
V_Vfb02b	Max	5.63	1.10	75.46	8.09	1910	6
	Min	0.90	0.00	55.23	4.04	890	

V_Vfb02g	(μ)	3.17	0.56	63.25	6.23	1244	15
	(σ)	1.81	0.38	8.01	0.77	361	
	Max	9.28	2.53	53.40	8.33	5251	
	Min	0.09	0.00	18.65	3.48	2474	
	(μ)	3.55	1.27	29.84	5.65	4234	
	(σ)	2.57	0.76	9.48	0.89	916	
V_St6	Max	21.86	6.67	41.30	8.62	5626	28
	Min	0.62	0.00	11.42	2.61	513	
	(μ)	10.37	2.14	23.16	5.53	4050	
	(σ)	5.25	1.64	9.46	1.24	1412	
V_St7	Max	19.09	1.67	54.62	9.47	3570	9
	Min	0.23	0.00	19.00	2.54	610	
	(μ)	11.10	0.84	31.82	4.89	2000	
	(σ)	6.31	0.40	11.06	1.62	1083	
V_S3a	Max	26.28	4.62	64.02	11.14	3345	13
	Min	0.20	0.00	20.07	4.32	1086	
	(μ)	11.59	1.65	44.75	7.23	1906	
	(σ)	6.34	1.08	12.72	1.37	775	

Table 5.8. The 180 seconds GNSS outage experiment results on the CUPAC dataset

CUPAC Dataset	Performance Metrics	Position Estimation Error (m)				Total Distance Travelled	Number of Test Sequences evaluated
		CTE		CRSE			
		WPM	WhONet	WPM	WhONet		
Charlie 3	Max	17.10	1.50	52.56	11.04	3416	7
	Min	3.55	0.00	23.04	3.89	1134	
	(μ)	10.33	1.03	44.08	6.91	1899	
	(σ)	4.54	0.28	10.46	1.77	788	
Charlie 4	Max	15.11	4.34	55.23	20.79	1603	3
	Min	8.03	0.00	40.66	3.70	1171	
	(μ)	11.72	2.89	46.80	10.28	1422	
	(σ)	2.90	0.20	6.17	7.00	183	
Delta 2	Max	10.93	0.57	53.53	5.15	1214	2
	Min	5.56	0.00	37.87	5.06	1162	
	(μ)	8.24	0.51	45.70	5.13	1188	
	(σ)	2.69	0.01	7.83	0.00	26	
Delta 3	Max	10.17	2.10	50.38	7.55	1244	6
	Min	0.41	0.00	30.77	5.42	301	
	(μ)	4.59	1.18	42.74	6.45	721	

(σ)	3.42	0.16	7.22	0.54	346
------------	------	------	------	------	-----

5.2 Summary

In this chapter, the robustness and accuracy of the WhONet in consistently improving the Wheel encoder Physics Model (WPM) position estimation was demonstrated with up to a 93% reduction in the position error after 180 seconds of travel. With several analyses over four different GNSS outage scenarios using two different datasets, we have shown that the WhONet is able to provide an average accuracy of 8.62 m after 5.6 km of travel. As such, the WhONet, can be used to process the wheel encoder measurements to provide a more accurate and robust position estimation for autonomous vehicles in the long-term absence of GNSS signals.

As this chapter focuses on a model trained on a certain vehicle to be deployed on the same vehicle, the next chapter looks at the use of transfer learning to aid the generalization of the WhONet model to other vehicles or motion characteristics.

Chapter 6

New Vehicle Domain Adaptation of Vehicular Position Model using Transfer Learning.

Having established the performance of the WhONet model for position estimation in longer term GNSS outage, this chapter provides a novel framework called R-WhONet (Recalibrated Wheel Odometry neural Network) for the adaptation of the WhONet model to vehicles with different feature characteristics such as tyre pressures, worn out tyre state, driving behavior, size, etc. We for the first time study the ability of the R-WhONet model to accurately and robustly adapt the WhONet model to new vehicles and scenarios using transfer learning, by evaluating its performance on longer term GNSS outage scenarios using the CUPAC dataset (as it is characterised by a different vehicle dynamics). As such in this chapter, we discuss the motivations for model adaptations, mathematical definitions of transfer learning and other associated terms, R-WhONet's framework, as well as the results from R-WhONet's evaluation.

6.1. Motivation

Traditional deep learning techniques have so far been designed to work in isolation (Krizhevsky et al. 2012; Redmon et al. 2015). The WhONet has been trained to learn the positional errors associated with a particular car size, sensor error pattern as well as limited worn tyre states and tyre pressure variation. There is however a limit to the positional error the WhONet model can learn, as the sizes in which vehicles come are

numerous and the wearing of tyres and changes in tyre pressures are somewhat uncontrollable. An approach to addressing this problem could be to train a model to fit the dynamics of each vehicle type on the road. However, this method is too expensive and impractical particularly due to the different tyre states of each vehicle at different times of use. This paradigm can however be overcome through the use of transfer learning to recalibrate a pre-trained model to adapt to the dynamics and tyre state of the vehicles to which it is to be used.

Transfer learning within the context of deep learning, has mostly found motivations in complex problems requiring a large amount of data for accurate performance (Cheng et al. 2017). The difficulty in getting large amounts of labelled data and the high cost of labelling the data has made it a challenge to sufficiently train accurate deep learning models for different domains applications (Pan & Yang 2009). Through the use of pre-trained models such as on the ImageNet with millions of images relating to different categories, it has been shown that transfer learning can be used to transfer features and parameters of the pre-trained model to a new domain application (Shi et al. 2008; Wenchen Zheng et al. 2008; Zhuo et al. 2008). Transfer learning transcends specific tasks and domain applications to leverage knowledge learnt from a pre-trained model to solve problems in different application domains (Jialin Pan et al. 2007; Kuhlmann & Stone 2007; Ling et al. 2008; Pan et al. 2008; Yang et al. 2008; Yin et al. 2005; Zheng et al. 2008). It is with such inspiration that we propose in this chapter the recalibrated Wheel Odometry neural Network (R-WhONet). R-WhONet leverages the knowledge transfer capabilities of transfer learning to recalibrate the WhONet model to adapt to different vehicle dynamics and tyre states. We show that R-WhONet is able to consistently adapt a generic pre-trained WhONet model (which we refer to as G-WhONet for simplicity) to provide better uncertainty estimations whilst providing accuracies similar to a WhONet model trained specifically for the new vehicle.

6.2. Transfer Learning

6.2.1. Definition of representations

We define a Domain D as a two-element tuple made up of a feature space \mathcal{X} , (which is characterised by a specific tyre pressure, worn out state and vehicle dynamics), and a

marginal probability $P(\mathbf{X})$ such that \mathbf{X} is a sample data. Mathematically, the domain, D can be defined as $D = \{\mathcal{X}, P(\mathbf{X})\}$

Where $\mathbf{X} = \{\mathbf{x}_1, \dots, \mathbf{x}_m\}, \mathbf{x}_t \in \mathcal{X}$

Here, \mathbf{x}_t refers to a specific vector describing each sample data point at each time t . The specific vector \mathbf{X} describes the wheel speed measurement of the four wheels of the vehicle.

Task T is also defined as a two-element tuple with an objective function n and a label space \mathcal{Y} . The objective function can thus be expressed probabilistically as $P(\mathbf{Y}|\mathbf{X})$.

Mathematically, the task, T can be defined as $T = \{\mathcal{Y}, P(\mathbf{Y}|\mathbf{X})\} = \{\mathcal{Y}, n\}$.

Where $\mathbf{Y} = \{\mathbf{y}_1, \dots, \mathbf{y}_m\}, \mathbf{y}_t \in \mathcal{Y}$

here, \mathbf{y}_t refers to a specific vector describing each label of a sample data point at each time t . The specific vector \mathbf{y} describes the position uncertainty measurement of the vehicle.

We also define the following necessary representations:

Source Domain D_S – In this thesis, the source domain is defined as the vehicle whose dynamics and states are used to train the WhONet model.

Source task T_S – The source task is defined as the uncertainty measurement of the vehicle's position due to the dynamics and states of the source vehicle.

Target Domain D_T – We define the task domain as a new vehicle whose dynamics and states are different from the source domain.

Target Task T_T – The target task is defined as the uncertainty measurement of the vehicle's position due to the dynamics and states of the new vehicle.

6.2.2. Definition of Transfer Learning

Given a source task T_S , a reciprocal source domain D_S , a target task T_T and a target domain D_T , the aim of transfer learning is to enable the discovery of the target probability distribution $P(\mathbf{Y}_T|\mathbf{X}_T)$ in D_T with the statistics obtained from D_S and T_S where $D_S \neq D_T$ or $T_S \neq T_T$. Usually, a limited number of labeled target examples which are significantly smaller than the number of labeled source examples are presumed to be available.

Where \mathbf{Y}_T refers to the position uncertainty estimation and \mathbf{X}_T refers to the wheel speed measurements of the four wheels.

The following conditions need to be satisfied for transfer learning:

1. $\mathcal{X}_s \neq \mathcal{X}_T$, the feature spaces of the target and source domain are not the same.
2. $P(\mathbf{X}_s) \neq P(\mathbf{X}_T)$, the marginal probability distributions of the target and source domain are different.
3. $\mathcal{Y}_s \neq \mathcal{Y}_T$, the label space between the source and target tasks vary.
4. $P(\mathbf{Y}_s|\mathbf{X}_s) \neq P(\mathbf{Y}_T|\mathbf{X}_T)$, the conditional probability distributions of the target and source tasks differ.

6.2.3. Model Definitions

S-WhONet (specific - Wheel Odometry neural Network) – This refers to the WhONet model which is pre-trained only on the vehicle in which it is to be deployed i.e., the target domain becomes the source domain. For every new vehicle, change in vehicle state and/or dynamics, a new S-WhONet model is trained to predict the position estimation of the new vehicle at every time t .

As such, S-WhONet is characterised by the following definitions:

1. $\mathcal{X}_s = \mathcal{X}_T$, the feature spaces of the target and source domain are the same.
2. $P(\mathbf{X}_s) = P(\mathbf{X}_T)$, the marginal probability distributions of the target and source domain are similar.
3. $\mathcal{Y}_s = \mathcal{Y}_T$, the label space between the source and target tasks are the same.
4. $P(\mathbf{Y}_T|\mathbf{X}_T) = 0$, the conditional probability distributions of the target domain is not found, rather, the conditional probability distributions of the source domain is used directly in the target domain.

G-WhONet (Generic Wheel Odometry neural Network) – This describes the WhONet model trained on the source vehicle but does not undergo any form of adaptation before deployment on the target vehicle.

G-WhONet is characterised by the following:

1. $\mathcal{X}_s \neq \mathcal{X}_T$, the feature spaces of the target and source domain are different.
2. $P(\mathbf{X}_s) \neq P(\mathbf{X}_T)$, the marginal probability distributions of the target and source domain are similar.
3. $\mathcal{Y}_s \neq \mathcal{Y}_T$, the label space between the source and target tasks are the same.

4. $P(Y_T|X_T) = 0$ the conditional probability distributions of the target is not found, rather, the conditional probability distribution of the source domain $P(Y_S|X_S)$ is used in the target domain.

R-WhONet (recalibrated Wheel Odometry neural Network) – This describes the WhONet model which has its conditional probability distribution $P(Y_T|X_T)$ in the target domain (new vehicle), adapted from the source domain $P(Y_S|X_S)$. The conditional probability distribution is formulated from the source vehicle and then adapted to $P(Y_T|X_T)$ in the target domain for deployment on the new target vehicle.

As such, R-WhONet is characterised by the following:

1. $\mathcal{X}_S \neq \mathcal{X}_T$, the feature spaces of the target and source domain are not the same.
2. $P(X_S) \neq P(X_T)$, the marginal probability distributions of the target and source domain are different.
3. $\mathcal{Y}_S \neq \mathcal{Y}_T$, the label space between the source and target tasks vary.
4. $P(Y_S|X_S) \neq P(Y_T|X_T)$, the conditional probability distributions of the target and source tasks differ.

6.3. Model Training and Evaluation

This section details how the G-WhONet, S-WhONet and R-WhONet models are trained using the Keras-Tensorflow platform.

6.3.1. G-WhONet's Training

G-WhONet is trained on the IO-VNB data subsets presented in Table 3.13 and as described in Section 3.2.3.3, thus establishing the conditional distribution $P(Y_S|X_S)$. The IO-VNB datasets used to train the G-WhONet Model are characterised by about 1590 mins of drive time over a total distance of 1,165 km. The G-WhONet model was optimised using the adamax optimiser with an initial learning rate of 0.0007 and trained using the mean absolute error loss function and a dropout rate of 0.05 of the weighted connections in the hidden layers. Furthermore, the input features to the G-WhONet were normalised between 0 and 1 to reduce learning bias. Table 6.1 highlights the parameters characterising the training of the G-WhONet model.

6.3.2. S-WhONet's Training

S-WhONet was trained on the CUPAC data subsets presented in Table 3.14, as also described in Section 3.2.3.3 in order to determine the conditional probability distribution $P(\mathbf{Y}_T|\mathbf{X}_T)$. The CUPAC datasets used to train the S-WhONet model are characterised by about 104 mins of drive over 54.9 km. The S-WhONet model was optimised using the adamax optimiser with an initial learning rate of 0.0007 and trained using the mean absolute error loss function and a dropout rate of 0.05 of the weighted connections in the hidden layers. Just as with the G-WhONet model, the input features to the S-WhONet were normalised between 0 and 1 to reduce learning bias. Table 6.1 highlights the parameters characterising the training of the S-WhONet model.

6.3.3. R-WhONet's Training

The G-WhONet model of the source domain with conditional probability distribution $P(\mathbf{Y}_S|\mathbf{X}_S)$ is adapted to create the R-WhONet model which learns the target probability distribution $P(\mathbf{Y}_T|\mathbf{X}_T)$ of the new vehicle to which it is to be deployed on. The R-WhONet model is trained on the first m seconds of the CUPAC datasets highlighted on Table 3.18 and as justified in Section 3.2.3.4. The input features to the R-WhONet model were normalised between 0 and 1 to reduce learning bias. Table 6.1 highlights the parameters characterising the training of the WhONet model. Figure 6.1 describes the learning relationship between the R-WhONet and WhONet as well as the RWhONet's learning scheme.

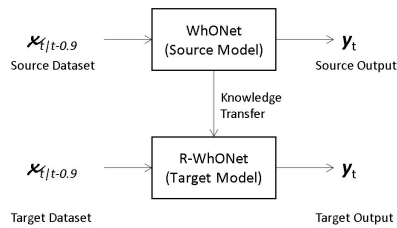


Figure 6.1. Learning scheme of the R-WhONet model

Table 6.1. Training parameters of the G-WhONet, S-WhONet and R-WhONet models

Parameters	G-WhONet/ S-WhONet/ R-WhONet
Learning rate	0.0007
Dropout rate	0.05
Time step	1
Hidden layers	1
Hidden neurons	72 per layer
Batch size	128

6.3.4. R-WhONet Training Time Selection Experiment

The R-WhONet model is trained on the first m seconds of the CUPAC datasets presented on Table 6.1. In order to determine the value of m that consistently gives the least position uncertainty estimation Y_T in the target domain, we experimented over a range of values for m (10 s, 20 s, 30 s, ..., and 120 s). The results from this experimentation are presented on Table 6.1. From observation, it can be seen that when m is defined as 50 seconds, R-WhONet provides the least position error estimation. This shows that the R-WhONet needs 50 seconds of data before it is able to most accurately adapt to its target domain. At an m value of 40 seconds, slightly worse results were obtained compared to an m value of 50 seconds, however at all other values of m , very poor results were obtained. This could be possibly attributed to the R-WhONet underfitting or overfitting the data in the target domain.

Table 6.2. Results from the experimentation of various values of m to determine the adaptation time for the R-WhONet model.

CUPAC		Positional CRSE (m)									
Dataset	m	10 s	20 s	30 s	40 s	50 s	60 s	70 s	80 s	90 s	100 s
Charlie 3	Max	14.8	243.8	68.2	11.2	10.6	124.5	75.5	69.7	148.5	33.7
	Min	5.6	7.2	6.7	4.5	3.5	6.3	6.3	6.5	6.8	6.5
	(μ)	10.1	66.0	21.6	9.0	7.8	30.0	23.0	22.9	48.5	18.8
	(σ)	2.0	81.1	20.2	1.0	1.4	39.0	21.9	20.0	51.4	9.7
Charlie 4	Max	21.5	29.8	21.8	21.5	21.1	21.6	22.8	23.4	23.5	23.9
	Min	5.5	5.1	5.5	5.5	5.6	5.7	6.4	6.8	8.2	7.3
	(μ)	11.5	15.0	11.8	11.6	11.5	12.1	12.5	13.4	15.9	13.4
	(σ)	3.8	5.1	5.9	4.1	4.0	5.2	5.1	5.1	5.0	6.1
Delta 2	Max	7.0	7.1	8.0	7.7	7.3	6.8	6.8	7.1	7.2	7.4
	Min	6.8	6.4	7.4	7.0	6.6	6.4	6.7	6.8	6.5	6.7
	(μ)	7.0	6.9	7.7	7.5	7.1	6.6	6.7	7.0	6.9	7.1
	(σ)	0.0	0.0	0.0	0.0	0.0	0.0	0.0	0.0	0.1	0.0
Delta 3	Max	11.9	8.7	10.9	8.7	10.2	11.8	12.1	12.5	7.8	8.1
	Min	7.3	6.9	7.4	6.7	6.4	6.6	6.0	5.8	5.9	6.2
	(μ)	9.4	7.9	8.9	7.5	8.1	8.3	8.0	7.7	6.7	7.0
	(σ)	0.9	0.4	0.7	0.6	0.8	1.2	0.8	1.1	0.6	0.5

6.3.5. Model Evaluation

The R-WhONet, G-WhONet and S-WhONet and the physics model (WPM) are evaluated on the CUPAC datasets presented on Table 3.18. The CUPAC dataset used for evaluation has vehicular dynamics and state properties such as tyre pressure, worn out tyre state, driving behavior, etc. different from the IO-VNBD dataset which was used for training the G-WhONet model. The models are evaluated on the longer-term GNSS outage scenarios of 30s, 60s, 120s and 180s just as in Chapter 5.

Each test set used in the longer term GNSS outage scenarios are broken down into test sequences of 30s, 60s, 120s or 180s depending on the outage scenario being evaluated. The maximum, minimum, average and standard deviation, of the CRSE's and CTE's of all the test sequences evaluated within each dataset are recorded in each scenario and used in evaluating the performance of each model. GPS outages are assumed on the test scenarios, for the purpose of the investigation with a prediction frequency of 1s.

6.4. Results and Discussion

In this section, the performance of the R-WhONet in comparison to the G-WhONet model, S-WhONet model and WPM are evaluated on the 30 s, 60 s, 120 s and 180 seconds using the CUPAC datasets presented on Table 3.18.

6.4.1. 30 s GNSS Outage

In the 30 seconds GNSS outage scenario, R-WhONet provides an CRSE reduction of up to 36% on the G-WhONet's estimation. As presented on Table 6.3 and 6.4, the R-WhONet achieves the best average CTE and CRSE of 0.31 m and 1.22 m compared to 1.11 m and 1.46 m of the G-WhONet over a max distance per test sequence of 618 m of all 121 sequences evaluated on the CUPAC dataset (see Table 3.18). Moreover, on the maximum metric, the R-WhONet achieves the best CTE and CRSE of 0.92 m and 1.60 m respectively while G-WhONet achieves the best CTE and CRSE of 1.96 m and 2.02 m respectively as well.

The robustness of the R-WhONet is further emphasized by the low standard deviation of 0.27 obtained compared to 0.20 of G-WhONet. The result so obtained shows that R-WhONet is able to adapt the G-WhONet model to the new vehicle with performances relatively closer to a model (S-WhONet) trained specifically for the new vehicle as further illustrated in Figures 6.2-6.4.

Table 6.3. CRSE performance comparison of the R-WhONet, G-WhONet, S-WhONet and WPM on the 30 seconds GNSS outage scenario.

CUPAC Dataset	Performance Metrics	Positional Estimation Error (m)				Total Distance Travelled (m)	Number of Test Sequences evaluated
		CRSE					
		WPM	R-WhO-Net	G-WhO-Net	S-WhO-Net		
Charlie 3	Max	13.71	4.14	5.68	5.36	618	45
	Min	2.25	0.50	0.56	0.37	18	
	(μ)	7.43	1.34	1.61	1.14	313	
	(σ)	2.81	0.71	0.90	0.73	154	
Charlie 4	Max	16.02	6.25	9.70	8.53	407	22
	Min	2.95	0.62	0.80	0.41	12	
	(μ)	7.42	1.89	2.05	1.62	217	
	(σ)	2.79	1.35	2.00	1.69	95	
Delta 2	Max	23.26	1.60	2.02	1.42	261	16
	Min	3.19	0.83	0.69	0.51	55	
	(μ)	8.85	1.22	1.46	0.94	193	
	(σ)	4.72	0.20	0.32	0.24	65	
Delta 3	Max	12.45	3.74	5.22	5.07	346	38
	Min	4.05	0.84	0.90	0.43	8	
	(μ)	7.22	1.53	1.77	1.18	131	
	(σ)	2.47	0.57	0.70	0.72	97	

Table 6.4. CTE performance comparison of the R-WhONet, G-WhONet, S-WhONet and WPM on the 30 seconds GNSS outage scenario.

CUPAC Dataset	Performance Metrics	Positional Estimation Error (m)				Total Distance Travelled (m)	Number of Test Sequences evaluated
		CTE					
		WPM	R-WhO-Net	G-WhO-Net	S-WhO-Net		
Charlie 3	Max	10.26	2.90	3.90	2.05	618	45
	Min	0.18	0.00	0.03	0.00	18	
	(μ)	2.96	0.60	1.13	0.46	313	
	(σ)	2.15	0.61	0.93	0.47	154	
Charlie 4	Max	5.95	3.30	6.42	3.87	407	22
	Min	0.61	0.00	0.34	0.00	12	
	(μ)	2.82	0.84	1.46	0.81	217	
	(σ)	1.70	0.83	1.37	0.86	95	
Delta 2	Max	4.24	0.92	1.96	0.78	261	16

Delta 3	Min	0.83	0.00	0.16	0.01	55	38
	(μ)	2.61	0.31	1.11	0.30	193	
	(σ)	1.21	0.27	0.42	0.20	65	
	Max	7.58	1.88	2.47	1.36	346	
	Min	0.19	0.00	0.09	0.00	8	
	(μ)	2.08	0.55	1.33	0.37	131	
	(σ)	1.85	0.45	0.52	0.33	97	

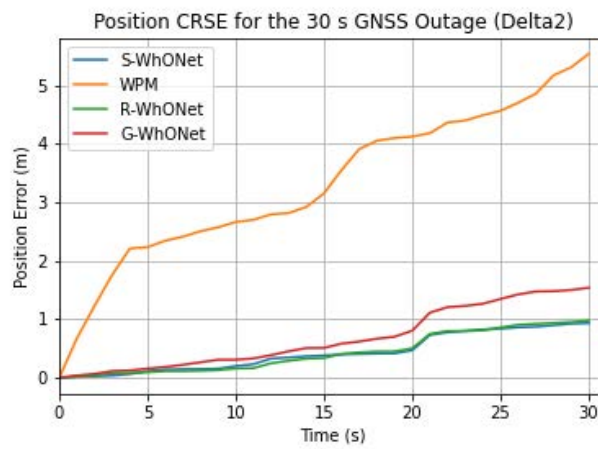


Figure 6.2. Sample CRSE evolution of the models on the Delta 2 CUPAC dataset during the 30 s GNSS outage scenario after recalibration.

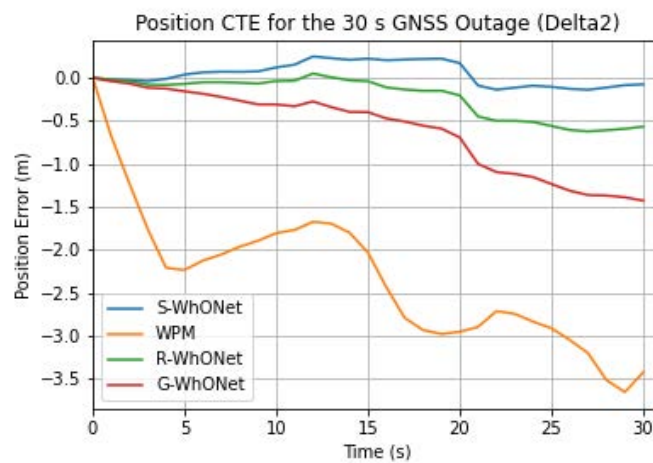


Figure 6.3. Sample CTE evolution of the models on the Delta 2 CUPAC dataset during the 30 s GNSS outage scenario after recalibration.

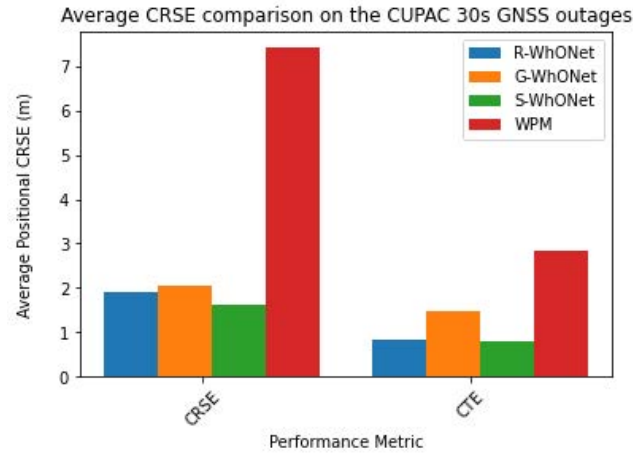


Figure 6.4. CRSE and CTE comparison of the models on the Charlie 4 CUPAC dataset during the 30 s GNSS outage scenario after recalibration.

6.4.2. 60 s GNSS Outage

Tables 6.5 and 6.6. reports the result from the 60 seconds GNSS outage experiment on CUPAC On the CTE and CRSE metric, the R-WhONet provides the best average of 0.50 m and 2.45 m compared to 2.15 m and 2.89 m of the G-WhONet over a max test sequence distance covered of 1234 m of all 60 sequences evaluated on the CUPAC dataset (see Table 3.18.). Also, on the maximum metric, the R-WhONet obtains the best CTE and CRSE of 0.83 m and 2.72 m in contrast to the G-WhONet best CTE and CRSE of 3.02 m and 3.65 m.

The consistency of the R-WhONet is further highlighted by the low standard deviation of 0.18 obtained compared to 0.42 of G-WhONet as reported in Table 6.5. The evolution of the R-WhONet, G-WhONet, S-WhONet and WPM error estimations over time on both the CTE and CRSE metric as well as the error comparisons are illustrated on Figures 6.5-6.7.

Table 6.5. CRSE performance comparison of the R-WhONet, G-WhONet, S-WhONet and WPM on the 60 seconds GNSS outage scenario.

CUPAC Dataset	Performance Metrics	Positional Estimation Error (m)				Total Distance Travelled (m)	Number of Test Sequences evaluated
		CRSE					
		WPM	R-WhO-Net	G-WhO-Net	S-WhO-Net		
Charlie 3	Max	21.48	5.56	6.62	4.94	1234	22
	Min	6.08	1.13	1.43	1.03	281	
	(μ)	14.86	2.75	3.25	2.54	627	
	(σ)	4.14	0.94	1.32	0.90	284	

Charlie 4	Max	19.40	11.26	12.46	11.41	643	11
	Min	7.91	1.63	2.21	1.50	250	
	(μ)	15.06	3.76	4.18	3.70	445	
	(σ)	3.51	1.87	3.13	2.34	149	
Delta 2	Max	32.17	2.72	3.65	2.60	490	8
	Min	8.41	2.02	2.15	1.66	149	
	(μ)	17.69	2.45	2.89	2.22	385	
	(σ)	7.01	0.18	0.47	0.27	104	
Delta 3	Max	18.19	5.00	4.31	4.23	661	19
	Min	10.17	2.00	2.76	1.56	24	
	(μ)	14.45	2.76	3.36	2.46	253	
	(σ)	2.74	0.63	0.42	0.45	168	

Table 6.6. CTE performance comparison of the R-WhONet, G-WhONet, S-WhONet and WPM on the 60 seconds GNSS outage scenario.

CUPAC Dataset	Perfor- mance Metrics	Positional Estimation Error (m)				Total Distance Travelled (m)	Number of Test Sequences evaluated
		CTE					
		WPM	R-WhO- Net	G-WhO- Net	S-WhO- Net		
Charlie 3	Max	9.17	2.90	6.59	2.61	1234	22
	Min	0.10	0.00	0.11	0.00	281	
	(μ)	3.85	1.03	2.15	0.81	627	
	(σ)	2.56	0.81	1.53	0.73	284	
Charlie 4	Max	8.44	3.45	6.87	3.96	643	11
	Min	1.35	0.00	0.00	0.00	250	
	(μ)	3.94	1.37	2.71	1.41	445	
	(σ)	2.04	0.68	2.06	0.84	149	
Delta 2	Max	6.14	0.83	3.02	0.75	490	8
	Min	0.67	0.00	1.30	0.01	149	
	(μ)	3.32	0.50	2.21	0.50	385	
	(σ)	1.95	0.25	0.63	0.14	104	
Delta 3	Max	9.89	2.92	4.22	1.49	661	19
	Min	0.01	0.02	0.21	0.00	24	
	(μ)	2.45	0.80	2.59	0.52	253	
	(σ)	2.36	0.69	0.82	0.40	168	

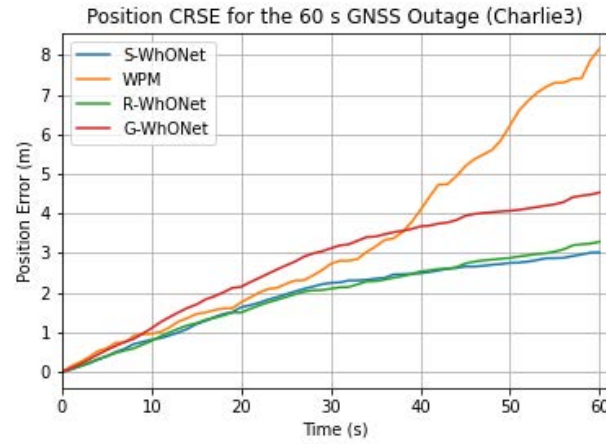


Figure 6.5. Sample CRSE evolution of the models on the Delta 2 CUPAC dataset during the 60 s GNSS outage scenario after recalibration.

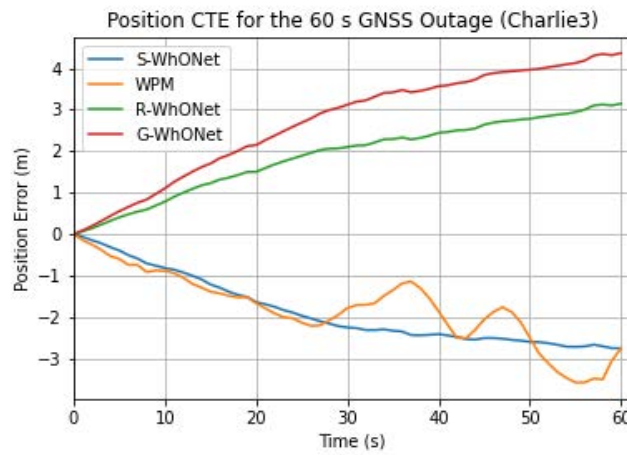


Figure 6.6. Sample CTE evolution of the models on the Delta 2 CUPAC dataset during the 60 s GNSS outage scenario after recalibration.

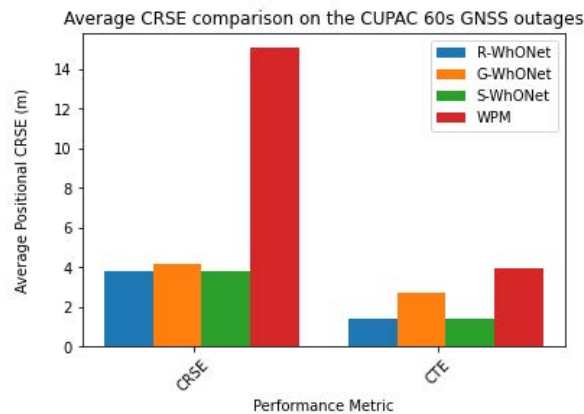


Figure 6.7. CRSE and CTE comparison of the models on the Charlie 4 CUPAC dataset during the 60 s GNSS outage scenario after recalibration.

6.4.3. 120 s GNSS Outage

The R-WhONet outperforms the G-WhONet on the CRSE metric by up to 31% on the 120 seconds GNSS outage scenario as illustrated in Figures 6.8 and 6.9. When evaluated on the CUPAC, as shown on Table A12,, the R-WhONet achieves the best average CTE and CRSE of 0.68 m and 4.67 m compared to 4.09 m and 5.54 m of the G-WhONet over a max distance per test sequence of 2262 m of all 29 sequences evaluated on the CUPAC dataset (see Table 6.7 and 6.8). In addition, on the maximum metric, the R-WhONet has the best CTE and CRSE of 0.99 m and 4.75 m while G-WhONet has CTE and CRSE of 5.62 m and 6.26 m CTE and CRSE respectively.

The consistency of the R-WhONet is further emphasized by the low standard deviation of 0.02 obtained in comparison to 0.52 of G-WhONet as reported in Table 6.7. The result so obtained shows that R-WhONet is able to adapt the G-WhONet model to the new vehicle with performances relatively closer to a model (S-WhONet) trained specifically for the new vehicle as further illustrated in Figure 6.10.

Table 6.7. CRSE performance comparison of the R-WhONet, G-WhONet, S-WhONet and WPM on the 120 seconds GNSS outage scenario.

CUPAC Dataset	Performance Metrics	Positional Estimation Error (m)				Total Distance Travelled (m)	Number of Test Sequences evaluated
		CRSE					
		WPM	R-WhO-Net	G-WhO-Net	S-WhO-Net		
Charlie 3	Max	38.45	10.32	9.44	9.40	2262	11
	Min	15.64	3.45	4.07	2.27	637	
	(μ)	29.71	5.69	6.49	4.57	1254	
	(σ)	7.53	1.46	1.71	1.61	539	
Charlie 4	Max	38.54	18.25	19.82	12.10	1140	5
	Min	25.10	3.53	4.44	2.60	558	
	(μ)	30.12	7.86	8.36	6.65	890	
	(σ)	4.77	3.54	5.79	3.71	204	
Delta 2	Max	47.53	4.75	6.26	4.68	887	4
	Min	20.76	4.45	5.02	2.70	540	
	(μ)	35.90	4.67	5.54	3.75	735	
	(σ)	11.21	0.02	0.52	0.45	145	
Delta 3	Max	33.37	5.93	7.64	5.74	1165	9
	Min	24.09	3.90	5.65	3.15	204	
	(μ)	29.34	5.17	6.73	4.30	505	
	(σ)	3.88	0.39	0.62	0.66	310	

Table 6.8. CTE performance comparison of the R-WhONet, G-WhONet, S-WhONet and WPM on the 120 seconds GNSS outage scenario.

CUPAC Dataset	Performance Metrics	Positional Estimation Error (m)				Total Distance Travelled (m)	Number of Test Sequences evaluated
		CTE					
		WPM	R-WhO-Net	G-WhO-Net	S-WhO-Net		
Charlie 3	Max	14.78	2.86	8.50	2.34	2262	11
	Min	0.14	0.00	1.09	0.00	637	
	(μ)	6.39	1.40	4.09	1.06	1254	
	(σ)	4.43	0.94	2.23	0.72	539	
Charlie 4	Max	12.93	5.40	12.89	5.48	1140	5
	Min	0.29	0.00	1.50	0.01	558	
	(μ)	5.32	2.46	5.41	2.64	890	
	(σ)	4.53	0.55	3.94	0.82	204	
Delta 2	Max	7.63	0.99	5.62	1.08	887	4
	Min	1.51	0.07	3.08	0.01	540	
	(μ)	4.37	0.68	4.15	0.79	735	
	(σ)	2.52	0.35	1.08	0.08	145	
Delta 3	Max	9.82	2.71	6.84	1.49	1165	9
	Min	0.65	0.00	3.01	0.02	204	
	(μ)	3.84	1.34	5.19	0.83	505	
	(σ)	3.15	0.83	1.20	0.40	310	

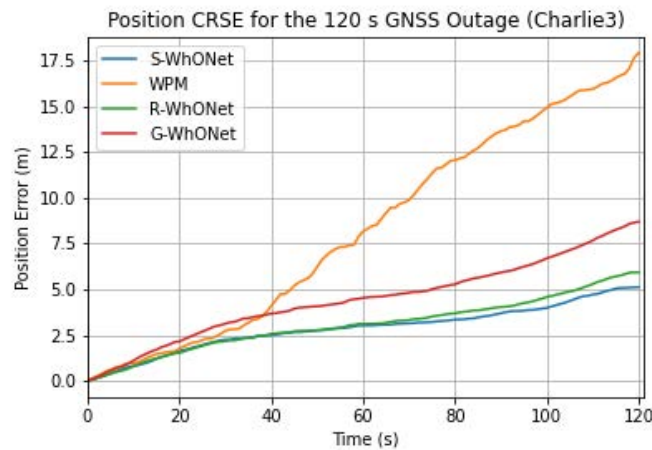


Figure 6.8. Sample CRSE evolution of the models on the Delta 2 CUPAC dataset during the 120 s GNSS outage scenario after recalibration.

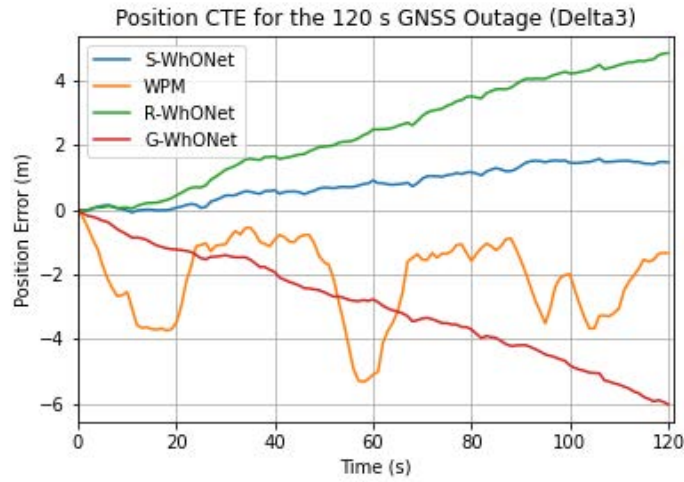


Figure 6.9. Sample CTE evolution of the models on the Delta 2 CUPAC dataset during the 120 s GNSS outage scenario after recalibration.

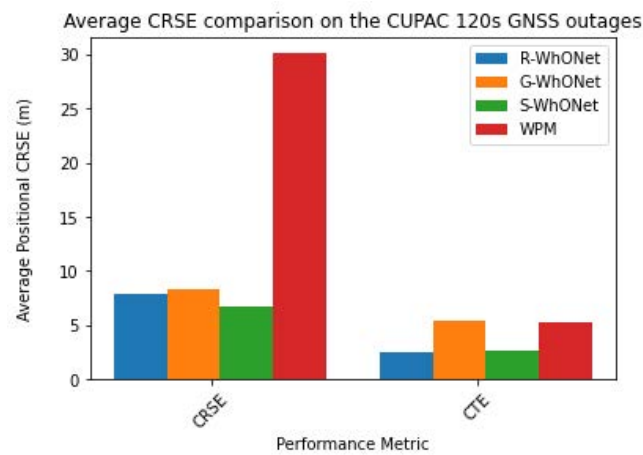


Figure 6.10. CRSE and CTE comparison of the models on the Charlie 4 CUPAC dataset during the 120 s GNSS outage scenario after recalibration.

6.4.4. 180 s GNSS Outage

In the 180 seconds GNSS outage scenario, R-WhONet provides a CRSE reduction of up to 32% on the G-WhONet's estimation. As presented on Tables 6.9 and 6.10, the R-WhONet achieves the best average CTE and CRSE of 0.26 m and 6.84 m compared to 5.50 m and 8.31 m of the G-WhONet over a max distance per test sequence of 3496 m of all 18 sequences evaluated on the CUPAC dataset (see Table 3.18.). Furthermore, on the maximum metric, the R-WhONet achieves the best CTE and CRSE of 0.49 m and 7.30 m compared to the G-WhONet's best CTE and CRSE of 6.46 m and 8.43 m.

The consistency of the R-WhONet is better accentuated by the low standard deviation of 0 obtained, compared to 0.12 of G-WhONet as reported in Tables 6.9 and

6.10. The result so obtained shows that R-WhONet is able to adapt the G-WhONet model to the new vehicle domain, with performances relatively closer to a model (S-WhONet) trained specifically for the new vehicle, as further illustrated in Figures 6.11-6.13.

Table 6.9. CRSE performance comparison of the R-WhONet, G-WhONet, S-WhONet and WPM on the 180 seconds GNSS outage scenario.

CUPAC Dataset	Performance Metrics	Positional Estimation Error (m)				Total Distance Travelled (m)	Number of Test Sequences evaluated
		CRSE					
		WPM	R-WhO-Net	G-WhO-Net	S-WhO-Net		
Charlie 3	Max	55.25	10.34	15.31	9.94	3496	7
	Min	23.99	4.62	5.49	3.74	1012	
	(μ)	44.42	7.87	9.86	7.69	1916	
	(σ)	9.19	1.38	2.90	1.31	772	
Charlie 4	Max	54.72	21.23	22.44	21.14	1716	3
	Min	41.51	5.50	7.36	5.22	1220	
	(μ)	46.94	11.45	12.52	11.28	1400	
	(σ)	5.64	4.24	7.01	5.27	224	
Delta 2	Max	68.59	7.30	8.43	6.58	1278	2
	Min	39.12	6.22	8.19	6.15	928	
	(μ)	53.86	6.84	8.31	6.39	1103	
	(σ)	14.74	0.04	0.12	0.00	175	
Delta 3	Max	48.63	10.18	10.52	9.20	1624	6
	Min	39.39	6.35	9.06	6.10	323	
	(μ)	44.01	7.73	10.09	7.38	758	
	(σ)	4.62	0.94	0.51	0.50	470	

Table 6.10. CTE performance comparison of the R-WhONet, G-WhONet, S-WhONet and WPM on the 180 seconds GNSS outage scenario.

CUPAC Dataset	Performance Metrics	Positional Estimation Error (m)				Total Distance Travelled (m)	Number of Test Sequences evaluated
		CTE					
		WPM	R-WhO-Net	G-WhO-Net	S-WhO-Net		
Charlie 3	Max	20.66	4.84	15.09	3.35	3496	7
	Min	0.48	0.05	0.98	0.03	1012	
	(μ)	10.12	1.66	5.50	1.57	1916	
	(σ)	6.00	1.61	4.54	0.73	772	
	Max	11.94	5.10	14.59	5.21	1716	3

Charlie 4	Min	8.13	0.04	3.26	0.14	1220	2
	(μ)	10.14	3.60	7.78	3.68	1400	
	(σ)	1.56	0.31	4.90	0.18	224	
Delta 2	Max	9.81	0.49	6.46	0.25	1278	
	Min	3.30	0.02	5.99	0.07	928	
	(μ)	6.56	0.26	6.22	0.16	1103	
	(σ)	3.26	0.00	0.23	0.01	175	
Delta 3	Max	8.73	3.17	9.54	1.10	1624	6
	Min	0.46	0.03	5.43	0.00	323	
	(μ)	4.90	1.29	7.78	0.53	131	
	(σ)	3.17	0.65	1.29	0.33	97	

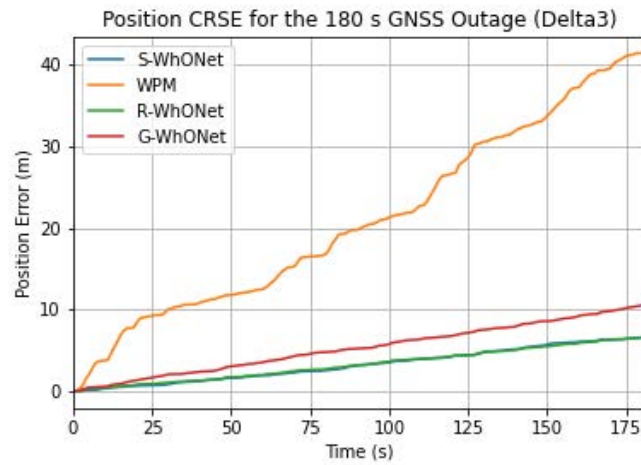


Figure 6.11. Sample CRSE evolution of the models on the Delta 2 CUPAC dataset during the 180 s GNSS outage scenario after recalibration.

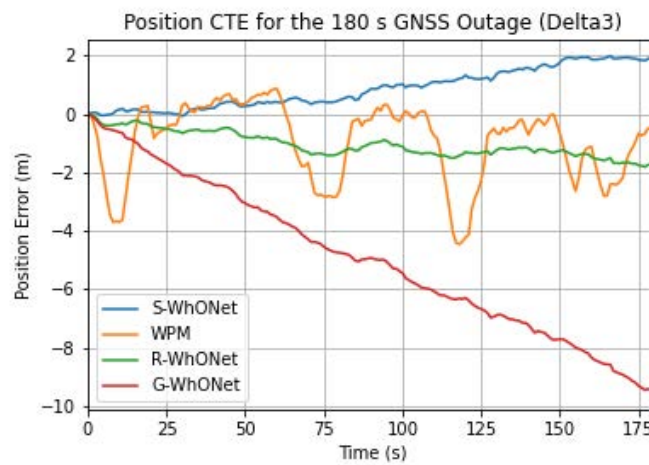


Figure 6.12. Sample CTE evolution of the models on the Delta 2 CUPAC dataset during the 180 s GNSS outage scenario after recalibration.

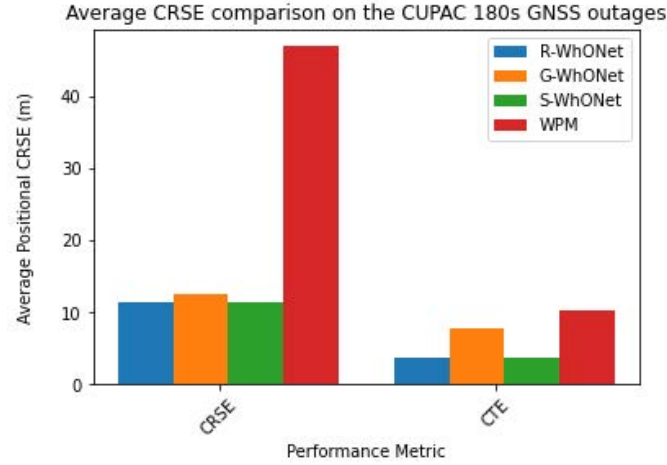


Figure 6.13. CRSE and CTE comparison of the models on the Charlie 4 CUPAC dataset during the 180 s GNSS outage scenario after recalibration.

6.5. Summary

In this chapter, R-WhONet (Recalibration Wheel Odometry neural Network) was proposed for the adaptation of the WhONet model to vehicles with different dynamics and states such as tyre pressures, worn out tyre state, driving behavior, size, etc. Due to the difference in the feature space of different vehicles as affected by varying vehicle dynamics and state properties, a model trained to learn the correlation between the wheel speed and the position uncertainty on a vehicle A, will not fit a vehicle B with different motion characteristics. As it is expensive and impractical to train a specific WhONet (S-WhONet) model for every vehicle's dynamics and different worn-out tyre states as well as tyre pressure, we leveraged transfer learning to recalibrate a generic WhONet (G-WhONet) model trained on a source Vehicle A, for an on the fly adaptation to a new target vehicle B. This provides an improved estimation of the vehicles position uncertainty estimation needed for continuous positioning correction. We showed that a G-WhONet model does not fit a target vehicle as accurately as a S-WhONet trained for that vehicle. We also further showed that the R-WhONet is able to improve the performance of the G-WhONet model to provide better uncertainty estimation accuracies closer to the S-WhONet model.

It is however worth noting that one of the major reasons why the R-WhONet model does not give estimations that exactly match that of the S-WhONet model is due to the limitation of the features of the new target vehicles used in the transfer learning training process. The first 50 seconds of the training data which is used for transfer learning might

not have features which the model will encounter after adaptation. The continuous adaptation of the model might provide the opportunity to address this limitation. The use of systems that are able to inform on the change in the states of the vehicle, through techniques that inform on the worn-out state of the tyres or through information on the change in tyre pressures, the WhONet model can be continuously triggered into recalibration mode for adaptation to the vehicle's new state. As the datasets used in this thesis do not provide information on exactly when the vehicular dynamics properties have changed, it has been challenging to implement such a system. However, this will be the subject of future research.

Chapter 7

Conclusions and Future Work

7.1. Summary of Contributions

The use of deep learning for robust and accurate localisation of autonomous vehicles in GNSS deprived environments using ego-motion sensors were investigated in this thesis.

Inertial navigation sensors have unique properties which are important for ego-motion localisation of autonomous vehicles. However, low-cost ego-motion sensors are plagued by noises which are cascaded exponentially over time leading to poor navigation results. Many studies on the use of deep learning to learn the noise in these sensors have been successful, however, their investigations have mostly been focused on vehicular tracking on simple straight line and low-speed drive trajectories. As this is not realistic of everyday driving experience, the first challenge becomes how to consistently and accurately learn the noise in the inertial data for navigation in challenging driving environments. Features characterizing these complex scenarios are sometimes indistinguishable from the noises inherent in the data making it a challenge for the deep learning model to accurately track the vehicle. More so, the dataset used by other researchers for their investigations are either not publicly available or

characterised by a high signal to noise ratio and as such too expensive to be found on present day vehicles. Chapter 3 describes a publicly released large- scale dataset on noisy ego-motion data called IO-VNBD (Inertial Odometry Vehicular Navigation Benchmark Dataset) characterised by 5700km over 98hrs (publicly available at <https://github.com/onyekpeu/IO-VNBD>). The dataset captures information such as the vehicle's longitudinal acceleration, yaw rate, heading, GPS co-ordinates (latitude, longitude) amongst others at each time instance from the Electric Control Unit (ECU) of from four vehicles and three smart phones with a sampling interval of 10 Hz. Furthermore, we described the physics model used to estimate the vehicles orientation rate from the gyroscope, which we called GPM (Gyroscope orientation estimation Physics Model), the physics model used to estimate the vehicles position from the accelerometer which we called APM (Accelerometer position estimation Physics Model) and the physics model used to estimate the vehicles position from the wheel encoder which we called WPM (Wheel encoder position estimation Physics Model), these defined physics models are used as baselines for comparison in this thesis. The deep learning models are also described in chapter 3. We described the deep learning model used to estimate the vehicles orientation rate which we called GyroNet (Gyroscope-based orientation rate estimation neural Network model), the deep learning model used to estimate the vehicle's position from the accelerometer's measurement which we called AccNet (Accelerometer-based position estimation neural Network) and the deep learning model used to estimate the vehicles position from the wheel encoder's measurement which we called WhONet (Wheel Odometry neural Network). In addition, we also introduced the metrics to evaluate the performance of the deep learning and the physics model in Chapter 3 as well as the ground truth position formulation using Vincenty's 's inverse formula on the GPS coordinates and the orientation rate formulation from the GPS heading.

In Chapter 4, extensive experiment were conducted on the IO-VNB dataset to investigate the performance of WhONet, AccNet, and GyroNet in comparison to WPM, APM and GPM respectively on several challenging driving scenarios such as hand brake, motorway, sharp cornering and successive left and right turns, wet road, quick changes acceleration, and roundabout. The results obtained over several test sequences each of 10s length, showed that the scenarios explored were indeed complex for the deep learning and physics models however the deep learning models provided significant estimation

improvement in comparison to the corresponding physics model. The WhONet offered up to 91% error reduction over the WPM's estimation, the AccNet improved on the APM's position estimation by up to 89% and the GyroNet improved on the orientation rate estimation on the GPM by 83%.

We also compared the performance of WhONet to AccNet and discovered that the WhONet is able to provide up to a 99% reduction on the position error comparatively, thus establishing it as a suitable model for robust and accurate vehicular position tracking in complex driving environments. Of all the complex driving scenarios studied, the roundabout scenario proved to be the most challenging for all models investigated. Chapter 4 thus answers the 1st research question "How can deep learning improve localisation using inertial sensor data in complex driving environments?" by showing the capability of the AccNet and GyroNet model to provide better position estimates relative to other compared models whilst using inertial sensor data. The 2nd research question "How can deep learning be used to improve on localisation with wheel encoder data comparatively to inertial sensor data in challenging environments?" is also answered in this chapter through the establishment of the superiority of the WhONet model over the AccNet model in AV position estimation.

Having established the superiority of the Wheel encoder-based position estimation deep learning (WhONet) model compared to the accelerometer-based position estimation deep learning (AccNet) model, in Chapter 5, we further extend the analysis to evaluate the performance of the WhONet model over longer term GNSS outages (defined as up to 180s). The performance of the proposed WhONet was extensively evaluated on longer GNSS outage scenarios comprising of 129 test sequences of 30 s simulated GNSS outage, 197 sequences of 60s simulated GNSS outages, 399 sequences of 120s simulated GNSS outages and 809 sequences of 180s simulated GNSS outages. The total trajectory covered across all sequences investigated in each GNSS scenario is 493 km. We demonstrate that the WhONet is able to provide up to 93 % improvement over the directly integrated positioning information from the WPM. The WhONet is able to provide an average accuracy of 8.62 m after 5.6 km of travel. Chapter 5 thus answers the 3rd research question "How can deep learning be used to improve localisation in longer term GNSS outages?" by showing its superiority over the compared models in longer GNSS outages of up to 180s.

Chapter 6 explores the challenge of WhONet's generalization to new vehicle with different dynamics and states. Vehicular features such as the physical state of the vehicle (worn out state of the tyres, pressure of the tyre, passenger weight distribution, size of the vehicle, etc.) vary from vehicle to vehicle but ego-motion sensor datasets are always specific to the vehicle used in collecting the data. As such models specifically trained with data from a vehicle with limited feature characteristics affecting the motion of the vehicle¹ do not adapt to give correct position estimation in other vehicles. With the inspiration from transfer learning, we proposed the Recalibrated Wheel Odometry neural Network (R-WhONet) which leverages the knowledge transfer capabilities of transfer learning to recalibrate the WhONet model to vehicles with different dynamics and tyre states. We showed that the R-WhONet is capable of consistently adapting to a pre-trained generic WhONet model to provide better uncertainty estimations (with up to 36% error reductions) whilst providing accuracies similar to a WhONet model trained specifically for the new vehicle. We thus answer the 4th research question "How can deep learning localisation models be adapted to vehicles with different error feature characteristics and vehicular state and dynamics?" in this chapter.

7.2. Limitations

We however do stress that despite the performance of the deep learning models, the accuracy and robustness of their estimations are limited by the quality of the data obtained from the GNSS receiver which is used in training the models and also as baselines in comparing the performance of the models. The information provided by the (VBOX HD2, 2019) documentation suggests that the errors from the GNSS receiver data are within the range of ± 3 m. The use of quality GNSS data for the model training and analysis has the potential to improve the performance of the deep learning models.

In order to provide continuous positioning information for vehicular localisation, the deep learning models need to provide estimates of the vehicles position and orientation in real time. Although, minimal parameterisations of the neural networks were considered during the selection of the deep learning models, real time implementation of these models was not the focus of this thesis and as such will be the subject of future research.

¹ not all scenarios that can influence the position estimation of the vehicle can be captured in any dataset

7.3. Future Work

There is still room for a lot of improvement on vehicular localisation in GNSS deprived environments. With a broader vision towards improving the reliability, robustness, generalisation and accuracy of deep learning models especially in longer term GNSS outages, the following represents prospective research directions that are worthy of explorations:

7.3.1. Map Matching

Map matching is useful for so many purposes; it is used when a navigation system displays the vehicle's location on a map. Map matching indicates a process of assigning geographical objects to locations on a digital map. Most common geographical objects are point positions obtained from a positioning system, which are most times GPS receivers. In many applications of map matching, information such as speed limits are assigned to the representations of roads on a map. The objective of map matching is to put the GPS positions at their "accurate" locations on the polylines in the map.

Due to unreliability, the GPS positions do not intersect with polylines generally. The use of map matching can be extended towards the estimates from the deep learning models as a means to explore the potential for improved localisation of the vehicles in GNSS deprived environments through polylines repositioning on the map.

7.3.2. Explainable, Reliable and Accurate Localisation

In today's society, the presence of automated decision-making is constantly increasing. From shaping our consumption of goods (via e-marketing) to translating our thoughts and speech, to deciding on how much we pay for insurance machine learning plays an important role. Machine learning are also present in sciences, they have found promising use in applications such as finding spatial trends or temporal patterns in data, or improved parameterisation in climate simulations. Most machine learning applications however focus on optimising performance metrics, such as accuracy, which are not always good trust indicators. Although the increase in model complexity and data size may improve the accuracy of machine learning predictions, these models may be forced to rely on illusory correlations, draw conclusions that are not considering the

underlying principles defining the systems dynamics or encode and magnify bias within the system. Because of these, the relations between outputs and inputs become difficult to interpret and the predictions uncertainty as well as the confidence in the model become harder to estimate.

Instead of trying to fix the fundamental problems later on, it is better and more practical to implement eXplainable Artificial Intelligence (XAI) procedures at the very start of the machine and deep learning adoption. The XAI procedures consist of ensemble runs, random sampling and Monte-Carlo simulations, which are quite common methods in engineering. XAI comprises of a systematic perturbation of some components of the model, which enables it to observe how it affects the model's estimates mostly using sensitivity analyses. Due to the safety critical nature of the autonomous vehicle navigation systems, interpretability of the vehicular navigation models are necessary and provide sufficient arguments for the suitability of a model for use on the road as well as sufficient argument when communicating anomaly behaviours to insurance stakeholders, Original Equipment Manufacturers (OEM) and other relevant stakeholders, and as such presents an interesting research direction to be explored.

7.3.3. Sensor Fusion

Deep learning approaches for vehicular localisation have provided good performances despite how they rarely consider robust and information-rich fusion strategies for handling imperfect sensor data. We suggest the exploration of sensor fusion frameworks to enhance the model's robust adaptation to real life scenarios with characteristics such as bad sensor synchronization, corrupt or missing data, etc. Other sensor information on the vehicle such as surrounding air temperature, brake pressure, steering angle amongst others may offer further insights on improving the accuracy, robustness and generalisation of the vehicular localisation deep learning models in a wide range of scenarios.

References

- ACFR (2016) *Marine Robotics Datasets - ACFR*. available from
<<http://marine.acfr.usyd.edu.au/datasets/>>
- Ahmed, S., Huda, M.N., Rajbhandari, S., Saha, C., Elshaw, M., and Kanarachos, S. (2019) 'Pedestrian and Cyclist Detection and Intent Estimation for Autonomous Vehicles: A Survey'. *Applied Sciences* [online] 9 (11), 2335. available from
<<https://www.mdpi.com/2076-3417/9/11/2335>> [22 March 2020]
- AndroSensor (2019) *AndroSensor for Android* [online] available from
<<http://www.fivasim.com/androsensor.html>> [19 January 2021]
- Babak, S.-J., Hussain, S.A., Karakas, B., and Cetin, S. (2017) *Control of Autonomous Ground Vehicles: A Brief Technical Review - IOPscience* [online] available from
<<https://iopscience.iop.org/article/10.1088/1757-899X/224/1/012029>> [22 March 2020]
- Blanco-Claraco, J.-L., Moreno-Dueñas, F.-Á., and González-Jiménez, J. (2013) 'The Málaga Urban Dataset: High-Rate Stereo and LiDAR in a Realistic Urban Scenario':
Http://Dx.Doi.Org/10.1177/0278364913507326 [online] 33 (2), 207–214. available from
<<https://journals.sagepub.com/doi/full/10.1177/0278364913507326>>
- Bonarini, A., Burgard, W., and Fontana, G. (2006) *Datasets : The Rawseeds Project*. available from
<<http://www.rawseeds.org/home/category/benchmarking-toolkit/datasets/>>
- Borenstein, J. and Feng, L. (1996) *Measurement and Correction of Systematic Odometry Errors in Mobile Robots*. vol. 12
- Borenstein, J. and Feng, L. (9AD) *Correction of Systematic Odometry Errors in Mobile Robots*
[online] available from <<https://ieeexplore.ieee.org/abstract/document/525942/>> [15
-

February 2021]

- Brossard, M., Barrau, A., and Bonnabel, S. (2020) 'AI-IMU Dead-Reckoning'. *IEEE Transactions on Intelligent Vehicles*
- Brossard, M., Bonnabel, S., and Barrau, A. (2020) *Denoising IMU Gyroscopes with Deep Learning for Open-Loop Attitude Estimation* [online] available from <<https://github.com/>> [15 June 2021]
- Burri, M., Nikolic, J., Gohl, P., Schneider, T., Rehder, J., Omari, S., Achtelik, M.W., and Siegwart, R. (2016) 'The EuRoC Micro Aerial Vehicle Datasets': <https://doi.org/10.1177/0278364915620033> [online] 35 (10), 1157–1163. available from <<https://journals.sagepub.com/doi/abs/10.1177/0278364915620033>>
- Carlevaris-Bianco, N., Ushani, A.K., and Eustice, R.M. (2016) 'University of Michigan North Campus Long-Term Vision and Lidar Dataset'. *The International Journal of Robotics Research* [online] 35 (9), 1023–1035. available from <<http://www.deepdyve.com/lp/sage/university-of-michigan-north-campus-long-term-vision-and-lidar-dataset-Rlf7v6LUr0>>
- Caruso, D., Engel, J., and Cremers, D. (2015) 'Large-Scale Direct SLAM for Omnidirectional Cameras'. *IEEE International Conference on Intelligent Robots and Systems* 2015-December, 141–148
- Chebrolu, N., Lottes, P., Schaefer, A., Winterhalter, W., Burgard, W., and Stachniss, C. (2017) 'Agricultural Robot Dataset for Plant Classification, Localization and Mapping on Sugar Beet Fields'. *International Journal of Robotics Research* 36 (10), 1045–1052
- Chen, C., Lu, X., Markham, A., and Trigoni, N. (2018a) *IONet: Learning to Cure the Curse of Drift in Inertial Odometry*. [online] 6468–6476. available from <<http://arxiv.org/abs/1802.02209>>
- Chen, C., Zhao, P., Lu, C.X., Wang, W., Markham, A., and Trigoni, N. (2018b) *OxIOD: The Dataset for Deep Inertial Odometry*. available from <<https://onikle.com/articles/24653>>
- Chen, D.M., Baatz, G., Köser, K., Tsai, S.S., Vedantham, R., Pylvänäinen, T., Roimela, K., Chen, X., Bach, J., Pollefeys, M., Girod, B., and Grzeszczuk, R. (2011) 'City-Scale Landmark Identification on Mobile Devices'. *Proceedings of the IEEE Computer Society Conference on Computer Vision and Pattern Recognition* 737–744
- Chen, G. (1992) 'Introduction to Random Signals and Applied Kalman Filtering (Second Edition),

- Robert Grover Brown and Patrick Y. C. Hwang, John Wiley, New York, 1992, 512 p.p., ISBN 0-47152-573-1, \$62.95'. *International Journal of Robust and Nonlinear Control* [online] 2 (3), 240–242. available from
<<https://onlinelibrary.wiley.com/doi/full/10.1002/rnc.4590020307>> [31 May 2021]
- Cheng, Y., Wang, D., Zhou, P., and Zhang, T. (2017) *A Survey of Model Compression and Acceleration for Deep Neural Networks*. [online] 1–10. available from
<<http://arxiv.org/abs/1710.09282>>
- Chiang, K.-W. (2003) *The Utilization of Single Point Positioning and Multi-Layers Feed-Forward Network for INS/GPS Integration*. 258–266. available from
<<https://www.ion.org/publications/abstract.cfm?articleID=5201>> [5 June 2019]
- Chiang, K.-W. and El-Sheimy, N. (2002) *INS/GPS Integration Using Neural Networks for Land Vehicle Navigation Applications*. 535–544. available from
<<https://www.ion.org/publications/abstract.cfm?articleID=2055>> [5 June 2019]
- Chiang, K. (2004) *INS / GPS Integration Using Neural Networks for Land Vehicular Navigation UCGE Reports Number 20209 Department of Geomatics Engineering INS / GPS Integration Using Neural Networks for Land Vehicular Navigation Applications by Kai-Wei Chiang*. (April)
- Chiang, K.W., Noureldin, A., and El-Sheimy, N. (2008) 'Constructive Neural-Networks-Based MEMS/GPS Integration Scheme'. *IEEE Transactions on Aerospace and Electronic Systems* 44 (2), 582–594
- Cho, K., Van Merriënboer, B., Gulcehre, C., Bahdanau, D., Bougares, F., Schwenk, H., and Bengio, Y. (2014) 'Learning Phrase Representations Using RNN Encoder-Decoder for Statistical Machine Translation'. in *EMNLP 2014 - 2014 Conference on Empirical Methods in Natural Language Processing, Proceedings of the Conference*. held 3 June 2014. Association for Computational Linguistics (ACL), 1724–1734
- Choi, S., Zhou, Q.Y., and Koltun, V. (2015) 'Robust Reconstruction of Indoor Scenes'. *Proceedings of the IEEE Computer Society Conference on Computer Vision and Pattern Recognition* 07-12-June-2015, 5556–5565
- Choi, Y., Kim, N., Hwang, S., Park, K., Yoon, J.S., An, K., and Kweon, I.S. (2018) *KAIST Multi-Spectral Day/Night Data Set for Autonomous and Assisted Driving*. [online] available from
<http://www.ieee.org/publications_standards/publications/rights/index.html>
- Cordts, M., Omran, M., Ramos, S., Rehfeld, T., Enzweiler, M., Benenson, R., Franke, U., Roth, S.,

- and Schiele, B. (2016) 'The Cityscapes Dataset for Semantic Urban Scene Understanding'. *Proceedings of the IEEE Computer Society Conference on Computer Vision and Pattern Recognition* 2016-December, 3213–3223
- Cummins, M., Newman, P., and Newman, M.C.P. (2008) 'FAB-MAP: Probabilistic Localization and Mapping in the Space of Appearance'. *The International Journal of Robotics Research* 27
- Dai, H. fa, Bian, H. wei, Wang, R. ying, and Ma, H. (2019) 'An INS/GNSS Integrated Navigation in GNSS Denied Environment Using Recurrent Neural Network'. *Defence Technology*
- Delmerico, J., Cieslewski, T., Rebecq, H., Faessler, M., and Scaramuzza, D. (2019) 'Are We Ready for Autonomous Drone Racing? The UZH-FPV Drone Racing Dataset'. in *IEEE International Conference on Robotics and Automation (ICRA)* [online] held 2019. available from <<http://rpg.ifi.uzh.ch>>
- Domke, C. (2020) *LiDARs for Self-Driving Vehicles: A Technological Arms Race | Automotive World*. available from <<https://www.automotiveworld.com/articles/lidars-for-self-driving-vehicles-a-technological-arms-race/>>
- Dowd, I. (2019) *The Future of Autonomous Vehicles*. [online] available from <<https://www.openaccessgovernment.org/future-of-autonomous-vehicles/57772/>> [4 June 2019]
- El-Moneim, S.A., Nassar, M.A., Dessouky, M.I., Ismail, N.A., El-Fishawy, A.S., and Abd El-Samie, F.E. (2020) 'Text-Independent Speaker Recognition Using LSTM-RNN and Speech Enhancement'. *Multimedia Tools and Applications* [online] 79 (33–34), 24013–24028. available from <<https://link.springer.com/article/10.1007/s11042-019-08293-7>> [30 January 2021]
- Engel, J., Usenko, V., and Cremers, D. (2016) *A Photometrically Calibrated Benchmark For Monocular Visual Odometry*. [online] available from <<https://arxiv.org/abs/1607.02555v2>>
- Fang, W., Jiang, J., Lu, S., Gong, Y., Tao, Y., Tang, Y., Yan, P., Luo, H., and Liu, J. (2020) 'A LSTM Algorithm Estimating Pseudo Measurements for Aiding INS during GNSS Signal Outages'. *Remote Sensing* [online] 12 (2), 256. available from <<https://www.mdpi.com/2072-4292/12/2/256>> [23 March 2020]
- Ferrera, M., Moras, J., Trouvé-Peloux, P., Creuze, V., and Dégez, D. (2018) *The Aqualoc Dataset: Towards Real-Time Underwater Localization from a Visual-Inertial-Pressure Acquisition*

- System*. [online] available from <<http://arxiv.org/abs/1809.07076>>
- Furgale, P., Carle, P., Enright, J., and Barfoot, T.D. (2012) 'The Devon Island Rover Navigation Dataset': [Http://Dx.Doi.Org/10.1177/0278364911433135](http://Dx.Doi.Org/10.1177/0278364911433135) [online] 31 (6), 707–713. available from <<https://journals.sagepub.com/doi/10.1177/0278364911433135>>
- Gardner, M.W. and Dorling, S.R. (1998) 'Artificial Neural Networks (the Multilayer Perceptron) - a Review of Applications in the Atmospheric Sciences'. *Atmospheric Environment* 32 (14–15), 2627–2636
- Geiger, A., Lenz, P., Stiller, C., and Urtasun, R. (2013) 'Vision Meets Robotics: The KITTI Dataset': [Http://Dx.Doi.Org/10.1177/0278364913491297](http://Dx.Doi.Org/10.1177/0278364913491297) [online] 32 (11), 1231–1237. available from <<https://journals.sagepub.com/doi/full/10.1177/0278364913491297>>
- Gerard O'Dwyer (2018) *Finland, Norway Press Russia on Suspected GPS Jamming during NATO Drill* [online] available from <<https://www.defensenews.com/global/europe/2018/11/16/finland-norway-press-russia-on-suspected-gps-jamming-during-nato-drill/>> [4 June 2019]
- Gers, F.A., Schmidhuber, J., and Cummins, F. (2000) 'Learning to Forget: Continual Prediction with LSTM'. *Neural Computation* 12 (10), 2451–2471
- Glover, A.J., Maddern, W.P., Milford, M.J., and Wyeth, G.F. (2010) 'FAB-MAP + RatSLAM: Appearance-Based SLAM for Multiple Times of Day'. *Proceedings - IEEE International Conference on Robotics and Automation* 3507–3512
- Graves, A. and Schmidhuber, J. (2005) 'Framewise Phoneme Classification with Bidirectional LSTM and Other Neural Network Architectures'. in *Neural Networks*. held 1 July 2005. Pergamon, 602–610
- Griffith, S., Chahine, G., and Pradalier, C. (2017) 'Symphony Lake Dataset': [Https://Doi.Org/10.1177/0278364917730606](https://doi.org/10.1177/0278364917730606) [online] 36 (11), 1151–1158. available from <<https://journals.sagepub.com/doi/full/10.1177/0278364917730606>>
- Guzmán, R., Hayet, J.B., and Klette, R. (2015) 'Towards Ubiquitous Autonomous Driving: The CCSAD Dataset'. *Lecture Notes in Computer Science (Including Subseries Lecture Notes in Artificial Intelligence and Lecture Notes in Bioinformatics)* 9256, 582–593
- Handa, A., Whelan, T., McDonald, J., and Davison, A.J. (2014) 'A Benchmark for RGB-D Visual Odometry, 3D Reconstruction and SLAM'. in *IEEE International Conference on Robotics and Automation (ICRA)* [online] held 2014. available from <<http://www.povray.org/>>

- Hess, W., Kohler, D., Rapp, H., and Andor, D. (2016) 'Real-Time Loop Closure in 2D LIDAR SLAM'. *Proceedings - IEEE International Conference on Robotics and Automation* 2016-June, 1271–1278
- Hewitt, R.A., Boukas, E., Azkarate, M., Pagnamenta, M., Marshall, J.A., Gasteratos, A., and Visentin, G. (2017) 'The Katwijk Beach Planetary Rover Dataset': <https://doi.org/10.1177/0278364917737153> [online] 37 (1), 3–12. available from <<https://journals.sagepub.com/doi/10.1177/0278364917737153>>
- Hochreiter, S. and Schmidhuber, J. (1997) 'Long Short-Term Memory'. *Neural Computation* [online] 9 (8), 1735–1780. available from <<http://www.mitpressjournals.org/doi/10.1162/neco.1997.9.8.1735>>
- Huang, A.S., Antone, M., Olson, E., Fletcher, L., Moore, D., Teller, S., and Leonard, J. (2010) 'A High-Rate, Heterogeneous Data Set from the DARPA Urban Challenge'. *International Journal of Robotics Research* 29 (13), 1595–1601
- Huang, Z., Zhu, J., Yang, L., Xue, B., ... J.W.-I. transactions on, and 2015, U. (2015) 'Accurate 3-D Position and Orientation Method for Indoor Mobile Robot Navigation Based on Photoelectric Scanning'. *Ieeexplore.Ieee.Org* [online] available from <<https://ieeexplore.ieee.org/abstract/document/7084100/>> [15 February 2021]
- Jekeli, C. (2012) *Inertial Navigation Systems with Geodetic Applications*. De Gruyter
- Jeong, J., Cho, Y., Shin, Y.-S., Roh, H., and Kim, A. (2018) 'Complex Urban LiDAR Data Set'. *Proceedings - IEEE International Conference on Robotics and Automation* [online] 6344–6351. available from <<https://arxiv.org/abs/1803.06121v1>>
- Jialin Pan, S., Kwok, J.T., Yang, Q., and Junfeng Pan, J. (2007) *Adaptive Localization in a Dynamic WiFi Environment Through Multi-View Learning* * [online] available from <www.aaai.org> [15 June 2021]
- Jung, H., Oto, Y., Mozos, O.M., Iwashita, Y., and Kurazume, R. (2016) 'Multi-Modal Panoramic 3D Outdoor Datasets for Place Categorization'. in *International Conference on Intelligent Robots and Systems (IROS)*. held 2016
- Kok, M., Hol, J.D., and Schön, T.B. (2017) 'Using Inertial Sensors for Position and Orientation Estimation'. *Foundations and Trends in Signal Processing* [online] 11 (2), 1–153. available from <<http://dx.doi.org/10.1561/20000000094>> [20 January 2020]
- Krizhevsky, A., Sutskever, I., and Hinton, G.E. (2012) *ImageNet Classification with Deep*

- Convolutional Neural Networks* [online] available from <<http://code.google.com/p/cuda-convnet/>> [26 February 2020]
- Kuhlmann, G. and Stone, P. (2007) 'Graph-Based Domain Mapping for Transfer Learning in General Games'. in *Lecture Notes in Computer Science (Including Subseries Lecture Notes in Artificial Intelligence and Lecture Notes in Bioinformatics)* [online] held 2007. Springer Verlag, 188–200. available from <https://link.springer.com/chapter/10.1007/978-3-540-74958-5_20> [15 June 2021]
- Lee Teschler (2018) *Inertial Measurement Units Will Keep Self-Driving Cars on Track* [online] available from <<https://www.microcontrollertips.com/inertial-measurement-units-will-keep-self-driving-cars-on-track-faq/>> [5 June 2019]
- Leung, K.Y.K., Halpern, Y., Barfoot, T.D., and Liu, H.H.T. (2011) 'The UTIAS Multi-Robot Cooperative Localization and Mapping Dataset'. *International Journal of Robotics Research* 30 (8), 969–974
- Li, W., Saeedi, S., McCormac, J., Clark, R., Tzoumanikas, D., Ye, Q., Huang, Y., Tang, R., and Leutenegger, S. (2018) *InteriorNet: Mega-Scale Multi-Sensor Photo-Realistic Indoor Scenes Dataset*. available from <<https://onikle.com/articles/25041>>
- Ling, X., Xue, G.R., Dai, W., Jiang, Y., Yang, Q., and Yu, Y. (2008) 'Can Chinese Web Pages Be Classified with English Data'. in *Proceeding of the 17th International Conference on World Wide Web 2008, WWW'08*. held 2008. 969–978
- Liu, P., Yang, R., and Xu, Z. (2019) 'How Safe Is Safe Enough for Self-Driving Vehicles?' *Risk Analysis* [online] 39 (2), 315–325. available from <<http://doi.wiley.com/10.1111/risa.13116>> [4 June 2019]
- Maddern, W., Pascoe, G., Linegar, C., and Newman, P. (2016) '1 Year, 1000 Km: The Oxford RobotCar Dataset': *Http://Dx.Doi.Org/10.1177/0278364916679498* [online] 36 (1), 3–15. available from <<https://journals.sagepub.com/doi/abs/10.1177/0278364916679498>>
- Mahmoud, H. and Akkari, N. (2016) 'Shortest Path Calculation: A Comparative Study for Location-Based Recommender System'. in *Proceedings - 2016 World Symposium on Computer Applications and Research, WSCAR 2016*. held 19 December 2016. Institute of Electrical and Electronics Engineers Inc., 1–5
- Majdik, A.L., Till, C., and Scaramuzza, D. (2017) 'The Zurich Urban Micro Aerial Vehicle Dataset': *Http://Dx.Doi.Org/10.1177/0278364917702237* [online] 36 (3), 269–273. available from <<https://journals.sagepub.com/doi/full/10.1177/0278364917702237>>

-
- Malleswaran, M., Vaidehi, V., Saravanaselvan, A., and Mohankumar, M. (2013) 'Performance Analysis of Various Artificial Intelligent Neural Networks for GPS/INS Integration'. *Applied Artificial Intelligence* 27 (5), 367–407
- Mallios, A., Vidal, E., Campos, R., and Carreras, M. (2017) 'Underwater Caves Sonar Data Set': <https://doi.org/10.1177/0278364917732838> [online] 36 (12), 1247–1251. available from <<https://journals.sagepub.com/doi/10.1177/0278364917732838>>
- Mao, W., Wang, M., Sun, W., Qiu, L., Pradhan, S., and Chen, Y.-C. (2019) 'RNN-Based Room Scale Hand Motion Tracking'. in *The 25th Annual International Conference on Mobile Computing and Networking* [online] held 11 October 2019 at New York, NY, USA. Association for Computing Machinery (ACM), 1–16. available from <<https://dl.acm.org/doi/10.1145/3300061.3345439>> [30 January 2021]
- Mccormac, J., Handa, A., Leutenegger, S., and Davison, A.J. (2017) 'SceneNet RGB-D: 5M Photorealistic Images of Synthetic Indoor Trajectories with Ground Truth'. in *The IEEE International Conference on Computer Vision (ICCV)* [online] held 2017. available from <<http://robotvault.>>
- Merriaux, P., Dupuis, Y., Vasseur, P., and Savatier, X. (2014) 'Wheel Odometry-Based Car Localization and Tracking on Vectorial Map (Extended Abstract)'. in *2014 IEEE 17th International Conference on Intelligent Transportation Systems (ITSC) October 8-11, 2014. Qingdao, China* [online] held 2014 at Qingdao, China. IEEE. available from <<https://ieeexplore.ieee.org/stamp/stamp.jsp?tp=&arnumber=6957971>> [16 July 2020]
- Milford, M.J. and Wyeth, G.F. (2012) 'SeqSLAM: Visual Route-Based Navigation for Sunny Summer Days and Stormy Winter Nights'. *Proceedings - IEEE International Conference on Robotics and Automation* 1643–1649
- Miller, M., Chung, S.-J., and Hutchinson, S. (2018) 'The Visual-Inertial Canoe Dataset': <https://doi.org/10.1177/0278364917751842> [online] 37 (1), 13–20. available from <<https://journals.sagepub.com/doi/full/10.1177/0278364917751842>>
- Mueggler, E., Rebecq, H., Gallego, G., Delbruck, T., and Scaramuzza, D. (2017) *The Event-Camera Dataset and Simulator: Event-Based Data for Pose Estimation, Visual Odometry, and SLAM*. [online] available from <http://rpg.ifi.uzh.ch/davis_data.html>
- Noureldin, A., El-Shafie, A., and Bayoumi, M. (2011) 'GPS/INS Integration Utilizing Dynamic Neural Networks for Vehicular Navigation'. *Information Fusion* [online] 12 (1), 48–57. available from <<http://dx.doi.org/10.1016/j.inffus.2010.01.003>>

-
- NovAtel (2014) 'IMU Errors and Their Effects'. *Apn-064* [online] (Rev A), 1–6. available from <<http://www.novatel.com/assets/Documents/Bulletins/APN064.pdf>>
- Nwe, T.L., Dat, T.H., and Ma, B. (2018) 'Convolutional Neural Network with Multi-Task Learning Scheme for Acoustic Scene Classification'. in *Proceedings - 9th Asia-Pacific Signal and Information Processing Association Annual Summit and Conference, APSIPA ASC 2017*. held 5 February 2018. Institute of Electrical and Electronics Engineers Inc., 1347–1350
- Nweke, H.F., Teh, Y.W., Al-garadi, M.A., and Alo, U.R. (2018) 'Deep Learning Algorithms for Human Activity Recognition Using Mobile and Wearable Sensor Networks: State of the Art and Research Challenges'. in *Expert Systems with Applications*. vol. 105. Elsevier Ltd, 233–261
- Oettershagen, P., Stastny, T., Mantel, T., Melzer, A., Rudin, K., Gohl, P., Agamennoni, G., Alexis, K., and Siegwart, R. (2016) 'Long-Endurance Sensing and Mapping Using a Hand-Launchable Solar-Powered UAV'. *Field and Service Robotics : Results of the 10th International Conference* [online] 113, 441–454. available from <<https://doi.org/10.3929/ethz-a-010585180>>
- Onda, K., Oishi, T., and Kuroda, Y. (2018) 'Dynamic Environment Recognition for Autonomous Navigation with Wide FOV 3D-LiDAR'. *IFAC-PapersOnLine* 51 (22), 530–535
- Onyekpe, U., Kanarachos, S., Palade, V., and Christopoulos, S.-R.G. (2020a) 'Learning Uncertainties in Wheel Odometry for Vehicular Localisation in GNSS Deprived Environments'. in *International Conference on Machine Learning Applications (ICMLA)* [online] held December 2020. IEEE, 741–746. available from <https://www.researchgate.net/publication/344565188_Learning_Uncertainties_in_Wheel_Odometry_for_Vehicular_Localisation_in_GNSS_Deprived_Environments> [25 February 2021]
- Onyekpe, U., Kanarachos, S., Palade, V., and Christopoulos, S.-R.G. (2020b) 'Vehicular Localisation at High and Low Estimation Rates during GNSS Outages : A Deep Learning Approach'. in *In: Wani M.A., Khoshgoftaar T.M., Palade V. (Eds) Deep Learning Applications, Volume 2. Advances in Intelligent Systems and Computing, Vol 1232*. ed. by M. Arif Wani, Taghi Khoshgoftaar, V.P. Springer Singapore, 229–248
- Onyekpe, U., Palade, V., Herath, A., Kanarachos, S., and Fitzpatrick, M.E. (2021a) 'WhONet: Wheel Odometry Neural Network for Vehicular Localisation in GNSS-Deprived Environments'. *Engineering Applications of Artificial Intelligence* 105, 104421

-
- Onyekpe, U., Palade, V., and Kanarachos, S. (2020) *Learning to Localise Automated Vehicles in Challenging Environments Using Inertial Navigation Systems (INS)*. [online] available from <<http://arxiv.org/abs/2010.02363>> [9 October 2020]
- Onyekpe, U., Palade, V., Kanarachos, S., and Christopoulos, S.-R.G. (2021b) 'A Quaternion Gated Recurrent Unit Neural Network for Sensor Fusion'. *Information* [online] 12 (3), 117. available from <<https://www.mdpi.com/2078-2489/12/3/117>> [14 March 2021]
- Onyekpe, U., Palade, V., Kanarachos, S., and Szkolnik, A. (2021c) 'IO-VNBD: Inertial and Odometry Benchmark Dataset for Ground Vehicle Positioning'. *Data in Brief* 35, 106885
- Ouzz, O. (2019) *Ford Fiesta Interior Dimensions - Our Houzz* [online] available from <<http://ourhouzz.site/ford-fiesta-interior-dimensions>> [26 February 2020]
- OXTS (2016) *Why Integrate an INS with Imaging Systems on an Autonomous Vehicle* [online] available from <<https://www.oxts.com/technical-notes/why-use-ins-with-autonomous-vehicle/>> [4 June 2019]
- Pan, S.J., Shen, D., Yang, Q., and Kwok, J.T. (2008) *Transferring Localization Models Across Space* [online] available from <www.aaai.org> [15 June 2021]
- Pan, S.J. and Yang, Q. (2009) *A Survey on Transfer Learning*. [online] available from <<http://socrates.acadiau.ca/courses/comp/dsilver/NIPS95>> [15 June 2021]
- Pandey, G., McBride, J.R., and Eustice, R.M. (2011) 'Ford Campus Vision and Lidar Data Set'. *The International Journal of Robotics Research (IJRR)*
- Papadoulis, A., Quddus, M., and Imprialou, M. (2019) 'Evaluating the Safety Impact of Connected and Autonomous Vehicles on Motorways'. *Accident Analysis and Prevention* 124, 12–22
- Peynot, T., Scheduling, S., and Terho, S. (2010) 'The Marulan Data Sets: Multi-Sensor Perception in a Natural Environment with Challenging Conditions': *Http://Dx.Doi.Org/10.1177/0278364910384638* [online] 29 (13), 1602–1607. available from <<https://journals.sagepub.com/doi/10.1177/0278364910384638>>
- Pietrzak, M. (2016) *Vincenty · PyPI* [online] available from <<https://pypi.org/project/vincenty/>> [12 April 2019]
- Pire, T., Mujica, M., Civera, J., and Kofman, E. (2018) 'The Rosario Dataset: Multisensor Data for Localization and Mapping in Agricultural Environments'. *International Journal of Robotics Research* [online] 38 (6), 633–641. available from <<https://arxiv.org/abs/1809.06413v2>>

- Pomerleau, F., Liu, M., Colas, F., and Siegwart, R. (2012) 'Challenging Data Sets for Point Cloud Registration Algorithms'. *The International Journal of Robotics Research* [online] (14), 1705–1711. available from <<https://hal.archives-ouvertes.fr/hal-01143454>>
- Pronobis, A. and Caputo, B. (2009) 'COLD: The CoSy Localization Database': [Http://Dx.Doi.Org/10.1177/0278364909103912](http://Dx.Doi.Org/10.1177/0278364909103912) [online] 28 (5), 588–594. available from <<https://journals.sagepub.com/doi/abs/10.1177/0278364909103912>>
- Purohit, H., Tanabe, R., Ichige, K., Endo, T., Nikaido, Y., Suefusa, K., and Kawaguchi, Y. (2019) 'MIMII Dataset: Sound Dataset for Malfunctioning Industrial Machine Investigation and Inspection'. *ArXiv* [online] available from <<http://arxiv.org/abs/1909.09347>> [30 January 2021]
- Rajkomar, A., Oren, E., Chen, K., Dai, A.M., Hajaj, N., Hardt, M., Liu, P.J., Liu, X., Marcus, J., Sun, M., Sundberg, P., Yee, H., Zhang, K., Zhang, Y., Flores, G., Duggan, G.E., Irvine, J., Le, Q., Litsch, K., Mossin, A., Tansuwan, J., Wang, D., Wexler, J., Wilson, J., Ludwig, D., Volchenboun, S.L., Chou, K., Pearson, M., Madabushi, S., Shah, N.H., Butte, A.J., Howell, M.D., Cui, C., Corrado, G.S., and Dean, J. (2018) 'Scalable and Accurate Deep Learning with Electronic Health Records'. *Npj Digital Med* [online] 1 (1), 18. available from <www.nature.com/npjdigitalmed> [25 February 2021]
- Redmon, J., Divvala, S., Girshick, R., and Farhadi, A. (2015) *You Only Look Once: Unified, Real-Time Object Detection* [online] available from <<https://goo.gl/bEs6Cj>> [11 May 2020]
- Russell, S. and Norvig, P. (2010) 'Artificial Intelligence: A Modern Approach' [online] 4th edn. available from <<https://www.pearson.com/us/higher-education/program/Russell-Artificial-Intelligence-A-Modern-Approach-4th-Edition/PGM1263338.html>> [8 November 2021]
- Salychev, O.S., Voronov, V.V., Cannon, M.E., Nayak, R., and Lachapelle, G. (2000) *Low Cost INS/GPS Integration: Concepts and Testing*. 98–105. available from <<http://www.ion.org/publications/abstract.cfm?jp=p&articleID=11>> [31 May 2021]
- Saraee, E., Jalal, M., and Betke, M. (2018) *SAVOIAS: A Diverse, Multi-Category Visual Complexity Dataset*. [online] available from <<https://www.bu.edu/cs/ivc/>>
- Schubert, D., Goll, T., Demmel, N., Usenko, V., Stückler, J., and Cremers, D. (2018) 'The TUM VI Benchmark for Evaluating Visual-Inertial Odometry'. *IEEE International Conference on Intelligent Robots and Systems* [online] 1680–1687. available from <<https://arxiv.org/abs/1804.06120v3>>
- Senturk, U., Yucedag, I., and Polat, K. (2018) 'Repetitive Neural Network (RNN) Based Blood Pressure Estimation Using PPG and ECG Signals'. in *ISMSIT 2018 - 2nd International Symposium on Multidisciplinary Studies and Innovative Technologies, Proceedings*. held 6 December 2018. Institute of Electrical and Electronics Engineers Inc.

- Shan, Z., Li, R., and Schwertfeger, S. (2019) 'RGBD-Inertial Trajectory Estimation and Mapping for Ground Robots'. *Sensors (Switzerland)* 19 (10)
- Sharaf, R., Noureldin, A., Osman, A., and El-Sheimy, N. (2005) 'Online INS/GPS Integration with a Radial Basis Function Neural Network'. *IEEE Aerospace and Electronic Systems Magazine* 20 (3), 8–14
- Shi, X., Fan, W., and Ren, J. (2008) 'Actively Transfer Domain Knowledge'. in *Lecture Notes in Computer Science (Including Subseries Lecture Notes in Artificial Intelligence and Lecture Notes in Bioinformatics)* [online] held 2008. Springer, Berlin, Heidelberg, 342–357. available from <https://link.springer.com/chapter/10.1007/978-3-540-87481-2_23> [15 June 2021]
- Shotton, J., Glocker, B., Zach, C., Izadi, S., Criminisi, A., and Fitzgibbon, A. (2013) *Scene Coordinate Regression Forests for Camera Relocalization in RGB-D Images*. available from <<https://www.microsoft.com/en-us/research/publication/scene-coordinate-regression-forests-for-camera-relocalization-in-rgb-d-images/>>
- Simons-Morton, B.G., Ouimet, M.C., Wang, J., Klauer, S.G., Lee, S.E., and Dingus, T.A. (2009) 'Hard Braking Events Among Novice Teenage Drivers By Passenger Characteristics'. in *Proceedings of the ... International Driving Symposium on Human Factors in Driver Assessment, Training, and Vehicle Design* [online] held 2009. The University of Iowa, 236–242. available from <[pmc/articles/PMC3019610/?report=abstract](https://pubmed.ncbi.nlm.nih.gov/19610/)> [16 July 2020]
- Smith, M., Baldwin, I., Churchill, W., Paul, R., and Newman, P. (2009) 'The New College Vision and Laser Data Set'. *The International Journal of Robotics Research* 28
- Sturm, J., Engelhard, N., Endres, F., Burgard, W., and Cremers, D. (2012) 'A Benchmark for the Evaluation of RGB-D SLAM Systems'. in *Conference on Intelligent Robots and Systems* [online] held 2012. 573–580. available from <<http://vision.in.tum.de/data/datasets/>>
- Susto, G.A., Cenedese, A., and Terzi, M. (2018) 'Time-Series Classification Methods: Review and Applications to Power Systems Data'. in *Big Data Application in Power Systems*. Elsevier, 179–220
- Templeton, B. (2017) *Cameras or Lasers?* [online] available from <<http://www.templetons.com/brad/robocars/cameras-lasers.html>> [4 June 2019]
- Thomas, C.M. and Featherstone, W.E. (2005) 'Validation of Vincenty's Formulas for the Geodesic Using a New Fourth-Order Extension of Kivioja's Formula'. *Journal of Surveying Engineering* [online] 131 (1), 20–26. available from

- <<http://ascelibrary.org/doi/10.1061/%28ASCE%290733-9453%282005%29131%3A1%2820%29>> [18 March 2020]
- Tong, C.H., Gingras, D., Larose, K., Barfoot, T.D., and Dupuis, É. (2013) 'The Canadian Planetary Emulation Terrain 3D Mapping Dataset': <Http://Dx.Doi.Org/10.1177/0278364913478897> [online] 32 (4), 389–395. available from <<https://journals.sagepub.com/doi/abs/10.1177/0278364913478897>>
- Tsang, G., Deng, J., and Xie, X. (2018) 'Recurrent Neural Networks for Financial Time-Series Modelling'. in *Proceedings - International Conference on Pattern Recognition*. held 26 November 2018. Institute of Electrical and Electronics Engineers Inc., 892–897
- U.S. Department of Transportation, N.H.T.S.A. (2009) *Comparing Real-World Behaviors of Drivers With High versus Low Rates of Crashes and Near-Crashes*.
- VBOX Video HD2 (2019) available from <<https://www.vboxmotorsport.co.uk/index.php/en/products/video-loggers/vbox-video>> [26 February 2020]
- Vincenty, T. (1975) 'Direct and Inverse Solutions of Geodesics on the Ellipsoid with Application of Nested Equations'. *Survey Review* 23 (176), 88–93
- Wang, J., Chen, Y., Hao, S., Peng, X., and Hu, L. (2019) 'Deep Learning for Sensor-Based Activity Recognition: A Survey'. *Pattern Recognition Letters* 119, 3–11
- Warren, M., McKinnon, D., He, H., Glover, A., Shiel, M., and Upcroft, B. (2014) 'Large Scale Monocular Vision-Only Mapping from a Fixed-Wing SUAS'. *Springer Tracts in Advanced Robotics* [online] 92, 495–509. available from <https://link.springer.com/chapter/10.1007/978-3-642-40686-7_33>
- Warren, M., McKinnon, D., He, H., and Upcroft, B. (2010) 'Unaided Stereo Vision Based Pose Estimation'. *Australasian Conference on Robotics and Automation*
- Wasenmuller, O., Meyer, M., and Stricker, D. (2016) 'CoRBS: Comprehensive RGB-D Benchmark for SLAM Using Kinect V2'. *2016 IEEE Winter Conference on Applications of Computer Vision, WACV 2016*
- Weber, Y. and Kanarachos, S. (2020) 'CUPAC – The Coventry University Public Road Dataset for Automated Cars'. *Data in Brief* 28, 104950
- Wenchen Zheng, V., Jialin Pan, S., Yang, Q., and Junfeng Pan, J. (2008) *Transferring Multi-Device Localization Models Using Latent Multi-Task Learning* * [online] available from

- <www.aaai.org> [15 June 2021]
- Yang, Q., Pan, J., and Zheng, V.W. (2008) *Estimating Location Using Wi-Fi Estimating Location Using Wi-Fi Task 2 Evaluation Criterion* [online] available from <www.cs.ust.hk> [15 June 2021]
- Yang, S.-W., Wang, C.-C., and Thorpe, C. (2011) 'The Annotated Laser Data Set for Navigation in Urban Areas': [Http://Dx.Doi.Org/10.1177/0278364910389840](http://dx.doi.org/10.1177/0278364910389840) [online] 30 (9), 1095–1099. available from <<https://journals.sagepub.com/doi/abs/10.1177/0278364910389840>>
- Yao, W., Zhou, D., Zhan, L., Liu, Yong, Cui, Y., You, S., and Liu, Yilu (2017) 'GPS Signal Loss in the Wide Area Monitoring System: Prevalence, Impact, and Solution'. *Electric Power Systems Research* [online] 147 (C), 254–262. available from <<https://linkinghub.elsevier.com/retrieve/pii/S0378779617300950>> [5 June 2019]
- Yin, J., Yang, Q., and Ni, L. (2005) 'Adaptive Temporal Radio Maps for Indoor Location Estimation'. in *Proceedings - Third IEEE International Conference on Pervasive Computing and Communications, PerCom 2005*. held 2005. 85–94
- Zeller, N., Quint, F., and Stilla, U. (2018) *A Synchronized Stereo and Plenoptic Visual Odometry Dataset*. [online] available from <<https://arxiv.org/abs/1807.09372v2>>
- Zheng, V.W., Xiang, E.W., Yang, Q., and Shen, D. (2008) *Transferring Localization Models Over Time* * [online] available from <www.aaai.org> [15 June 2021]
- Zhu, A.Z., Thakur, D., Ozaslan, T., Pfrommer, B., Kumar, V., and Daniilidis, K. (2018) *The Multi Vehicle Stereo Event Camera Dataset: An Event Camera Dataset for 3D Perception*. [online] (1). available from <<http://velodynelidar.com/vlp-16-lite.html>>
- Zhuo, H., Yang, Q., Hu, D.H., and Li, L. (2008) 'Transferring Knowledge from Another Domain for Learning Action Models'. in *Lecture Notes in Computer Science (Including Subseries Lecture Notes in Artificial Intelligence and Lecture Notes in Bioinformatics)* [online] held 15 December 2008. Springer, Berlin, Heidelberg, 1110–1115. available from <https://link.springer.com/chapter/10.1007/978-3-540-89197-0_115> [15 June 2021]

Appendix A

Table A1. Existing odometry datasets

Shortname and References	Configuration		Sensor Information						
	Platform, Environment		Pose	IMU	GPS	Labels	Lidar	Images	Other
IO-VNBD (Onyekpe, Palade, Kanarachos, & Szkolnik, 2021)	Veh	Urban	O	O	O	O			Wheel Encoder, Smartphone, Temperature sensor, Steering Angle, Brake pressure, Accelerometer Pedal position, etc.
FMDataset (Shan, Li, & Schwertfeger, 2019)	Hand	Indoor		O				O	
UZH-FPV Drone Racing (Delmerico, Cieslewski, Rebecq, Faessler, & Scaramuzza, 2019)	UAV	Indoor, Outdoor	O	O				O	
ADVIO Dataset (Saraee, Jalal, & Betke, 2018)	Hand	Urban	O	O				O	iPhone, Tango, Pixel
DeepIO Dataset (C. Chen et al., 2018)	Hand	Indoor	O	O					
Aqualoc Dataset (Ferrera, Moras, Trouvé-Peloux, Creuze, & Dégez, 2018)	ROV	Underwater	O	O				O	Pressure Sensor

Rosario Dataset (Pire, Mujica, Civera, & Kofman, 2018)	Mob	Terrain	O	O	O		O	Encoder
InteriorNet (Li et al., 2018)	Hand	Indoor	O	O		O	O	Texture, Lighting, Context, Optical Flow
SPO Dataset (Zeller, Quint, & Stilla, 2018)	Hand	Urban	O	O			O	Plenoptic Camera
KAIST Day/Night (Y. Choi et al., 2018)	Veh	Urban	O	O	O	O	O	Thermal Camera
TUM-Visual-Inertial (Schubert et al., 2018)	Hand	Indoor,Urban	O	O			O	
Complex Urban (Jeong, Cho, Shin, Roh, & Kim, 2018)	Veh	Urban	O	O	O		O	Encoder
Multi Vech Event (Zhu et al., 2018)	Veh	Urban	O	O	O		O	O
VI Canoe (Miller, Chung, & Hutchinson, 2018)	USV	Terrain	O	O	O			O
RPG-event (Mueggler, Rebecq, Gallego, Delbruck, & Scaramuzza, 2017)	UAV/Hand	Indoor	O	O				O
Underwater Cave (Mallios, Vidal, Campos, & Carreras, 2017)	AUV	Underwater	O	O				O
Zurich Urban MAV (Majdik, Till, & Scaramuzza, 2017)	UAV	Urban	O	O	O			O
Chilean Underground (Leung, Halpern, Barfoot, & Liu, 2011)	Mob	Terrain(Underground)	O				O	O
SceneNet RGB-D (McCormac, Handa, Leutenegger, & Davison, 2017)	Hand	Indoor	O			O		O
Symphony Lake (Griffith, Chahine, & Pradalier, 2017)	USV	Terrain (Lake)		O	O		O	O
Agricultural Robot (Chebrolu et al., 2017)	Mob	Terrain	O		O	O	O	O

Beach Rover (Hewitt et al., 2017)	Mob	Terrain	O	O	O	O	O	Encoder
EuRoc (Burri et al., 2016)	UAV	Indoor	O	O			O	
TUM-MONO (Engel, Usenko, & Cremers, 2016)	Hand	Indoor, Urban					O	Photometric Calibration
Cityscape (Cordts et al., 2016)	Veh	Urban	O		O	O	O	
Solar-UAV (Oettershagen et al., 2016)	UAV	Terrain	O	O	O	O		
CoRBS (Wasenmuller, Meyer, & Stricker, 2016)	Hand	Indoor	O				O	O
Oxford-robotcar (Maddern, Pascoe, Linegar, & Newman, 2016)	Veh	Urban	O	O	O	O	O	
NCLT (Carlevaris-Bianco, Ushani, & Eustice, 2016)	Mob	Urban	O	O	O	O	O	FOG
MPO-Japan (Jung, Oto, Mozos, Iwashita, & Kurazume, 2016)	Veh	Urban, Terrain		O	O	O	O	FARO 3D
Cartographer (Hess, Kohler, Rapp, & Andor, 2016)	Hand	Indoor		O			O	O
CCSAD (Guzmán, Hayet, & Klette, 2015)	Veh	Urban		O	O		O	
TUM-Omni (Caruso, Engel, & Cremers, 2015)	Hand	Indoor, Urban	O					
Augmented ICL-NUIM (S. Choi, Zhou, & Koltun, 2015)	Hand	Indoor	O				O	
ICL-NUIM (Handa, Whelan, Mcdonald, & Davison, 2014)	Hand	Indoor	O				O	
MRPT-Malaga (Blanco-Claraco, Moreno-Dueñas, & González-Jiménez, 2013)	Veh	Urban		O	O	O	O	
KITTI (Geiger, Lenz, Stiller, & Urtasun, 2013)	Veh	Urban	O	O	O	O	O	O

Canadian Planetary (Tong, Gingras, Larose, Barfoot, & Dupuis, 2013)	Mob	Terrain	O	O	O		O	O	
Microsoft 7 Scenes (Shotton et al., 2013)	Hand	Indoor	O					O	
SeqSLAM (Milford & Wyeth, 2012)	Veh	Urban					O		O
ETH-challenging (Pomerleau, Liu, Colas, & Siegwart, 2012)	Hand	Urban, Terrain		O	O		O	O	
TUM-RGBD (Sturm, Engelhard, Endres, Burgard, & Cremers, 2012)	Hand/Mob	Indoor	O	O				O	
ASRL-Kagara-Airborn (Michael Warren et al., 2014)	UAV	Terrain		O	O			O	
Devon Island Rover (Furgale, Carle, Enright, & Barfoot, 2012)	Mob	Terrain	O		O			O	Sunsensor, Inclinometer
ACFR Marine (ACFR, 2016)	AUV	Underwater	O	O		O		O	
UTIAS Multi-Robot (Leung et al., 2011)	Mob	Urban	O			O			
Ford Campus (Pandey, McBride, & Eustice, 2011)	Veh	Urban	O	O	O		O	O	
San Francisco (D. M. Chen et al., 2011)	Veh	Urban	O	O	O	O	O	O	DMI
Annotated-Laser (Yang, Wang, & Thorpe, 2011)	Veh	Urban	O			O	O	O	
MIT-DARPA-Urban (Huang et al., 2010)	Veh	Urban	O	O	O	O	O	O	
St Lucia Stereo (M Warren, McKinnon, He, & Upcroft, 2010)	Veh	Urban		O	O			O	
St Lucia Multiple Times (Glover, Maddern, Milford, & Wyeth, 2010)	Veh	Urban			O			O	
Marulan (Peynot, Scheduling, & Terho, 2010)	Mob	Terrain	O	O	O		O	O	Infrared

COLD (Pronobis & Caputo, 2009)	Hand	Indoor	O		O	O	O
NewCollege (Smith, Baldwin, Churchill, Paul, & Newman, 2009)	Mob	Urban	O		O	O	O
Rawseeds-Indoor (Bonarini, Burgard, & Fontana, 2006)	Mob	Indoor	O	O		O	O
Rawseeds-Outdoor (Bonarini et al., 2006)	Mob	Urban	O	O	O	O	O
FABMAP (Cummins, Newman, & Newman, 2008)	Veh	Urban			O		O

Table A2-1. Dataset description from Driver A, B and C.

Driver	Dataset name	Features	Cities and towns covered	Weather conditions	Collection date	Velocity and acceleration range	Total time driven and distance covered	Total number of data points	Corresponding smartphone dataset
A	V-S1	B-road (B4101), roundabout (x9), reverse (x5), hilly road, A4053 (ring-road), hard-brake, tyre pressure E	Coventry	15 / 4 °C, Sunny, Humidity:73%, Wind:2.486 mph N	08/09/2019	0.0 to 93.8 km/hr, -0.59 to 0.34 g	86.3 mins, 38.16 km	51790	S-S1
	V-S2	B-road (B4112, B4065), roundabout (x18), reverse drive (x8), motorway, dirt road, u-turn (x5), country road, successive left-right turns, hard-brake, A-roads (A4600), tyre pressure E	Coventry, Nuneaton	17 / 15 °C Passing clouds. Humidity:47% Wind:3.728 mph N	08/09/2019	0.0 to 105.2 km/hr, -0.56 to 0.43 g	156.5 mins, 75.64 km	93900	S-S2
	V-S3a	Round-about (x15), u-turn/reverse drive (x4), motorway (M6), A-road (A4600, A426), hard-brake, swift maneuvers, country roads, change in speed, night-time, sharp turn left/right, tyre pressure E	Coventry, Rugby	17 / 12 °C, Passing clouds. Humidity:65% Wind:6.836 mph W	04/09/2019	0.0 - 98.0 km/hr, -0.57 to 0.4 g	41.1 mins, 26.0 km	24660	S-S3a
	V-S3b	Successive left-right turns (x21), reverse/u-turns (x1), tyre pressure – E	Rugby		04/09/2019	0.0 to 44.8 km/hr, -0.37 to 0.3 g	11.4 mins, 3.8 km	6840	S-S3b
	V-S3c	Roundabout(x4), A-road (A428), country roads, tyre pressure E	Rugby, Coventry		04/09/2019	0.0 to 117.1 km/hr, -0.36 to 0.35 g	62.0 mins, 44.28 km	37220	S-S3c
	V-S4	Roundabout (x14), u-turn, A-road, successive left-right turns, swift maneuvers, change in speed, night-time, A-road (A429, A45, A46), ring-road (A4053), tyre pressure E	Coventry	13 / 12 °C, Passing clouds. Humidity:83% Wind:8.078 mph WNW	06/09/2019	0.0 to 109.6 km/hr, -0.48 to 0.41 g	163.0 mins, 93.9 km	97824	S-S4
B	V-M	Roundabout (x30), successive left-right turns, hard-brake (x21), swift maneuvers (x5), country roads, sharp turn left/right, daytime, u-turn (x1), u-turn reverse (x7), tyre pressure E	Coventry	15 / 12 °C, Partly sunny. Humidity:80% Wind:8.078 mph NW	07/09/2019	0.0 to 100.7 km/hr, -1.01 to 0.44 g	176.7 mins, 105.44 km	105995	S-M
C	V-St1	Roundabout (x9), A-road (A452), B-road, car park navigation, tyre pressure E	Coventry, Kenilworth	13 / 10 °C, Passing clouds. Humidity:56% Wind:7.457 mph ESE	01/04/2019	0.0 to 73.3 km/hr, -0.39 to 0.45 g	95.4 mins, 47.05 km	57213	N/A

Table A2-2. Dataset description from Driver C and D.

Driver	Dataset name	Features	Cities and towns covered	Weather conditions	Collection date	Velocity and acceleration range	Total time driven and distance covered	Total number of data points	Corresponding smartphone dataset
C	V-St4	Roundabout (x1), A-road (A4114, A444, A46), motorway (M40), tyre pressure E	Coventry, Warwick, Chesterton	9 / 4 °C Scattered clouds. Humidity:72% Barometer:991 mbar Wind:12.428 mph W	04/03/2019	0.0 to 101.4 km/hr, -0.27 to 0.13 g	22.7 mins, 28.48 km	13591	N/A
	V-St6	Motorway (M40), daytime, tyre pressure E	Stokenchurch, Headington Oxford	11 / 9 °C, Passing clouds. Humidity:62% Wind:10.564 mph SSW	05/03/2019	0.0 to 122.1 km/hr, -0.32 to 0.35 g	85.6 mins, 113.63 km	51360	N/A
	V-St7	Motorway (M40), residential roads, A-road (A46), tyre pressure E	Stokenchurch, Headington Oxford, Coventry, Kenilworth, Warwick	7 / 6 °C Light rain. Partly sunny. Humidity:85% Wind:14.914 mph W	07/03/2019	0.0 to 117.9 km/hr, -0.3 to 0.3 g	74.0 mins, 90.06 km	44427	N/A
D	V-Y1	Roundabout (x20), successive left-right turns, hard-brake, swift maneuvers, sharp turn left/right, reverse/u-turn (x8), tyre pressure E	Coventry	22 / 16 °C, Passing clouds. Humidity:74% Wind:6.836 mph SSW	30/08/2019	0.0 to 87.5 km/hr, -0.85 to 0.36 g	117.2 mins, 60.86 km	70341	S-Y1
	V-Y2	Roundabout (x9), u-turn/reverse (x1), A-road, B-road, country road, tyre pressure E	Coventry, Kenilworth	7 / 6 °C Light rain. Partly sunny. Humidity:85% Wind:14.914 mph W	08/03/2019	0.0 to 73.3 km/hr, -0.39 to 0.45 g	95.4 mins, 47.05 km	57213	N/A

Table A3-1. Description of datasets V-Vta1a to V-Vta17 from Driver E.

Driver	Dataset name	Features	Cities and towns covered	Weather conditions	Collection date	Velocity and acceleration range	Total time & distance covered	Total no of data points	Corresponding smartphone dataset
E	V-Vta1a	Wet road, gravel road, country road, sloppy roads, roundabout (x3), hard-brake on wet road, tyre pressure A	Nuneaton, Walton on Trent	4-10 / 3-6 °C Passing clouds,	14/112019	0.0 to 103.4 km/hr, -0.54 to 0.35 g	43.0 mins, 40.74 km	25821	S-Vta1a
	V-Vta1b	Hard-brake on muddy road, wet road, country road, tyre pressure A	Coton in the Elms	Broken Clouds,		0.1 to 77.7 km/hr, -0.49 to 0.28 g	1.6 mins, 1.26 km	956	S-Vta1b
	V-Vta2	Roundabout (x2), A-road (A511, A5121, A444), country road, hard-brakes, tyre pressure A	Walton on Trent	Scattered Clouds.		0.0 to 81.6 km/hr, -0.59 to 0.38 g	18.3 mins, 11.07 km	10995	S-Vta2
	V-Vta3	Roundabout (x1), swift maneuvers, tyre pressure A	Burton on Trent	Humidity:75-93%		0.0 to 45.8 km/hr, -0.31 to 0.27 g	1.5 mins, 0.38 km	875	S-Vta3
	V-Vta4	A-road (A511), tyre pressure A	Burton on Trent	Wind:4.971 mph SE		5.9 to 51.7 km/hr, -0.37 to 0.28 g	3.0 mins, 2.02 km	1809	S-Vta4
	V-Vta5	Roundabout (x1), A-road (A511), tyre pressure A	Burton on Trent			29.2 to 51.1 km/hr, -0.26 to 0.09 g	0.6 min, 0.42 km	357	S-Vta5
	V-Vta6	A-road (A511), tyre pressure A	Burton on Trent			43.8 to 103.9 km/hr, -0.24 to 0.13 g	2.3 mins, 2.62 km	1393	S-Vta6
	V-Vta7	Roundabout (x2), A-road (A511), hard-brakes, tyre pressure A	Burton on Trent			22.4 to 113.1 km/hr, -0.54 to 0.18 g	1.4 mins, 1.54 km	857	S-Vta7
	V-Vta8	Town roads, A-roads (A511), tyre pressure A	Hatton Derby			0.0 to 77.6 km/hr, -0.45 to 0.3 g	6.2 mins, 3.43 km	3697	S-Vta8
	V-Vta9	Hard-brakes, A-road (A50), tyre pressure A	Derby			48.9 to 87.7 km/hr, -0.6 to 0.14 g	0.4 min, 0.43 km	226	S-Vta9
	V-Vta10	Roundabout (x1), A-road (A50), tyre pressure A	Sudbury Ashburne			38.8 to 118.0 km/hr, -0.28 to 0.13 g	2.6 mins, 3.95 km	1570	S-Vta10
	V-Vta11	Roundabout (x2), A-road (A50), tyre pressure A	Oaks Green Ashburne			26.8 to 97.7 km/hr, -0.45 to 0.15 g	1.0 min, 0.92 km	589	S-Vta11
	V-Vta12	changes in acceleration in a short period of time, A-road (A515), tyre pressure A	Ashburne			44.7 to 85.3 km/hr, -0.44 to 0.13 g	1.1 mins, 1.27 km	690	S-Vta12
	V-Vta13	A-road (A515), country road, hard-brakes, tyre pressure A	Ashburne			72.7 to 103.6 km/hr, -0.38 to 0.12 g	0.8 mins, 1.14 km	473	S-Vta13
	V-Vta14	Hard-brakes, changes in acceleration in a short period of time, A-road (A515), tyre pressure A	Ashburne			52.8 to 91.0 km/hr, -0.32 to 0.13 g	4.8 mins, 5.45 km	2893	S-Vta14
	V-Vta15	A-road (A515), tyre pressure A	Ashburne			60.1 to 78.8 km/hr, -0.12 to 0.06 g	1.4 mins, 1.72 km	869	S-Vta15
	V-Vta16	Roundabout (x3), hilly roads, country road, A-road (A515), tyre pressure A	Thorpe Ashburne			0.0 to 93.9 km/hr, -0.49 to 0.42 g	18.9 mins, 13.72 km	11361	S-Vta16
	V-Vta17	Hilly roads, hard-brake, stationary (no motion), tyre pressure A	Ilam, Blore			0.0 to 56.2 km/hr, -0.51 to 0.28 g	7.7 mins, 4.19 km	4594	S-Vta17

Table A3-2. Description of datasets V-Vta19 to V-Vta30 from Driver E.

Driver	Dataset name	Features	Cities and towns covered	Weather conditions	Collection date	Velocity and acceleration range	Total time driven and distance covered	Total number of data points	Corresponding smartphone dataset
E	V-Vta19	Hilly road, tyre pressure A	Ilam	4-10 / 3-6 °C	06/11/2019	0.0 to 55.2 km/hr, -0.35 to 0.22 g	0.5 min, 0.26 km	310	S-Vta19
	V-Vta20	Hilly road, approximate straight-line travel, tyre pressure A	Ilam	Passing clouds,		0.0 to 44.8 km/hr, -0.19 to 0.3 g	5.4 mins, 0.39 km	3223	S-Vta20
	V-Vta21	Hilly road, tyre pressure A	Ilam	Broken Clouds,		0.0 to 74.8 km/hr, -0.44 to 0.24 g	3.5 mins, 2.76 km	2088	S-Vta21
	V-Vta22	Hilly road, hard-brake, tyre pressure A	Ilam	Scattered Clouds.		14.8 to 55.8 km/hr, -0.53 to 0.16 g	2.6 mins, 1.67 km	1572	S-Vta22
	V-Vta23	Hilly road, hard-brake, tyre pressure A	Thorpe	Humidity:75-93%		0.0 to 51.9 km/hr, -0.57 to 0.42 g	1.9 mins, 1.1 km	1119	S-Vta23
	V-Vta24	Hilly road, tyre pressure A	Thorpe	SE		0.0 to 56.4 km/hr, -0.46 to 0.36 g	2.0 mins, 0.71 km	1184	S-Vta24
	V-Vta25	U-turn, tyre pressure A	Thorpe	Wind:4.971 mph		0.0 to 48.6 km/hr, -0.46 to 0.3 g	1.1 mins, 0.16 km	646	S-Vta25
	V-Vta26	Gravel road, dirt road, hilly road, tyre pressure A	Thorpe			0.0 to 55.1 km/hr, -0.27 to 0.44 g	3.2 mins, 1.02 km	1947	S-Vta26
	V-Vta27	Gravel road, several hilly roads, potholes, country road, A-road (A515), tyre pressure A	Ashburne			0.0 to 65.0 km/hr, -0.43 to 0.29 g	4.8 mins, 3.16 km	2853	S-Vta27
	V-Vta28	Country road, hard-brakes, valley, A-road (A515), tyre pressure A	Milldale			0.0 to 66.0 km/hr, -0.58 to 0.31 g	7.0 mins, 3.94 km	4219	S-Vta28
	V-Vta29	Hard-brakes, country road, hilly road, windy road, dirt road, wet road, reverse drive (x2), bumps, rain, B-road (B5053), country road, u-turn (x3), windy road, valley, tyre pressure A	Wetton, Milldale			0.0 to 102.0 km/hr, -0.8 -to 0.38 g	39.6 mins, 26.12 km	23737	S-Vta29
	V-Vta30	Rain, wet road, u-turn (x2), A-road (A53, A515), inner town driving, B-road (B5053), tyre pressure A	Buxton			0.0 to 100.0 km/hr, -0.47 to 0.36 g	28.6 mins, 11.77 km	17179	S-Vta30

Table A4. Description of datasets V-Vtb1 to V-Vtb13 from Driver E.

Driver	Dataset name	Features	Cities and towns covered	Weather conditions	Collection date	Velocity and acceleration range	Total time driven and	Total number of data points	Corresponding smartphone dataset
--------	--------------	----------	--------------------------	--------------------	-----------------	---------------------------------	-----------------------	-----------------------------	----------------------------------

					distance covered				
E	V-Vtb1	Valley, rain, wet road, country road, u-turn (x2), hard-brake, swift maneuver, A-road (A6, A6020, A623, A515), B-road (B6405), round about (x3), daytime, tyre pressure A	Bakewell, Tideswell, Ashford on water, Buxton	4-8 / 4 °C Rain, Passing clouds, Broken Clouds, Chilly.	06/11/2019	0.0 to 101.2 km/hr, -0.63 to 0.36 g	54.1 mins, 41.94 km	32459	S-Vtb1
	V-Vtb2	Country road, wet road, dirt road, tyre pressure A	Youlgreave	Humidity:94-98%		0.0 to 61.1 km/hr, -0.36 to 0.39 g	9.5 mins, 4.35 km	5712	S-Vtb2
	V-Vtb3	Reverse, wet road, dirt road, gravel road, night-time, tyre pressure A	Youlgreave	Barometer:1004 mbar		0.0 to 37.5 km/hr, -0.23 to 0.33 g	13.8 mins, 0.71 km	8289	S-Vtb3
	V-Vtb4	Dirt road, country road, gravel, wet road, tyre pressure A	Youlgreave	N Wind:10.564 mph		0.0 to 32.7 km/hr, -0.31 to 0.27 g	1.0 min, 0.27 km	625	S-Vtb4
	V-Vtb5	Dirt road, country road, gravel road, hard-brakes, Wet road, B-road (B6405, B6012, B5056), inner-town driving, A-road, motorway (M42, M1), rush hour(traffic), round-about (x6), a-road (A5, A42, A38, A615, A6), tyre pressure A	Atherstone, Nuthall, Hilcote, Matlock, Rowsley, Youlgreave			0.0 to 112.9 km/hr, -0.55 to 0.42 g	107.7 mins, 111.66 km	64610	S-Vtb5
	V-Vtb6	A-road (A5), tyre pressure A	Atherstone			52.7 to 73.0 km/hr, -0.11 to 0.11 g	0.8 min, 0.89 km	508	S-Vtb6
	V-Vtb7	Approximate straight-line motion, night-time, A-road (A5), tyre pressure A	Atherstone			29.1 to 69.2 km/hr, -0.37 to 0.13 g	0.8 min, 0.72 km	461	S-Vtb7
	V-Vtb8	Approximate straight-line motion, nighttime, wet road, A-road (A5), tyre pressure A	Atherstone			60.9 to 76.5 km/hr, -0.35 to 0.08 g	1.2 mins, 1.35 km	699	S-Vtb8
	V-Vtb9	Approximate straight-line motion, night-time, wet road, hard-brakes, A-road (A5), tyre pressure A	Nuneaton			66.8 to 92.0 km/hr, -0.14 to 0.1 g	0.8 min, 0.98 km	457	S-Vtb9
	V-Vtb10	Round-about, wet road, night-time, A-road (A5), tyre pressure A	Nuneaton			26.1 to 58.5 km/hr, -0.24 to 0.12 g	0.3 min, 0.23 km	195	S-Vtb10
	V-Vtb11	Approximate straight-line motion, night-time, wet road, A-road (A5), tyre pressure A	Nuneaton			65.1 to 75.3 km/hr, -0.05 to 0.12 g	0.7 min, 0.84 km	433	S-Vtb11
	V-Vtb12	Roundabout (x1), wet road, night-time, tyre pressure A	Nuneaton			22.2 to 71.6 km/hr, -0.38 to 0.17 g	0.8 min, 0.61 km	490	S-Vtb12
	V-Vtb13	Parking, wet road, tyre pressure A	Nuneaton			7.5 to 43.3 km/hr, -0.31 to 0.22 g	2.1 mins, 0.99 km	1245	N/A

Table A5. Description of datasets V-Vw1 to V-Vw12 from Driver E.

Driver	Dataset name	Features	Cities and towns covered	Weather conditions	Collection date	Velocity and acceleration range	Total time driven and distance covered	Total number of data points	Corresponding smartphone dataset
E	V-Vw1	Stationary (no motion, sensor bias estimation), daytime, tyre pressure C	Nuneaton	10 °C Smoke.	08/01/2020	0.00 to 0.00 km/hr, 0.00 to -0.00 g	34.1 mins, 0.00 km	20475	S-Vw1
	V-Vw2	A-road (A5, A421), motorway (M5), daytime, roundabout (x22), u-turn (x2), inner city driving, tyre pressure C	Nuneaton, Hinckley Milton Keynes	Wind: 6 mph N Humidity: 86%		0.0 to 115.4 km/hr, -0.62 to 0.45 g	87.9 mins, 98.63 km	52712	S-Vw2
	V-Vw3	Roundabout (x6), daytime, B-road, inner-city driving, tyre pressure C	Milton Keynes			0.0 to 77.4 km/hr, -0.47 to 0.41 g	6.6 mins, 5.05 km	3942	S-Vw3
	V-Vw4	Roundabout (x77), swift-maneuvers, hard-brake, inner city driving, reverse, A-road, motorway (M5, M40, M42), country road, successive left-right turns, daytime, u-turn (x3), tyre pressure D	Milton Keynes, Buckingham, Droitwich Spa, Kidderminster, Worcester			0.0 to 131.9 km/hr, -0.66 to 0.45 g	211.0 mins, 214.62 km	126573	S-Vw4
	V-Vw5	Successive left-right turns, daytime, sharp turn left/right, tyre pressure D	Worcester	10 °C Passing clouds.		0.0 to 38.7 km/hr, -0.4 to 0.21 g	1.8 mins, 0.7 km	1050	S-Vw5
	V-Vw6	Bumps, swift-maneuvers, daytime, sharp turn left/right, pressure D	Worcester	Wind: 2 mph N		3.3 to 40.7 km/hr, -0.34 to 0.26 g	2.1 mins, 1.08 km	1288	S-Vw6
	V-Vw7	Successive left-right turns, daytime, sharp turn left/right, tyre pressure D	Worcester	Humidity: 88%		0.4 to 42.2 km/hr, -0.37 to 0.37 g	2.8 mins, 1.23 km	1689	S-Vw7
	V-Vw8	Successive left-right turns, daytime, sharp turn left/right, tyre pressure D	Worcester			0.0 to 46.4 km/hr, -0.37 to 0.27 g	2.7 mins, 1.12 km	1599	S-Vw8
	V-Vw9	Swift-maneuvers, daytime, hard-brake, tyre pressure D	Worcester			3.8 to 42.0 km/hr, -0.67 to 0.21 g	1.0 min, 0.45 km	601	S-Vw9
	V-Vw10	Hilly road, daytime, pressure D	Worcester			11.8 to 58.9 km/hr, -0.42 to 0.11 g	1.1 mins, 0.74 km	670	S-Vw10
	V-Vw11	Motorway (M5), daytime, roundabout (x5), tyre pressure D				0.0 to 98.4 km/hr, -0.37 to 0.33 g	8.2 mins, 5.85 km	4924	S-Vw11
	V-Vw12	Approximate straight-line motion, daytime, Motorway (M5), tyre pressure D		7 °C Drizzle. Fog. Wind: 5 mph N Humidity: 93%		82.6 to 97.4 km/hr, -0.06 to 0.07 g	1.75 mins, 2.64 km	1050	S-Vw12

Table A6. Description of datasets V-Vw13 to V-Vw17 from Driver E.

Driver	Dataset name	Features	Cities and towns covered	Weather conditions	Collecti on date	Velocity and acceleration range	Total time driven and distance covered	Total number of data points	Corresponding smartphone dataset
E	V-Vw13	Approximate straight-line motion, daytime, motorway (M5), tyre pressure D		7 °C Drizzle. Fog.	08/01/20 20	94.0 to 115.0 km/hr, -0.07 to 0.06 g	0.5 min, 0.82 km	297	S-Vw13
	V -Vw14a	Motorway (M5), nighttime, tyre pressure D		Wind: 5 mph N Humidity: 93%		61.9 to 109.4 km/hr, -0.38 to 0.12 g	5.2 mins, 7.92 km	3140	S-Vw14a
	V -Vw14b	Motorway (M42), nighttime, tyre pressure D				12.6 to 120.1 km/hr, -0.28 to 0.28 g	32.7 mins, 41.21 km	19600	S-Vw14b
	V -Vw14c	Motorway (M42), roundabout (x2), A-road (A446), nighttime, hard-brakes, tyre pressure D				0.0 to 100.5 km/hr, -0.53 to 0.41 g	26.4 mins, 17.15 km	15857	S-Vw14c
	V -Vw15	Stationary (no motion, sensor bias estimation), nighttime, tyre pressure D	Dordon	8 °C Cool. Wind: 2 mph N Humidity: 80%		0.0 to 0.0 km/hr, 0.00 to 0.0 g	2.3 mins, 0.00 km	1391	S-Vw15
	V -Vw16a	A-road (A5), roundabout (x2), tyre pressure D	Atherstone	8 °C Rain		0.0 to 83.5 km/hr, -0.39 to 0.4 g	10.0 mins, 8.49 km	6000	S-Vw16a
	V -Vw16b	Hard-brakes, nighttime, A-road (A5), approximate straight-line travel, tyre pressure D	Nuneaton	showers. Overcast. 2 mph N 80%		1.3 to 86.3 km/hr, -0.75 to 0.29 g	2.0 mins, 1.99 km	1171	S-Vw16b
	V -Vw17	Hard-brakes, nighttime, A-road (A5), approximate straight-line travel, tyre pressure D	Calcedote			31.5 to 72.7 km/hr, -0.8 to 0.19 g	0.5 min, 0.54 km	329	S-Vw17

Table A7-1. Description of datasets V-Vfa01to V-Vfb02c from Driver E.

Driver	Dataset name	Features	Cities and towns covered	Weather conditions	Collection date	Velocity and acceleration range	Total time driven and distance covered	Total number of data points	Corresponding smartphone dataset
E	V-Vfa01	A-road (A444), roundabout (x1), B-road (B4116), daytime, hard-brakes, tyre pressure A	Nuneaton, Twycross, Measham	6 °C Quite cool. Wind: 8 mph N Humidity: 97% 7 °C, Scattered clouds.	08/11/2019	0.0 to 98.4 km/hr, -0.56 to 0.42 g	19.2 mins, 18.8 km	11535	S-Vfa01
	V-Vfa02	B-road (B4116), roundabout (x5), A-road (A42, A641), motorway (M1, M62), high rise buildings, hard-brake, tyre pressure C	Bradford, Measham	Wind: 8 mph N Humidity: 87% 5 °C, Light rain.		0.0 to 117.9 km/hr, -0.67 to 0.48 g	112.9 mins, 163.38 km	67755	S-Vfa02
	V-Vfb01a	City-centre driving, roundabout (x1), wet road, ring-road, nighttime, tyre pressure C	Bradford	Passing clouds. Wind: 10 mph N Humidity:87%		0.0 to 68.9 km/hr, -0.43 to 0.42 g	28.3 mins, 6.81 km	17000	N/A
	V-Vfb01b	Motorway (M606), round-about (x1), city roads, traffic, wet road, changes in acceleration in short periods of time, nighttime, tyre pressure C				0.0 to 83.0 km/hr, -0.38 to 0.23 g	6.5 mins, 4.07 km	3880	N/A
	V-Vfb01c	Motorway (M62), wet-road, heavy traffic, nighttime, tyre pressure C				0.2 to 104.5 km/hr, -0.36 to 0.38 g	10.5 mins, 10.66 km	6320	N/A
	V-Vfb01d	Roundabout (x1), A-road (A650), nighttime, tyre pressure C				0.0 to 56.0 km/hr, -0.46 to 0.36 g	17.9 mins, 3.39 km	10713	N/A
	V-Vfb02a	Motorway (M1), roundabout (x2), A-road (A650), nighttime, hard-brakes, tyre pressure D	East Ardsley,	7 °C, Rain showers. Overcast.		0.0 to 122.3 km/hr, -0.5 to 0.37 g	59.9 mins, 96.5 km	35960	N/A
	V-Vfb02b	Roundabout (x1), bumps, successive left-right turns, hard-brakes (x7), swift-maneuvers, nighttime, tyre pressure D	Nuthall	Wind: 12 mph N Humidity:86%		0.0 to 84.3 km/hr, -0.5 to 0.35 g	18.3 mins, 7.69 km	11000	N/A
	V-Vfb02c	U-turn (x1), hard-brakes, nighttime, tyre pressure D	Nuthall			2.0 to 52.8 km/hr, -0.53 to 0.26 g	1.1 mins, 0.54 km	640	N/A

Table A7-2. Description of datasets V-Vfb02d to V-Vfb02g from Driver E.

Driver	Dataset name	Features	Cities and towns covered	Weather conditions	Collection date	Velocity and acceleration range	Total time driven and distance covered	Total number of data points	Corresponding smartphone dataset
E	V-Vfb02d	Round-about (x1), nighttime, tyre pressure D	Nuthall	7 °C, Rain showers. Overcast. Wind: 12 mph N	08/11/2019	0.0 to 57.3 km/hr, -0.33 to 0.31 g	1.5 mins, 0.84 km	880	N/A
	V-Vfb02e	Changes in acceleration in short period of time, nighttime, tyre pressure D	Nuthall	Humidity:86%		37.4 to 73.9 km/hr, -0.24 to 0.19 g	1.6 mins, 1.52 km	980	N/A
	V-Vfb02f	Roundabout (x1), nighttime, tyre pressure D	Nuthall			1.6 to 49.5 km/hr, -0.24 to 0.32 g	1.1 mins, 0.47 km	660	N/A
	V-Vfb02g	Motorway (M1), A-road (A42, A444, A5), country road, roundabout (x2), hard-brakes, nighttime, tyre pressure D	Nuneaton			0.0 to 119.4 km/hr, -0.51 to 0.35 g	45.3 mins, 63.56 km	27159	N/A

Table A8. Information on other Smartphone Dataset captured independently from drivers F, G and H.

Driver	Dataset name	Location	Comments	Vehicle model	Phone Model	Total Time driven (mins)	Total distance covered (km)	Total number of data points
F	S-T1, S-T2, S-T3, S-T4, S-T5, S-T6, S-T8, S-T9	France	Information on 3-axis orientation and magnetic field not available.	Renault Megane	Motorola moto G7 power	1005.70	1508.39	603425
	S-T10, S-T11	France	-	Renault Megane	Motorola moto G7 power	20.60	8.86	12389
G	S-I	Nigeria	-	Toyota Corolla Verso	Huawei P20 pro,	9.70	0.06	5800
H	S-A1, S-A2, S-A3, S-A4, S-A5, S-A6, S-A7, S-A8, S-A9, S-A10, S-A11, S-A12, S-A13	England	-	Volvo XC70	Blackberry Priv	638.30	1511.93	382956